Received: 11 November 2022 | Revised: 27 April 2023 | Accepted: 25 June 2023

DOI: 10.1002/cnm.3751

BASIC RESEARCH

WILEY

Numerical coupling of 0D and 1D models in networks of vessels including transonic flow conditions. Application to short-term transient and stationary hemodynamic simulation of postural changes

Javier Murillo | **Pilar García-Navarro**

Fluid Dynamic Technologies – I3A, University of Zaragoza, Zaragoza, Spain

Correspondence
Javier Murillo, Fluid Dynamic Technologies – I3A, University of Zaragoza, Zaragoza, Spain.
Email: javier.murillo@unizar.es

Present address
Javier Murillo, EINA, C. María de Luna, 3, Zaragoza, Spain.

Funding information
Gobierno de Aragón, Grant/Award Numbers: T32-20R, E24-17R

Abstract

When modeling complex fluid networks using one-dimensional (1D) approaches, boundary conditions can be imposed using zero-dimensional (0D) models. An application case is the modeling of the entire human circulation using closed-loop models. These models can be considered as a tool to investigate short-term transient and stationary hemodynamic responses to postural changes. The first shortcoming of existing 1D modeling methods in simulating these sudden maneuvers is their inability to deal with rapid variations in flow conditions, as they are limited to the subsonic case. On the other hand, numerical modeling of 0D models representing microvascular beds, venous valves or heart chambers is also currently modeled assuming subsonic flow conditions in 1D connecting vessels, failing when transonic and supersonic flow conditions appear. Therefore, if numerical simulation of sudden maneuvers is a goal in closed-loop models, it is necessary to reformulate the current methodologies used when coupling 0D and 1D models, allowing the correct handling of flow evolution for both subsonic and transonic conditions. This work focuses on the extension of the general methodology for the Junction Riemann Problem (JRP) when coupling 0D and 1D models. As an example of application, the short-term transient response to head-up tilt (HUT) from supine to upright position of a closed-loop model is shown, demonstrating the potential, capability and necessity of the presented numerical models when dealing with sudden maneuvers.

KEYWORDS

0D-1D coupling, HUT, junctions, mathematical modeling, short-term transient, sonic flow

1 | INTRODUCTION

Numerical modeling of 1D flow in networks, coupled with 0D models, can be considered as an alternative to three-dimensional (3D) modeling when analyzing human blood flow in large/medium arteries and veins[1–9] and its

sensitivity to variations in the body positioning[10] with only a fraction of the computational cost. A challenging problem of fluid–structure interactions (FSIs) appear due to the flexibility of veins, that contrary to arteries, in sitting or standing positions collapse.[5] In order to characterize fluid flow in a flexible vessel, it is useful to define the speed index S (the ratio of flow velocity and pulse wave velocity),[11] describing subcritical flow ($S<1$), sonic flow ($S=1$) and supercritical flow ($S>1$). This parameter allows to explain experimental observations related with flow limitation or sonic blockage. When sonic blockage is produced, an increase in the difference between upstream and downstream pressures in a vessel is unable to increase the flow across the nozzle throat generated in the same vessel.[11] Vascular waterfall or a flow limitation is observed in the venous return in the CVS when the pressure inside the vena cava is smaller than the pressure outside.[12,13] This phenomenon is observed at atmospheric pressure when breathing spontaneously. When venous collapse occurs, further decrease of the right atrial pressure does not improve venous return.[14] In the respiratory tract, during forced expiration, flow limitation is produced with independence of the effort put forward by the patient.[15] In general, dealing with highly compliant venous walls lead to problems of FSIs including collapse, shock waves and self-oscillations, leading to complex problems.[10]

The appropriate treatment of all these phenomena requires non-trivial numerical methodologies when using 1D models for blood flow. 1D models for blood flow approaches[16–18] involve mass and momentum conservation, leading to a hyperbolic system of equations with source terms. Source terms are used to represent the presence of time-dependent postural maneuvers, pressure variations or muscular activity[2,19,20] as well as the spatial variations of the mechanical and geometrical properties of the vessel wall.[21]

Even when ignoring transient maneuvers, spurious oscillations in the numerical solution may appear unless the numerical resolution focus first on the balance between fluxes and source terms. This type of schemes providing well balanced solutions[21–25] can be applied to the analysis of the flow in collapsible vessels.[21–23] Furthermore, exactly well-balanced methods or energy balanced numerical schemes ensure exact solutions derived from the entropy function of the system, an energy conservation law.[21,24,25]

Due to gravity, postural changes cause fluid shifts that induce significant changes in pressure and, consequently, in the area of venous vessels, which can lead to vessel collapse. General pressure–area relations for collapsible vessels require a complex parametrization that allows to model the much more deformable behavior of veins. In 1D modeling veins are characterized using tube laws for thin-walled vessels. They have a sigmoid shape where pressure falls exponentially when the area tends to zero. When approaching a collapsed state, it is of utmost importance to control the approximations made in the numerical scheme, as the eigenvalues of the system do not determine the time step size, as in such conditions, the pure hyperbolic character of the set of equations is lost. A careless discretization of the source terms may lead to unrealistic or non-physiological values of transmural pressure or even negative vessel area.[21]

For 1D blood flow with constant vessel geometrical and mechanical properties it is possible to provide a flux formulation description of the system[26] and a straight forward flux formulation of the numerical solver, avoiding the presence a source vector term. If variations in vessel properties cannot be ignored, conservation-law form can still be achieved, and the source term will incorporate additional terms deriving from the spatial variation of vessel parameters. When involving geometrical and mechanical properties, numerical schemes are usually expressed in fluctuation form.[24,27] Augmented solvers, as the ARoe solver (Augmented Roe)[25] and the HLLS solver[28] can be expressed in fluctuation form or in flux form by transforming the initial Riemann Problem (RP) formulation in an approximate RP written in conservative–law form. Also, both schemes can be designed to verify the exactly well-balanced property, preserving energy conservation across contact discontinuities with variations in mechanical and geometrical properties, under subsonic and supersonic flow conditions. In Reference 21 both solvers were adapted for the first time to deal with test cases involving flow limitation and extreme collapsing conditions in elastic vessels. One property of these family of solvers is that they allow to describe the underlying set of approximate inner states providing the numerical solution, allowing to prevent unphysical values of transmural pressure while retaining the eigenvalues of the system in the hyperbolic region. But these robust and powerful tools become useless in the context of 1D flow in networks unless a methodology able to deal with discontinuities or high subcritical, transcritical and supercritical flow through junctions can be applied.

The junction, in a 1D framework, is an internal boundary conditions, that can be defined as a Junction Riemann Problem (JRP). There are different ways to deal with the JRP. There are methods based on energy or momentum conservation coupled with the continuity equation and the characteristic equations[22,29] that consider the solution in the subsonic regime represented by rarefactions or decompression waves. It is also possible to use the exact solution of the JRP at the junction[6,7,30,31] based on wave relations for shock and rarefactions (or compression and decompression waves) but the method fails even for subsonic flows at moderately high Froude numbers.[32] Another possibility is to

define bulk mechanical properties[10,20] in the junction that depend on the grid size used to the 1D vessels and require an specific numerical discretization, that even being able to manage supersonic flow conditions, cannot offer solutions derived by a standard eigen-structure analysis of the hyperbolic system of equations for flow in collapsible tubes in Reference 26 including transonic and supersonic conditions.

In Reference 33 a new methodology for the JRP was presented for the first time, allowing solutions for all type of flow transitions, including transonic flow, with independence of the number of vessels, for merging and splitting flows or any other possible combination in a confluence of vessels for elastic and collapsible tubes. This methodology can be used together with any numerical scheme of arbitrary order of accuracy, without requiring the definition of any extra information. The solutions are completely consistent with the underlying hyperbolic system of conservation laws, and can be applied to merging flows, splitting flows or any other possible combination in a confluence of vessels.

The hemodynamic effect of terminal vessels representing the peripheral circulation, venous valves, heart chamber time-varying elastance and cardiac valves among others, can be accounted for using lumped parameter or 0D models, where subsonic flow conditions in the 1D-0D coupling are always considered.[6–8,22,29,34–37] Considering that the blood flow in the arterial circulation is subsonic, it may seem unnecessary to extend the formulation of lumped models accounting for micro-circulation to include transonic flow conditions. But 0D models can be used to represent vascular beds connecting arteries and veins, portal venous systems where vascular beds are connected by veins, venous valves or hear models coupling venous return with the atria. In all these models flow conditions are subject to fast changes requiring numerical methodologies able to cope with any transient flow.

Hybrid models of networks containing hyperbolic conservation laws and lumped parameter models will be formulated by solving the classical Riemann problem at the junction,[38] the first order approach at the junction of the Generalized Riemann problem. Solving the classical JRP is equivalent to find a set of Godunov states on each junction vessel that fulfill a set of initial value problems together with a set of algebraic coupling conditions.

In this work, the methodology presented in Reference 33 for the JRP, recalled in Section 2.2, is extended to provide a correct management of transient flow in 1D-0D coupled models, including: valve modeling in Section 2.3, vascular bed modeling in Section 2.4 and heart modeling in Section 2.5. Considering that this is the main goal of this work, we first confirm in each section their robustness by presenting numerical experiments conducted to explore the solutions when subsonic, sonic, and supersonic conditions are imposed. Once all the numerical methodologies presented in this work are tested, we apply directly all these methods to a global tool, where the impact of transient maneuvers over the flow conditions in an integrated closed model of the CVS is analyzed. Therefore, in Section 3, the short-term transient response of a closed-loop model to HUT from supine to upright is shown, proving the ability of the presented models to deal with sudden maneuvers.

2 | MATERIALS AND METHODS

2.1 | 1D Mathematical models in arteries and veins

The 1D equations for flow in compliant vessels involve cross section average of the mass and momentum, leading to the following first-order, nonlinear hyperbolic system,

$$\partial_t \mathbf{U} + \partial_x \mathcal{F}(\mathbf{U}) = \mathbf{G}_\chi, \tag{1}$$

with $\mathbf{U} = \mathbf{U}(x,t)$ and

$$\mathbf{U} = \begin{bmatrix} A \\ Q \end{bmatrix}, \quad \mathcal{F}(\mathbf{U}) = \begin{bmatrix} Q \\ \dfrac{Q^2}{A} \end{bmatrix}, \quad \mathbf{G}_\chi = \begin{bmatrix} 0 \\ -\dfrac{A}{\rho}\dfrac{\partial p}{\partial x} - \dfrac{f}{\rho} - gA\dfrac{\partial \eta}{\partial x} \end{bmatrix} = \begin{bmatrix} 0 \\ G_\chi \end{bmatrix}, \tag{2}$$

where x is the axial coordinate along the vessel, t is the time, A is the cross-sectional area, $Q = Au$ is the volume flow rate with u the cross sectional average axial velocity, $p(x,t)$ is the average internal pressure over the cross section, f is the friction force per unit length, ρ is the blood density and η is a coordinate perpendicular to the horizontal plane, that accounts for the gravitational forces due to the presence of gravity acceleration g. This system of equations is closed by the following relation for pressure

$$p(x,t)-p_e(x,t)=p_{tr}, \tag{3}$$

where p_e is the external pressure and p_{tr} is the transmural pressure. If only elastic deformation of the vessel wall is considered, transmural pressure is formulated as

$$p_{tr}=K_o\sigma+p_o,\quad \sigma(\alpha)=\alpha^{m_\sigma}-\alpha^{n_\sigma}, \tag{4}$$

with $\alpha=A/A_o$, $A_o=A_o(x)$ the vessel cross-sectional reference area for which the transmural pressure p_{tr} is p_o and $\sigma(\alpha)$ the dimensionless transmural pressure difference. Vessel stiffness $K_o(x)$ and exponents m_σ and n_σ depend on the type of vessel. Transmural pressure for arteries is commonly defined setting $m_\sigma=1/2$ and $n_\sigma=0$. For veins, typical values for thin-walled elastic collapsible tubes, $m_\sigma=10$ and $n_\sigma=-3/2$ are used. The hyperbolic character of the equations is retained only if $m_\sigma\geq 0$ and $n_\sigma\geq -2$,[26] covering our range of application.

When using the pressure relation in (3) the momentum equation in (1) can be rewritten as follows

$$\partial_t Q+\partial_x\left(Au^2\right)+\alpha\frac{K_o}{\rho}(\partial_\alpha\sigma)(\partial_x A-\alpha\ \partial_x A_o)+\frac{A\sigma}{\rho}\partial_x K_o+\frac{A}{\rho}\partial_x p_e=-\frac{f}{\rho}-gA\partial_x\eta. \tag{5}$$

The following function φ

$$\varphi=D_o\ \Omega,\quad D_o=\frac{A_oK_o}{\rho},\quad \Omega=\left(\frac{m_\sigma}{m_\sigma+1}\alpha^{m_\sigma+1}-\frac{n_\sigma}{n_\sigma+1}\alpha^{n_\sigma+1}\right), \tag{6}$$

where

$$\partial_x\varphi=\alpha\frac{K_o}{\rho}(\partial_\alpha\sigma)(\partial_x A-\alpha\ \partial_x A_o)+\Omega\left(\frac{K_o}{\rho}\partial_x A_o-\frac{A_o}{\rho}\partial_x K_o\right), \tag{7}$$

can be used to express momentum in Equation (5)

$$\partial_t Q+\partial_x\left(Au^2\right)+\partial_x\varphi-\frac{K_o}{\rho}\Omega\ \partial_x A_o+\frac{1}{\rho}(A\sigma-A_o\Omega)\partial_x K_o+\frac{A}{\rho}\partial_x p_e=-\frac{f}{\rho}-gA\partial_x\eta. \tag{8}$$

Now system of equations in (1) is written as

$$\partial_t\mathbf{U}+\partial_x\mathbf{F}_\varphi(\mathbf{U})=\mathbf{S}_\chi, \tag{9}$$

where the new flux vector $\mathbf{F}_\varphi(\mathbf{U})$ and new vector of source terms $\mathbf{S}_\chi$ are

$$\mathbf{F}_\varphi=\begin{bmatrix}Au\\ Au^2+\varphi(\alpha)\end{bmatrix},\quad \mathbf{S}_\chi=\begin{bmatrix}0\\ \frac{K_o}{\rho}\Omega\ \partial_x A_o-\frac{1}{\rho}(A\sigma-A_o\Omega)\partial_x K_o-\frac{A}{\rho}\partial_x p_e-\frac{f}{\rho}-gA\partial_x\eta\end{bmatrix}, \tag{10}$$

with

$$(A\sigma-A_o\Omega)=(m_\sigma+1)^{-1}\alpha^{m_\sigma+1}-(n_\sigma+1)^{-1}\alpha^{n_\sigma+1}. \tag{11}$$

System in (9) can be written in quasi-linear form as follows

$$\frac{\partial\mathbf{U}}{\partial t}+\mathbf{J}(\mathbf{U})\frac{\partial\mathbf{U}}{\partial x}=\mathbf{S}_\chi, \tag{12}$$

with

$$\mathbf{J}=\begin{bmatrix}0 & 1\\ c^2-u^2 & 2u\end{bmatrix},\quad c=\alpha\frac{K_o}{\rho}(\partial_\alpha\sigma)=\sqrt{\frac{K_o}{\rho}\left(m_\sigma\alpha_\sigma^m-n_\sigma\alpha_\sigma^n\right)}, \tag{13}$$

where c is the Pulse Wave Velocity (PWV). Matrix $\mathbf{J}$ has two eigenvalues, $\lambda^1=u-c$ and $\lambda^2=u+c$, and two real eigenvectors, $\mathbf{e}^1=\left(1,\lambda^1\right)^T$ and $\mathbf{e}^2=\left(1,\lambda^2\right)^T$. When vessel mechanical and geometrical properties are considered constant, external pressure is constant and friction and gravity terms are neglected the source term $\mathbf{S}_\chi$ vanishes and the system is strictly hyperbolic.

2.1.1 | 1D Numerical method in vessels

All the vessels of the domain, a 1D network, are discretized in computational cells of constant length size $\Delta x=x_{i+1/2}-x_{i-1/2}$, leading to N_k cells in eack k vessel. In k vessel its local numbering is $i=1,...,N_k$. We will call terminal cells to those cells involved in the coupling with internal boundary conditions where the local numbering is $I_k=1$ or $I_k=N_k$, with I_k the index of the computational cell of vessel k linked to the boundary condition.

Following the Godunov first order method, by integrating (9), we obtain the following updating formula[21]

$$\mathbf{U}_i^{n+1}=\mathbf{U}_i^n-\frac{\Delta t}{\Delta x}\left[\mathbf{F}_{i+\frac{1}{2}}^-\mathbf{F}_{i-\frac{1}{2}}^+\right], \tag{14}$$

with

$$\mathbf{U}_i^n=\frac{1}{\Delta x}\int_{x_{i+1/2}}^{x_{i-1/2}}\mathbf{U}(x,t^n)dx, \tag{15}$$

where (15) gives the spatial-integral average at time $t=t^n$ of the conserved variable, $\Delta t=t^{n+1}-t^n$ and $\mathbf{F}_{i\mp1/2}^{\pm}$ are the numerical fluxes, with $\mathbf{F}=\mathbf{F}\left(\mathcal{F},\mathbf{G}_\chi\right)$. Following the quasi-steady wave-propagation algorithm,[39] the updating formula in (14) can be rewritten in terms of fluctuations,

$$\mathbf{U}_i^{n+1}=\mathbf{U}_i^n-\frac{\Delta t}{\Delta x}\left[\delta\mathbf{M}_{i+\frac{1}{2}}^-+\delta\mathbf{M}_{i-1/2}^+\right], \tag{16}$$

denoted here by δM. In this work, we define the following relation between fluxes and fluctuations as follows

$$\mathbf{F}_{i+\frac{1}{2}}^-=\mathbf{F}_{\varphi,i}^n+\delta\mathbf{M}_{i+1/2}^-,\quad \mathbf{F}_{i-\frac{1}{2}}^+=\mathbf{F}_{\varphi,i}^n-\delta\mathbf{M}_{i-\frac{1}{2}}^+, \tag{17}$$

with $\mathbf{F}_{\varphi,i}^n=\mathbf{F}_\varphi\left(\mathbf{U}_i^n\right)$, where in cases of exact equilibrium $\delta\mathbf{M}_{i\mp1/2}^{\pm}=0$.

On the other hand, we will refer to the evolved states in time at the terminal interfaces in $I_k=1$ or $I_k=N_k$ of the kth vessel as $\mathbf{U}_k^\star=\left[A_k^\star,Q_k^\star\right]$. This state, generated by the imposition of internal boundary conditions, will be used to compute the updating fluxes at its respective terminal interface

$$\begin{aligned}\mathbf{F}_{i-\frac{1}{2}}^+&=\mathbf{F}_\varphi\left(\mathbf{U}_k^\star\right),\quad I_k=1,\\ \mathbf{F}_{i+\frac{1}{2}}^-&=\mathbf{F}_\varphi\left(\mathbf{U}_k^\star\right),\quad I_k=N_k,\end{aligned} \tag{18}$$

or in fluctuation form as

$$\begin{aligned}\delta\mathbf{M}_{i-\frac{1}{2}}^+&=\mathbf{F}_\varphi\left(\mathbf{U}_i^n\right)-\mathbf{F}_\varphi\left(\mathbf{U}_k^\star\right),\quad I_k=1,\\ \delta\mathbf{M}_{i+\frac{1}{2}}^-&=\mathbf{F}_\varphi\left(\mathbf{U}_k^\star\right)-\mathbf{F}_\varphi\left(\mathbf{U}_i^n\right),\quad I_k=N_k.\end{aligned} \tag{19}$$

The hyperbolic system of Equation (1) can be solved using numerous numerical solvers where the numerical fluctuations can be computed using the path-conservative framework as[7,37,40] or as in References 21,25,33.

2.2 | Solution of the JRP

The definition of the internal boundary conditions for flow at junctions for merging flows, splitting flows or other possible combinations in a confluence of vessels is revisited here. The Riemann problem at vertex P or JRP, for N_P infinitely long converging vessels sharing vertex P is defined as the following set of initial value problems (IVP)

$$\frac{\partial \mathbf{U}_k}{\partial t}+\frac{\partial \mathbf{F}_\varphi}{\partial x}(\mathbf{U}_k)=\mathbf{S}_{\chi,k}, \quad \mathbf{U}_k(x,0)=\mathbf{U}_k^n, \tag{20}$$

for $k=1,...,N_P$, together with the following vector of coupling conditions

$$\Phi_c\left(\mathbf{U}_0^\star,...,\mathbf{U}_{N_P}^\star\right)=0, \tag{21}$$

where $\mathbf{U}_k^n$, with $k=1,...,N_P$ are constant vectors. The solution of the JRP with IVP's in (20) with constraints in (21) is a set of self-similar functions for each kth vessel, defined by $2N_P$ constant states. The constant states are the N_P constant initial conditions provided by the one-dimensional vessels $\mathbf{U}_k^n=\left[A_k^n,Q_k^n\right]$, with $k=1,...,N_P$, and the N_P remaining states are the evolved states $\mathbf{U}_k^\star=\left[A_k^\star,Q_k^\star\right]=\left[A_k^\star,A_k^\star u_k^\star\right]$, with $k=1,...,N_P$ at the junction.

The initial states $\mathbf{U}_k^n$ and the evolved states $\mathbf{U}_k^\star$ are connected through non-linear waves and among themselves by the coupling conditions in (21). In this work we consider that the material and geometrical properties can be different for each kth vessel, and variable inside each kth vessel. On the other hand, as we are using a first-order numerical method, material and geometrical properties are defined constant inside each cell the computational cells sharing vertex P, leading to $\mathbf{S}_{\chi,k}=\mathbf{0}$ in (20).

To couple the N_P vessels, we have to compute the unknown cross-sectional area $A_k^\star$ and velocity $u_k^\star$ for each vessel converging at node P, which means that we have $2N_P$ unknowns. Evolved states $A_k^\star$ and $u_k^\star$ will be used to compute fluxes at the boundary interface of the kth vessel in (18). In this work, all vessels involved in an internal boundary condition will be identified by the following auxiliary function can be defined depending on the position of the terminal cell[31]

$$g_k(I_k)=\begin{cases}1 & if \quad I_k=N_k\\ -1, & if \quad I_k=1\end{cases}. \tag{22}$$

This auxiliary function allows to distinguish between outflow vessels, where flow at the boundary cell initially leaves the domain, $(gu)_k^n>0$, and inflow vessels, where flow initially enters at the boundary cell, $(gu)_k^n<0$. We also define the following boundary Speed Index (SI)[33]

$$SI_{g,k}=g_k\frac{u_k}{c_k}, \tag{23}$$

and when $|SI|_{g,k}<1$, subsonic flow conditions will be defined in the I_k boundary cell of vessel k.

2.2.1 | Solution of the JRP under subsonic conditions

If we assume that initial and evolved states are under subsonic conditions, $|SI|_{g,k}^n<1$ and $|SI|_{g,k}^\star<1$, the coupling conditions that connect the evolved states $\mathbf{U}_k^\star$, with $k=1,...,N_P$, among themselves are

$$\Phi_c\left(\mathbf{U}_0^\star,...,\mathbf{U}_{N_P}^\star\right)=\begin{bmatrix}\sum_k\left[g(\alpha^\star A_o\ u^\star)\right]_k\\ \left[p_{T,1}^\star-p_{T,2}^\star\right]\\ \vdots\\ \left[p_{T,1}^\star-p_{T,N_P}^\star\right]\end{bmatrix}=\mathbf{0}, \tag{24}$$

where $p_T=p_M+K_o\sigma+\frac{1}{2}\rho u^2$, the value of total pressure, with $p_M=p_o+p_{ext}+\rho g\eta$. The first component in the system of coupling conditions (24) ensures mass conservation. The remaining N_P-1 components, guarantee equality of total pressure in all the vessels meeting at vertex P.

For any boundary cell, and depending on the sign of the jump between the evolved state and the initial state for α, $d\alpha_k^\star=\alpha_k^\star-\alpha_k^n$, the solution of the IVP in (20) for the kth vessel will be a shock ($d\alpha_k^\star>0$), or a rarefaction ($d\alpha_k^\star<0$).[26] We define the celerities of the system as $\lambda_{1g,k}=u_k-g_kc_k$ and $\lambda_{2g,k}=u_k+g_kc_k$. As the solutions of the IVP in (20) can only be developed in the inner region of each vessel, we will only need to explore solutions where $g_k\lambda_{1g,k}^\star\le 0$.

The solution of the IVP in (20) is a non-linear relationship between $\mathbf{U}_k^\star$ and $\mathbf{U}_k^n$, with $k=1,...,N_P$, and is written as follows[26]

$$u_k^\star-u_k^n+g_k\mathcal{B}_k=0, \tag{25}$$

with

$$\mathcal{B}_k=\begin{cases}dW_k^\star & \text{if} \quad d\alpha_k^\star\le 0\\ f_{g,k}^\star & \text{if} \quad d\alpha_k^\star>0,\end{cases} \tag{26}$$

where

$$dW_k^\star=\int_{\alpha_k^n}^{\alpha_k^\star}\frac{c(a)}{a}da, \quad f_{g,k}^\star=\left(\frac{1}{A_{o,k}}\left(\frac{1}{\alpha_k^n}-\frac{1}{\alpha_k^\star}\right)\left(\varphi_k^\star-\varphi_k^n\right)\right)^{\frac{1}{2}}. \tag{27}$$

When the solution of the IVP for the kth vessel is a rarefaction, the solution satisfies the following entropy conditions

$$g_k\lambda_{1g,k}^n<g_k\lambda_{1g,k}^\star\le 0, \tag{28}$$

and if the solution of the IVP for the kth vessel is a shock, the shock speed $S_{g,k}$ is given by

$$S_{g,k}=u_k^n-g\left(\frac{\varphi_k^\star-\varphi_k^n}{f_g^\star A^n}\right)_k, \quad -g_kS_k>0, \tag{29}$$

where the entropy conditions are

$$g_k\lambda_{1g,k}^\star<g_kS_{g,k}<g_k\lambda_{1g,k}^n. \tag{30}$$

The set of self-similar solutions provided for the k IVP's posed in the JRP is defined with the following vector

$$\Phi_{IVP}\left(\mathbf{U}_0^\star,...,\mathbf{U}_{N_P}^\star,\mathbf{U}_0^n,...,\mathbf{U}_{N_P}^n\right)=\begin{bmatrix}(u^\star-u^n+g\mathcal{B})_1\\ \vdots\\ (u^\star-u^n+g\mathcal{B})_{N_P}\end{bmatrix}=\mathbf{0}. \tag{31}$$

The solution of the JRP for subsonic flow conditions can be defined by a system of $2N_P$ equations of the form $\mathbf{E}(\mathbf{X})=\mathbf{0}$, with

$$\mathbf{E}(\mathbf{X})=\begin{bmatrix}\Phi_{IVP}\\ \Phi_c\end{bmatrix},\quad \mathbf{X}=\left[u_1^\star,...,u_{N_P}^\star,\alpha_1^\star...,\alpha_{N_P}^\star\right]^T, \tag{32}$$

with $\mathbf{X}$ the vector of the unknowns of the problem. System of equations in (32) is non-linear is solved here using Picard iterations between times t and $t+\Delta t$. In terms of notation, iterations are denoted by superscript m. The solution at m iteration or the initial solution $\mathbf{X}^m$ will be updated as follows

$$\mathbf{X}^{m+1}=\mathbf{X}^m+\delta\mathbf{X}^m. \tag{33}$$

In order to find $\delta\mathbf{X}^m$, we first consider the Taylor expansions of the functions in $\mathbf{E}(\mathbf{X})$, with

$$\mathbf{E}\left(\mathbf{X}^{m+1}\right)=\mathbf{E}(\mathbf{X}^m)+\mathbf{J}_\mathbf{E}(\mathbf{X}^m)\delta\mathbf{X}^m+O_i\left(\delta\mathbf{X}^2\right) \tag{34}$$

where $\mathbf{J}_\mathbf{E}(\mathbf{X})$ is Jacobian matrix defined over the function vector $\mathbf{E}(\mathbf{X})$. If the error terms are assumed negligible and $\mathbf{E}(\mathbf{X}^{m+1})=0$, the system of equations can be written in linear form and $\delta\mathbf{X}^m$ is found solving the equation

$$\mathbf{J}_\mathbf{E}(\mathbf{X}^m)\delta\mathbf{X}^m=-\mathbf{E}(\mathbf{X}^m). \tag{35}$$

Once all variables are updated, the procedure is repeated until $\mathbf{E}^{m+1}=\mathbf{E}(\mathbf{X}^{m+1})$ is under a desired tolerance.

2.2.2 | Solution of the JRP under subsonic and supersonic flow conditions

When the solutions of the k IVP's are not exclusively subsonic, the formulation of the solution for the IVP's and the coupling conditions in system of equations in (32) must be modified. One consequence of the generalization of the solution is that the number of unknowns of the system may change during the iterative search of the solution, changing the size of the system of equations and the size of the Jacobian in (35), requiring also the reordering of the unknowns of the problem. In order to preserve the original size of the system of equations and the vector of unknowns during the computation of the solution, the updating Jacobian matrix is reformulated to return $\delta u_k^{\star,m}=0$ and $\delta\alpha_k^{\star,m}=0$ when necessary. This is done with the help of a set of dynamic coefficients that will be evaluated after each iteration in each vessel.

In the case that the solution of the IVP in the kth vessel is a rarefaction or decompression wave, under initial subsonic conditions with $\left|SI_g^n\right|<1$ or under initial supersonic conditions with $SI_g^n<-1$, the limiting value of $Q_k^\star$ is given by $g_k\lambda_{1g}^\star=0$. In this case the velocity is limited by $u_k^\star=g_kc_k^\star$ with $c_k^\star=c_k^\star\left(\alpha_k^\star\right)$, and $u_k^\star$ is not any longer an unknown of the system. On the other hand, further acceleration/deceleration generated by a backward/forward rarefaction wave, in a vessel under initial supersonic conditions with $SI_g^n>1$, must be avoided. In order to include these limits in the evolution of the IVP, the solution to the IVP for the kth vessel in (32) is modified as follows

$$(u^\star-u^n+g\mathcal{B})_k\mathcal{D}_{w,k}+(u^\star-u^n)_k(1-\mathcal{D}_{w,k})=0, \tag{36}$$

with

$$u_k^{\bullet} = \mathcal{R}_{w,k}\, g_k c_k^{\star} + \mathcal{T}_{w,k} u_k^{\star}, \quad \mathcal{T}_{w,k} = 1 - \mathcal{R}_{w,k}. \tag{37}$$

After each iteration, once the vector of unknowns is updated providing the new value $\mathbf{X}^{m+1}$, the coefficients $\mathcal{R}_{w,k}$, $\mathcal{T}_{w,k}$ and $\mathcal{D}_{w,k}$ in (36) and (37) are dynamically updated for each k vessel. Coefficient $\mathcal{R}_{w,k}$ is evaluated after each iteration as follows

$$\mathcal{R}_{w,k}^{m+1} = \begin{cases} 1 & \text{if } SI_{g,k}^{\star,m} < 1 \quad \text{and} \quad SI_{g,k}^{\star,m+1} > 1 \quad \text{and} \quad \left(\alpha_k^{\star,m+1} - \alpha_k^n\right) \le 0 \\ 0 & \text{otherwise,} \end{cases} \tag{38}$$

and is zero when sonic conditions are not reached during the iterative search of a rarefaction solution, resulting in $\mathcal{T}_w^{m+1} = 1$. In this case the solution of the IVP is reduced to the subsonic case in (25). When sonic conditions are reached, $\mathcal{R}_{w,k}^{m+1} = 1$, and $u_k^{\star}$ is not an unknown of the system.

Coefficient $\mathcal{D}_{w,k}^{m+1}$ is defined as follows

$$\mathcal{D}_{w,k}^{m+1} = \begin{cases} 0 & \text{if } SI_{g,k}^n \ge 1 \text{ and } \left[g_k\left(Q^{\star,m+1} - Q^n\right)_k > 0 \text{ or } \left(\alpha^{\star,m+1} - \alpha^n\right)_k < 0\right] \\ 0 & \text{if } SI_{g,k}^n \ge 1 \text{ and } -g_k S_{g,k}^{\star,m+1} < 0 \\ 0 & \text{if } SI_{g,k}^n \ge 1 \text{ and } -g_k \lambda_{1g,k}^{\star,m+1} < 0 \\ 1 & \text{otherwise} \end{cases}, \tag{39}$$

and will be used to ensure that in outflow vessels with initial supersonic conditions with $SI_{g,k}^n > 1$, when $\mathcal{D}_{w,k} = 0$, the solution of the IVP for vessel k is $\mathbf{U}_k^{\star} = \mathbf{U}_k^n$, avoiding further acceleration of the flow in supersonic conditions or unphysical shock waves traveling in the wrong direction. The new set of self-similar solutions is defined with the following vector

$$\mathbf{\Phi}_{IVP}^s\left(\mathbf{U}_0^{\star}, ..., \mathbf{U}_{N_P}^{\star}, \mathbf{U}_0^n, ..., \mathbf{U}_{N_P}^n\right) = \begin{bmatrix} (u^{\bullet} - u^n + g\mathcal{B})_1 \mathcal{D}_{w,1} + du_1^{\star}(1 - \mathcal{D}_{w,1}) \\ \vdots \\ (u^{\bullet} - u^n + g\mathcal{B})_{N_P} \mathcal{D}_{w,N_P} + du_{N_P}^{\star}(1 - \mathcal{D}_{w,N_P}) \end{bmatrix} = \mathbf{0}, \tag{40}$$

with $du_k^{\star} = (u^{\star} - u^n)_k$. The vector of coupling conditions in (21) has to be modified to accommodate the new solution of the IVP in (36), and the evolved state for flow, $Q_k^{\star}$ in the kth vessel is given by

$$Q_k^{\star} = \mathcal{D}_{w,k}(\alpha^{\star} A_o\, u^{\bullet})_k + (1 - \mathcal{D}_{w,k}) Q_k^n. \tag{41}$$

When extending the solution of the JRP to sonic and supersonic solutions, all the evolved states of the N_P vessel may not participate in the energy conservation equation. The reference value in the energy conservation equation is defined as follows

$$p_T^{\bullet} = \sum_{k=1}^{N_P} \mathcal{L}_{w,k}\, p_{T,k}^{\star}, \tag{42}$$

with

$$\mathcal{L}_{w,k}^{m+1} = \begin{cases} 1 & \text{if} \quad k = k_{\mathcal{L}} \\ 0 & \text{otherwise} \end{cases}, \quad k_{\mathcal{L}} = \min\left\{k, \mathcal{T}_{w,k}^{m+1} \mathcal{D}_{k,w}^{m+1} = 1\right\}, \quad k = 1, ..., N_P. \tag{43}$$

Dynamic coefficient $\mathcal{L}_{w,k}$ is updated after each iteration. It is always zero except for the first eligible vessel where energy conservation can be defined. Ineligible vessels do not participate in the energy conservation equation when $\mathcal{T}_{w,k}=0$ (flow limitation) or $\mathcal{D}_w=0$ (conservation of the initial condition). The new vector of coupling conditions is given by

$$\mathbf{\Phi}_c^s\left(\mathbf{U}_0^\star,...,\mathbf{U}_{N_P}^\star,\mathbf{U}_0^n,...,\mathbf{U}_{N_P}^n\right)=\begin{bmatrix}\sum_k g_k\left[\mathcal{D}_{w,k}(\alpha^\star A_o\ u^\bullet)_k+(1-\mathcal{D}_{w,k})Q_k^n\right]\\ \left[p_T^\bullet-p_{T,2}^\star\right]\mathcal{Q}_{w,2}\\ \vdots\\ \left[p_T^\bullet-p_{T,N_P}^\star\right]\mathcal{Q}_{w,N_P}\end{bmatrix}=\mathbf{0}. \tag{44}$$

where the coefficient $\mathcal{Q}_{w,k}$ is updated after each iteration, and is defined as

$$\mathcal{Q}_{w,k}=\mathcal{T}_{w,k}\mathcal{D}_{w,k}(1-\mathcal{L}_{w,k}), \tag{45}$$

and may become equal to 0 or 1. In the case that $\mathcal{L}_{w,k}=1$, $\mathcal{Q}_{w,k}$ becomes zero as this k vessel will be used as the reference value in the energy conservation equation. Coefficient $\mathcal{Q}_{w,k}$ also becomes zero when the flow reaches sonic conditions in a rarefaction or when the flow is supersonic and cannot be further accelerated with independence of the gradient of energy across the junction. In both cases, these ineligible vessels do not participate in energy conservation equation, as their solution becomes independent of the energy level of the other vessels.

The solution of the JRP is defined by the following system of $2N_P$ equations

$$\mathbf{E}^s(\mathbf{X})=\begin{bmatrix}(u^\bullet-u^n+g\mathcal{B})_1\mathcal{D}_{w,1}+du_1^\star(1-\mathcal{D}_{w,1})\\ \vdots\\ (u^\bullet-u^n+g\mathcal{B})_{N_P}\mathcal{D}_{w,N_P}+du_{N_P}^\star(1-\mathcal{D}_{w,N_P})\\ \sum_k g_k\left[\mathcal{D}_{w,k}(\alpha^\star A_o\ u^\bullet)_k+(1-\mathcal{D}_{w,k})Q_k^n\right]\\ \left[p_T^\bullet-p_{T,2}^\star\right]\mathcal{Q}_{w,2}+d\alpha_1^\star(1-\mathcal{D}_{w,1})\mathcal{L}_{w,2}\quad+d\alpha_2^\star(1-\mathcal{D}_{w,2})\\ \vdots\\ \left[p_T^\bullet-p_{T,N_P}^\star\right]\mathcal{Q}_{w,N_P}+d\alpha_1^\star(1-\mathcal{D}_{w,1})\mathcal{L}_{w,N_P}+d\alpha_{N_P}^\star(1-\mathcal{D}_{w,N_P})\end{bmatrix}=\mathbf{0}. \tag{46}$$

System of equations in (46) is indirectly solved here using an equivalent linear system as in (35), where the number of unknowns and original equations is reduced to $2N_P-\sum_k\mathcal{R}_{w,k}-2\sum_k(1-\mathcal{D}_{w,k})$. Therefore, the iterative search of the solution will have to deal with two situations, $\mathcal{D}_{w,k}=0$ and $\mathcal{R}_{w,k}=1$. When $\mathcal{D}_{w,k}=0$ for vessel k, the linearized system will ensure that $\mathbf{U}_k^\star=\mathbf{U}_k^n$ by returning $\delta u_k^{\star,m}=0$ and $\delta\alpha_k^{\star,m}=0$. When $\mathcal{R}_{w,k}=1$ for vessel k, the linearized system will return $\delta u_k^\star=0$, as the solution will be provided by $\alpha^\star$. In order to satisfy these requirements, the following matrix $\mathbf{J}_{\mathbf{E}^s}(\mathbf{X})$, based on the analytical Jacobian of the system of equations in (46) is defined as

$$\mathbf{J}_{\mathbf{E}^s}(\mathbf{X})=\begin{bmatrix}\mathbf{J}_{\mathbf{E}^s,\mathbf{1}} & \mathbf{J}_{\mathbf{E}^s,\mathbf{2}}\\ \mathbf{J}_{\mathbf{E}^s,\mathbf{3}} & \mathbf{J}_{\mathbf{E}^s,\mathbf{4}}\end{bmatrix}_{(2N_P)\times(2N_P)}=\begin{bmatrix}e_{1,1} & \cdots & e_{1,2N_P}\\ \vdots & \ddots & \vdots\\ e_{2N_P,1} & \cdots & e_{2N_P,2N_P}\end{bmatrix}. \tag{47}$$

Matrices $\mathbf{J}_{\mathbf{E}^s,\mathbf{1}}$ and $\mathbf{J}_{\mathbf{E}^s,\mathbf{2}}$ are given by

$$\mathbf{J}_{\mathbf{E^s},\mathbf{1}} = \mathbf{I}_{N_P\times N_P}\begin{bmatrix} 1-\mathcal{D}_{w,1}\mathcal{R}_{w,1} \\ \vdots \\ 1-\mathcal{D}_{w,k}\mathcal{R}_{w,k} \\ \vdots \\ 1-\mathcal{D}_{w,N_P}\mathcal{R}_{w,N_P} \end{bmatrix}, \quad \mathbf{J}_{\mathbf{E^s},\mathbf{2}} = \mathbf{I}_{N_P\times N_P}\begin{bmatrix} \mathcal{D}_{w,1}a_1 \\ \vdots \\ \mathcal{D}_{w,k}a_k \\ \vdots \\ \mathcal{D}_{w,N_P}a_{N_P} \end{bmatrix}, \tag{48}$$

with

$$a_k = g_k\left(\mathcal{R}_w\frac{\partial c}{\partial\alpha}+\frac{\partial\mathcal{B}}{\partial\alpha}\right)_k. \tag{49}$$

Matrix $\mathbf{J}_{\mathbf{E^s},\mathbf{3}}$ is split into three matrices $\mathbf{J}_{\mathbf{E^s},\mathbf{3}} = \mathbf{J}^a_{\mathbf{E^s},\mathbf{3}} + \mathbf{J}^b_{\mathbf{E^s},\mathbf{3}} + \mathbf{J}^c_{\mathbf{E^s},\mathbf{3}}$. Matrix $\mathbf{J}^a_{\mathbf{E^s},\mathbf{3}}$ is of the form

$$\mathbf{J}^a_{\mathbf{E^s},\mathbf{3}} = \begin{bmatrix} g_1\ b_1 & g_2\ b_2 & \cdots & g_{N_P}\ b_{N_P} \\ \rho(\mathcal{L}_w u^\star)_1\mathcal{Q}_{w,2} & \rho(\mathcal{L}_w u^\star)_2\mathcal{Q}_{w,2} & \cdots & \rho(\mathcal{L}_w u^\star)_{N_P}\mathcal{Q}_{w,2} \\ \vdots & \vdots & & \vdots \\ \rho(\mathcal{L}_w u^\star)_1\mathcal{Q}_{w,N_P} & \rho(\mathcal{L}_w u^\star)_2\mathcal{Q}_{w,N_P} & \cdots & \rho(\mathcal{L}_w u^\star)_{N_P}\mathcal{Q}_{w,N_P} \end{bmatrix}_{N_P\times N_P}, \tag{50}$$

with

$$b_k = (\mathcal{T}_w\mathcal{D}_w\alpha^\star A_o)_k, \tag{51}$$

and

$$\mathbf{J}^b_{\mathbf{E^s},\mathbf{3}} = \begin{bmatrix} 0 & 0 & \cdots & 0 \\ 0 & \rho u_2^\star(\mathcal{L}_{w,2}-1)\mathcal{Q}_{w,2} & \cdots & 0 \\ \vdots & 0 & \ddots & 0 \\ 0 & 0 & \cdots & \rho u^\star_{N_P}(\mathcal{L}_{w,N_P}-1)\mathcal{Q}_{w,N_P} \end{bmatrix}_{N_P\times N_P}. \tag{52}$$

Matrix $\mathbf{J}^c_{\mathbf{E^s},\mathbf{3}}$ is given by

$$\mathbf{J}^c_{\mathbf{E^s},\mathbf{3}} = \begin{bmatrix} 0 & 0 & \cdots & 0 \\ \mathcal{R}_{w,1}\mathcal{D}_{w,1}\mathcal{L}_{w,2} & \mathcal{R}_{w,2}\mathcal{D}_{w,2} & \cdots & 0 \\ \vdots & 0 & \ddots & 0 \\ \mathcal{R}_{w,1}\mathcal{D}_{w,1}\mathcal{L}_{w,N_P} & 0 & \cdots & \mathcal{R}_{w,N_P}\mathcal{D}_{w,N_P} \end{bmatrix}_{N_P\times N_P}, \tag{53}$$

and is defined to return $\delta u_k^{\star,m} = 0$ for those k vessels with $\mathcal{R}_{w,k} = 1$ where sonic conditions are reached.

Matrix $\mathbf{J}_{\mathbf{E^s},\mathbf{4}}$ is decomposed in $\mathbf{J}_{\mathbf{E^s},\mathbf{4}} = \mathbf{J}^a_{\mathbf{E^s},\mathbf{4}} + \mathbf{J}^b_{\mathbf{E^s},\mathbf{4}} + \mathbf{J}^c_{\mathbf{E^s},\mathbf{4}}$, with

$$\mathbf{J}^{a}_{\mathbf{E^s},\mathbf{4}} = \begin{bmatrix} g_1\, v_1 & g_2\, v_2 & \cdots & g_{N_P}\, v_{N_P} \\ \left(\mathcal{L}_w K_o \frac{\partial \sigma}{\partial \alpha}\right)_1 \mathcal{Q}_{w,2} & \left(\mathcal{L}_w K_o \frac{\partial \sigma}{\partial \alpha}\right)_2 \mathcal{Q}_{w,2} & \cdots & \left(\mathcal{L}_w K_o \frac{\partial \sigma}{\partial \alpha}\right)_{N_P} \mathcal{Q}_{w,2} \\ \vdots & \vdots & \vdots & \vdots \\ \left(\mathcal{L}_w K_o \frac{\partial \sigma}{\partial \alpha}\right)_1 \mathcal{Q}_{w,N_P} & \left(\mathcal{L}_w K_o \frac{\partial \sigma}{\partial \alpha}\right)_2 \mathcal{Q}_{w,N_P} & \cdots & \left(\mathcal{L}_w K_o \frac{\partial \sigma}{\partial \alpha}\right)_{N_P} \mathcal{Q}_{w,N_P} \end{bmatrix}_{N_P \times N_P}, \tag{54}$$

with

$$v_k = (A_o \mathcal{D}_w)_k \left[\mathcal{T}_w u^{\star} + g_k \mathcal{R}_w \frac{\partial (c\alpha)^{\star}}{\partial \alpha} \right]_k, \tag{55}$$

and

$$\mathbf{J}^{b}_{\mathbf{E^s},\mathbf{4}} = \begin{bmatrix} 0 & 0 & \cdots & 0 \\ 0 & \left(K_o \frac{\partial \sigma}{\partial \alpha}\right)_2 (\mathcal{L}_{w,2} - 1) \mathcal{Q}_{w,2} & \cdots & 0 \\ \vdots & 0 & \ddots & 0 \\ 0 & 0 & \cdots & \left(K_o \frac{\partial \sigma}{\partial \alpha}\right)_{N_P} (\mathcal{L}_{w,N_P} - 1) \mathcal{Q}_{w,N_P} \end{bmatrix}_{N_P \times N_P}. \tag{56}$$

Matrix $\mathbf{J}^{c}_{\mathbf{E},\mathbf{4}}$, given by

$$\mathbf{J}^{c}_{\mathbf{E^s},\mathbf{4}} = \begin{bmatrix} 0 & 0 & \cdots & 0 \\ (1 - \mathcal{D}_{w,1}) \mathcal{L}_{w,2} & (1 - \mathcal{D}_{w,2}) & \cdots & 0 \\ \vdots & 0 & \ddots & 0 \\ (1 - \mathcal{D}_{w,1}) \mathcal{L}_{w,N_P} & 0 & \cdots & (1 - \mathcal{D}_{w,N_P}) \end{bmatrix}_{N_P \times N_P}, \tag{57}$$

and is defined to return $\delta \alpha_k^{\star,m} = 0$ for those outflow sections where supersonic conditions are initially imposed and the solution will not change in time.

The iterative search of the solution start defining $\alpha_k^{\star,m} = \alpha_k^n$ and $u_k^{\star,m} = u_k^n$ in the first iteration with $m = 0$. For each k vessel where initial supersonic conditions are imposed, $SI_{g,k}^n \geq 1$, only flow variations are allowed when $\mathcal{D}_{w,k} = 1$, and therefore it becomes necessary to estimate an initial value of $Q_k^{\star,m}$ different from Q_k^n at the first iteration with $m = 0$. Here, this initial estimation is computed as the sum of the flow contributions to the junction provided by the rest of vessels with $SI_g^n < 1$, as follows

$$Q_k^{\star,m=0} = g_k \left[- \sum_{\left(SI_{g,k}\right)_i^n < 1} g_i Q_i^n \right], \quad \left(SI_g\right)_k^n \geq 1 \tag{58}$$

allowing the transmission of backward waves through the confluence.

In order to avoid an excessive variation of α between two iterations and ensure convergence to the solution, we reduce the step size $\delta \mathbf{X}^m$ by using two damping factors $\gamma_{\alpha_{\min}} \leq 1$ and $\gamma_{u_{\min}} \leq 1$. Damping factor $\gamma_{\alpha_{\min}} \leq 1$ selected as the minimum among the damping factors $\gamma_{\alpha,k}$ defined for each k vessel of the junction

$$\delta\mathbf{X}^m = \gamma_{\alpha_{\min}}\ \delta\mathbf{X}^m,\ \ \gamma_{\alpha_{\min}} = \min\{\gamma_{\alpha,k}\},\quad \gamma_{\alpha,k} = \begin{cases} 1 & if\ |\delta\alpha_k^{\star,m}| < \delta\alpha_{lim} \\ \dfrac{\delta\alpha_{lim}}{|\delta\alpha_k^{\star,m}|} & if\ |\delta\alpha_k^{\star,m}| > \delta\alpha_{lim} \end{cases}, \tag{59}$$

with $\delta\alpha_{lim}$ a constant value, defined to limit the variation of α. Next, the updating step $\delta\mathbf{X}^m$ is corrected again by using another damping factor, $\gamma_{u_{\min}} \leq 1$, selected as the minimum among the damping factors $\gamma_{u,k}$ defined for each k vessel of the junction

$$\delta\mathbf{X}^m = \gamma_{u_{\min}}\ \delta\mathbf{X}^m,\ \ \gamma_{u_{\min}} = \min\{\gamma_{u,k}\},\quad \gamma_{u,k} = \begin{cases} 1 & if\ |\delta u^{\star,m}| < \delta u_{lim,k} \\ \dfrac{\delta u_{lim,k}}{|\delta u^{\star,m}|} & if\ |\delta u^{\star,m}| > \delta u_{lim,k} \end{cases}, \tag{60}$$

where $\delta u_{lim,k}$ is not a fixed value. Parameter $\delta u_{lim,k}$ is computed assuming that the increase in speed index $SI_{g,k}$ between two iterations, $\left|\delta SI_{g,k}^{\star,m}\right| = \left|SI_{g,k}^{\star,m+1} - SI_{g,k}^{\star,m}\right|$, is small and small enough to control the solution when the solution is in the vicinity of sonic flow conditions. The maximum variation of velocity in vessel k is approximated by

$$\delta u_{lim,k} = \left|\delta SI_{g,k}^m\right| c_k^{\star,m} \tag{61}$$

with

$$\left|\delta SI_{g,k}^{\star,m}\right| = \begin{cases} \min\left(\delta SI_{lim}, \left|1 - \left|SI_{g,k}^{\star,m}\right|\right|\right) & \text{if } 0 \leq SI_{g,k}^{\star,m} < 1 \\ \delta SI_{lim} & \text{otherwise} \end{cases}, \tag{62}$$

where variation of the seep index is limited by a prefixed constant value, δSI_{lim}, that can be further reduced to avoid sonic conditions when $0 \leq SI_{g,k}^{\star,m} < 1$.

Once the new value of $\mathbf{X}^{m+1}$ is computed, the values of $\mathcal{R}_{w,k}^{m+1}$, $\mathcal{T}_{w,k}^{m+1}$ and $\mathcal{D}_{w,k}^{m+1}$ are updated, and the velocity and vessel deformation are defined as

$$u_k^{\star,m+1} = u_k^{\bullet,m+1}\mathcal{D}_{w,k}^{m+1} + u_k^n\left(1 - \mathcal{D}_{w,k}^{m+1}\right),\ \ \alpha_k^{\star,m+1} = \alpha_k^{\star,m+1}\mathcal{D}_{w,k}^{m+1} + \alpha_k^n\left(1 - \mathcal{D}_{w,k}^{m+1}\right), \tag{63}$$

until the desired level of error is achieved.

2.3 | 0D valve model

The presence of valves results in changes in resistance to flow. The valve represented in Figure 1, between vessels k_1 and k_2, generates a pressure drop, Δp_v, between two vessels described by the following 0D equation[36]

$$L_v\frac{dQ_v}{dt} = \Delta p_v - R_v Q_v - B_v Q_v|Q_v|, \tag{64}$$

where Q_v is the flow through the valve. The coefficients are a linear resistance R_v, a quadratic resistance B_v and the inertance L_v, given by

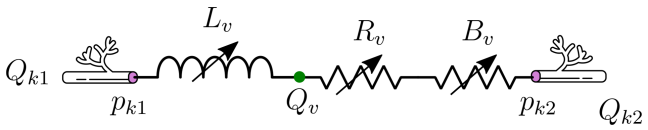

FIGURE 1 Lumped parameter model for a valve.

$$R_v = \frac{8\pi\mu l_e}{A_e^2} \quad B_v = \frac{\rho}{2(K_d A_e)^2}, \quad L_v = \frac{\rho l_e}{A_e}, \tag{65}$$

with A_e and l_e, the effective valve area and length respectively and K_d a discharge coefficient. When the valves open allow blood to flow from upstream vessel $k1$ to downstream vessel $k2$, and if they close, they stop the blood from flowing backwards, unless back flow in regurgitant valves is allowed. An index of valve state $(0 \leq \zeta \leq 1)$ is used to define the actual opening of the valve[36]

$$A_e(t) = (A_{e,max} - A_{e,min})\zeta(t) + A_{e,min}, \tag{66}$$

where $A_{e,max}$ and $A_{e,min}$ are the maximum and minimum effective orifice areas that the valve can achieve. To account for valve regurgitation or stenosis, $A_{e,max}$ and $A_{e,min}$ are defined as

$$A_{e,min} = M_{rg} A_{an}, \quad A_{e,max} = M_{st} A_{an}, \tag{67}$$

where $0 \leq M_{rg} \leq 1$ and $0 \leq M_{st} \leq 1$ are constant parameters used to represent two important functional properties of the valve, and A_{an} is the annulus area. When $M_{rg} = 0$ and $M_{st} = 1$ the valve closes and opens to full capacity, representing a healthy valve. A regurgitant valve is defined by $M_{rg} > 0$. Stenosis is represented by $M_{st} < 1$ and the extreme case of $M_{st} = 0$ corresponds to valve atresia or complete obstruction to flow. The valve opening $\zeta(t)$ in time is given by

$$\frac{d\zeta}{dt} = \begin{cases} (1-\zeta)K_{vo}(\Delta p_v - \Delta p_o) & if \quad \Delta p_v \geq \Delta p_{vo} \\ \zeta K_{vc}(\Delta p_v - \Delta p_o) & if \quad \Delta p_v < \Delta p_{vo} \end{cases} \tag{68}$$

where K_{vo} and K_{vc} are rate coefficients for valve opening and closing, respectively. Δp_{vo} is a reference pressure gradient. In venous valves annulus area A_{an} can be defined as a multiple of the reference cross-sectional area of the upstream vein $k = 1$, $A_{an} = \beta_A A_{o.}$[41] The effective valve length can be defined as a multiple of the venous reference radius of the upstream vein $k = 1$, $l_e = \beta_l r_{o.}$[41]

The solution of the JRP in (46) for two vessels, is adapted in Section 2.3.1 to include the dissipation of energy across a valve given by the lumped model in (64). This problem will be named the Valve Riemann Problem (VRP).

2.3.1 | Numerical solution of the VRP

The solution of the VRP depends on the pressure drop across the valve in (64) between two vessels, $N_p = 2$. In the VRP, the valve will located between two vessels with $g_{k1} = 1$ and $g_{k2} = -1$, leading to an outflow/inflow boundary section respectively. The Riemann problem at valve or VRP, for two infinitely long converging vessels sharing a valve is defined as the following set of IVP's,

$$\frac{\partial \mathbf{U}_k}{\partial t} + \frac{\partial \mathbf{F}_\varphi}{\partial x}(\mathbf{U}_k) = \mathbf{S}_{\chi,k}, \quad \mathbf{U}_k(x,0) = \mathbf{U}_k^n, \tag{69}$$

for $k = k_1, k_2$, together with the following vector of coupling conditions

$$\mathbf{\Phi}_V\left(\mathbf{U}_0^\star,...,\mathbf{U}_{N_P}^\star\right)=\begin{bmatrix}\sum_k[g(\alpha^\star A_o\ u^\star)]_k\\ p_{T,k1}^\star-p_{T,k2}^\star-\Delta p_v{}^{n+1}\\ \vdots\\ Q_{k1}^\star-Q_v^\star\end{bmatrix}=\mathbf{0}, \tag{70}$$

involving the energy dissipation across the valve, Δp_v, and the continuity equation for the flow across the valve Q_v, where the initial flow conditions across the valve, Q_v^n, can be different from Q_{k1}^n and Q_{k2}^n.

The solution of the VRP will be defined by a system of 5 equations, $\mathbf{E}^V(\mathbf{X})=0$, that will be solved using Picard iterations between times t and $t+\Delta t$. The system of equations is intended to perform not only under subsonic conditions, but also under sonic and supersonic conditions, with

$$\mathbf{E}^V(\mathbf{X})=\begin{bmatrix}(u^\star-u^n+g\mathcal{B})_{k1}\mathcal{D}_{w,k1}+du_{k1}^\star(1-\mathcal{D}_{w,k1})\\ (u^\star-u^n+g\mathcal{B})_{k2}\mathcal{D}_{w,k2}+du_{k2}^\star(1-\mathcal{D}_{w,k2})\\ \sum_k(g\ u^\star\alpha^\star A_o)_k\mathcal{D}_{w,k}+\sum_k g_k[(1-\mathcal{D}_w)(Au)^n]_k\\ \left[p_{T,k1}^\star-p_{T,k2}^\star-\Delta p_v\right]\mathcal{Q}_{w,k2}+d\alpha_{k1}(1-\mathcal{D}_{w,k1})+d\alpha_{k2}^\star(1-\mathcal{D}_{w,k2})\\ (u^\star\alpha^\star A_o)_{k1}\mathcal{D}_{w,k1}-Q_v^\star+(1-\mathcal{D}_{w,k1})Q_{k1}^n\end{bmatrix}, \tag{71}$$

and

$$\mathbf{X}=\left[u_{k1}^\star,\ u_{k2}^\star,\ \alpha_{k1}^\star,\ \alpha_{k2}^\star,\ Q_v^\star\right], \tag{72}$$

where Δp_v is numerically integrated here using an implicit discretization using $Q_v^\star$ as flow rate in the time interval t^n to t^{n+1}

$$\Delta p_v^{n+1}=\left(\frac{L_v^\star}{\Delta t}+R_v^\star+B_v^\star\left|Q_v^\star\right|\right)^{n+1}Q_v^\star-\left(\frac{L_v^\star}{\Delta t}\right)^{n+1}Q_v^n. \tag{73}$$

The first two equations in $\mathbf{E}^V(\mathbf{X})$ are relations for non-linear waves for both connecting vessels, followed by the mass conservation equation, the energy conservation equation, and a continuity equation for the flow across the valve. Energy losses produced in the valve depend on the level of total energy of the connecting vessels p_T to guarantee exact equilibrium under hydrostatic and non-hydrostatic equilibrium conditions. The continuity equation for the flow across the valve is modified ensuring that Q_v is limited by the constraints defined for the flow in vessel k_1. $\mathbf{E}^V(\mathbf{X})$ is defined to impose conservation of the initial value conditions in a k vessel depending on the dynamic parameter $\mathcal{D}_{w,k}$.

System of equations in (71) is indirectly solved using a equivalent linear system with

$$\mathbf{J}_{\mathbf{E}^V}(\mathbf{X})=\begin{bmatrix}\mathbf{J}_{\mathbf{E}^V,\mathbf{1}} & \mathbf{J}_{\mathbf{E}^V,\mathbf{2}}\\ \mathbf{J}_{\mathbf{E}^V,\mathbf{3}} & \mathbf{J}_{\mathbf{E}^V,\mathbf{4}}\end{bmatrix}, \tag{74}$$

where

$$\mathbf{J}_{\mathbf{E}^{\mathrm{v}},\mathbf{1}} = \begin{bmatrix} 1-\mathcal{D}_{w,k1}\mathcal{R}_{w,k1} & 0 \\ 0 & 1-\mathcal{D}_{w,k2}\mathcal{R}_{w,k2} \end{bmatrix}, \quad \mathbf{J}_{\mathbf{E}^{\mathrm{v}},\mathbf{2}} = \begin{bmatrix} \mathcal{D}_{w,k1}a_{k1} & 0 & 0 \\ 0 & \mathcal{D}_{w,k2}a_{k2} & 0 \end{bmatrix}. \tag{75}$$

Matrix $\mathbf{J}_{\mathbf{E},\mathbf{3}}$ is split in $\mathbf{J}_{\mathbf{E},\mathbf{3}} = \mathbf{J}^{a}_{\mathbf{E},\mathbf{3}} + \mathbf{J}^{b}_{\mathbf{E},\mathbf{3}} + \mathbf{J}^{c}_{\mathbf{E},\mathbf{3}}$, with

$$\mathbf{J}^{a}_{\mathbf{E}^{\mathrm{v}},\mathbf{3}} = \begin{bmatrix} g_{k1} & b_{k1} & g_{k2} & b_{k2} \\ \rho(\mathcal{L}_w u^{\star})_{k1}\mathcal{Q}_{w,k2} & & \rho(\mathcal{L}_w u^{\star})_{k2}\mathcal{Q}_{w,k2} & \\ b_{k1} & & 0 & \end{bmatrix}, \quad \mathbf{J}^{b}_{\mathbf{E}^{\mathrm{v}},\mathbf{3}} = \begin{bmatrix} 0 & 0 \\ 0 & \rho u^{\star}_{k2}(\mathcal{L}_{w,k2}-1)\mathcal{Q}_{w,k2} \\ 0 & 0 \end{bmatrix}, \tag{76}$$

and

$$\mathbf{J}^{c}_{\mathbf{E}^{\mathrm{v}},\mathbf{3}} = \begin{bmatrix} 0 & 0 \\ (1-\mathcal{T}_{w,k1})\mathcal{D}_{w,k1}\mathcal{L}_{w,k2} & (1-\mathcal{T}_{w,k2})\mathcal{D}_{w,k2} \\ 0 & 0 \end{bmatrix}. \tag{77}$$

Matrix $\mathbf{J}_{\mathbf{E}^{\mathrm{v}},\mathbf{4}}$ is split in $\mathbf{J}_{\mathbf{E}^{\mathrm{v}},\mathbf{4}} = \mathbf{J}^{a}_{\mathbf{E}^{\mathrm{v}},\mathbf{4}} + \mathbf{J}^{b}_{\mathbf{E}^{\mathrm{v}},\mathbf{4}} + \mathbf{J}^{c}_{\mathbf{E}^{\mathrm{v}},\mathbf{4}} + \mathbf{J}^{d}_{\mathbf{E},\mathbf{4}}$, where

$$\mathbf{J}^{a}_{\mathbf{E}^{\mathrm{v}},\mathbf{4}} = \begin{bmatrix} g_{k1} & v_{k1} & g_{k2} & v_{k2} & 0 \\ \left(\mathcal{L}_w K_o \frac{\partial\sigma}{\partial\alpha}\right)_{k1}\mathcal{Q}_{w,k2} & & \left(\mathcal{L}_w K_o \frac{\partial\sigma}{\partial\alpha}\right)_{k2}\mathcal{Q}_{w,k2} & & 0 \\ v_{k1} & & 0 & & 0 \end{bmatrix}, \quad \mathbf{J}^{b}_{\mathbf{E}^{\mathrm{v}},\mathbf{4}} = \begin{bmatrix} 0 & 0 & 0 \\ 0 & \left(K_o \frac{\partial\sigma}{\partial\alpha}\right)_{k2}(\mathcal{L}_{w,k2}-1)\mathcal{Q}_{w,k2} & 0 \\ 0 & 0 & 0 \end{bmatrix} \tag{78}$$

and

$$\mathbf{J}^{c}_{\mathbf{E}^{\mathrm{v}},\mathbf{4}} = \begin{bmatrix} 0 & 0 & 0 \\ (1-\mathcal{D}_{w,k1})\mathcal{L}_{w,k2} & (1-\mathcal{D}_{w,k2}) & 0 \\ 0 & 0 & 0 \end{bmatrix}, \quad \mathbf{J}^{d}_{\mathbf{E},\mathbf{4}} = \begin{bmatrix} 0 & 0 & 0 \\ 0 & 0 & -d_v\mathcal{Q}_{w,2} \\ 0 & 0 & -1 \end{bmatrix}. \tag{79}$$

where

$$d_v = \left(\frac{L^{\star}_v}{\Delta t} + R^{\star}_v + 2B^{\star}_v \left|Q^{\star}_v\right|\right). \tag{80}$$

After each Picard iteration the valve index ζ is updated first, using auxiliary variable

$$\Delta p^{\zeta}_v = p^{m+1}_{T,2} - p^{m+1}_{T,1}. \tag{81}$$

If the valve is opening, $\Delta p^{\zeta}_v - \Delta p_{vo} \geq 0$, valve state is discretized as follows

$$\frac{\Delta\zeta}{\Delta t}=\frac{\zeta^{n+1,m+1}-\zeta^{n}}{\Delta t}=\left(1-\zeta^{n+1,m+1}\right)K_{vo}\ \left(\Delta p_v^{\zeta}-\Delta p_{vo}\right) \tag{82}$$

leading to

$$\zeta^{n+1,m+1}=\frac{\zeta^{n}+K_{vo}\ \left(\Delta p_v^{\zeta}-\Delta p_{vo}\right)\Delta t}{1+K_{vo}\ \left(\Delta p_v^{\zeta}-\Delta p_{vo}\right)\Delta t} \tag{83}$$

ensuring always $\zeta^{n+1,m+1}\leq 1$. If the valve closes, $\Delta p_v^{\zeta}-\Delta p_{vo}<0$, valve index is discretized as follows

$$\frac{\Delta\zeta}{\Delta t}=\zeta^{n+1,m+1}K_{vc}\ \left(\Delta p_v^{\zeta}-\Delta p_{vo}\right) \tag{84}$$

equivalent to

$$\zeta^{n+1,m+1}=\frac{\zeta^{n}}{1-K_{vo}\ \left(\Delta p_v^{\zeta}-\Delta p_{vo}\right)\Delta t} \tag{85}$$

ensuring always $\zeta^{n+1,m+1}\geq 0$. Now effective area is computed as

$$A_e^{n+1,m+1}=(A_{e,max}-A_{e,min})\zeta^{n+1,m+1}+A_{e,min}, \tag{86}$$

and the valve parameters (65, 66) and the pressure drop in (73) are updated

$$\Delta p_v^{n+1,m+1}=\left(\frac{L_v^{\star,m+1}}{\Delta t}+R_v^{\star,m+1}+B_v^{\star,m+1}\left|Q_v^{\star,m+1}\right|\right)^{n+1}Q_v^{\star,m+1}-\left(\frac{L_v^{\star,m+1}}{\Delta t}\right)^{n+1}Q_v^{n}. \tag{87}$$

2.3.2 | Numerical experiments in the VRP

In the numerical experiments presented in this section, two infinitely large and frictionless vessels $k1$ and $k2$, defined in $(-\infty<x\leq 0)$ and $(0\leq x<\infty)$ respectively are connected by a valve located at $x=0$. In both vessels, the boundary conditions are in equilibrium with the initial conditions and do not participate in the evolution of the problem solution. Unlike the JRP, where no flow resistance is considered, in this set of VRP's the valve produces a pressure drop and energy dissipation occurs. Therefore, the exact solution of the VRP is not self-similar and cannot be calculated analytically. Therefore, the proposed numerical solutions are compared with the exact solutions of the equivalent JRP, in which the presence of the valve is omitted.

Mechanical and geometrical properties of both vessels in all numerical experiments are identical and given by reference diameter $d_{o,k}=30.500$ mm, reference pulse wave velocity $c_{o,k}=200.0$ cm s^{-1}, reference pressure $p_{o,k}=0$ mmHg, $m_\sigma=10$ and $m_\sigma=-3/2$. Initial conditions in each test case are presented in Table 1, providing for the left ($k=1$) and right ($k=2$) vessels the value of g_k depending on the position of the terminal cell, the external pressure $p_{e,k}$, the initial speed index $SI^n=u_k^n/c_k^n$ and initial relative area α_k^n at $t=0$.

In all cases reported in this work, density is $\rho=1$ g/cm^3 and friction forces are not considered in the vessels. Viscous energy dissipation is produced only in the valves where $\mu=0.0450$ g/cm/s. In all numerical simulations the CFL parameter will be set constant with CFL $=0.5$, and two levels of mesh refinement will be tested, $\Delta x=0.1$ cm and $\Delta x=0.01$ cm. Valve parameters are constant and given by: $M_{rg}=0.0$, $M_{st}=1.0$, $K_d=1.0$, $\beta_l=1.0$ $\beta_A=0.65$, $k_{vo}=0.03$ (cm s/g), $k_{vc}=0.03$ (cm s/g) and $dp_{vo}=0.0$. The numerical solutions also depend on the initial conditions for the flow across the valve Q_v and on the initial state of opening index ζ.

TABLE 1 VRP configuration.

Test case	k	g_k	$p_{e,k}$	SI	α	ζ
VRP1	1	1	0.0	0.00	1.100	1
	2	−1	0.0	0.00	1.000	
VRP2	1	1	0.0	0.00	1.100	1
	2	−1	0.0	0.00	0.200	
VRP4	1	1	0.0	0.00	1.100	0
	2	-1	−30.0	0.00	0.200	
VRP5	1	1	0.0	1.10	1.100	1
	2	−1	0.0	0.00	0.200	
VRP11	1	1	0.0	0.00	0.200	1
	2	−1	0.0	0.00	1.100	
VRP13	1	1	0.0	0.00	0.200	1
	2	−1	0.0	−1.10	1.100	
VRP15	1	1	0.0	−1.10	0.200	1
	2	−1	0.0	−1.10	1.100	

Note: Test case, number of vessel k, father or daughter vessel g_k, external pressure $p_{e,k}$, initial speed index $SI^n = u_k^n/c_k^n$ and initial relative area α_k^n at $t = 0$.

Test cases will consider initially fully open valves with $\zeta(t=0)=1$ and $Q_v(t=0)=Q_{k1}(t=0)$ or fully closed valves with $\zeta(t=0)=0$ and $Q_v(t=0)=0$. Figures 2–14 provide in the upper part of each figure the numerical solution for VRP for vessel area, flow, SI and total pressure at $t=0.030$ s for vessels $k1$ and $k2$, using lines $(-\circ-)$ and $(-\circ-)$ respectively. The analytical solution of the equivalent JRP without the valve is also plotted using a black line $(-)$.

In addition, Figures 2–14 provide in the lower part of each figure, the solutions in time for flow across the valve Q_v, for the index of valve state ζ, for the ratios $R_v/R_v(\zeta=1)$, $B_v/B_v(\zeta=1)$, $L_v/L_v(\zeta=1)$, for the jump in total pressure between the terminal computational cells in left and right vessels $\Delta p_T = p_T(k_2) - p_T(k_1)$ and for the pressure drop across the valve Δp_v in (64).

In test case VRP1, the initial variation of energy produced by the variation in vessel deformation leads to a flow from left to right. When the analytical solution of the JRP is compared with the numerical solution of the VRP in Figure 2, the solution for flow in the JRP (with zero resistance), a backward decompression wave (BDW) and a forward compression wave (FCW), is slightly attenuated in the VRP as the valve exerts a small resistance over the flow. The valve is completely open during all time and the jump in total energy converges to the pressure drop in the valve when steady conditions are achieved and the flow across the valve become constant.

When the variation in the vessel deformation is enlarged in test case VRP2 (Figure 4), the analytical solution of the JRP and the numerical solution of the VRP reach almost sonic conditions and the flow across the valve is strongly increased. Valve resistance increases and the jump in total pressure converges to the pressure drop in the valve earlier than in test case VRP1, as seen in Figure 4.

In test case VRP4 (Figure 6) the initial conditions for area and flow in test case VR2 are kept, but now a suction is imposed in the downstream vessel, p_{ext} $(--)$, and the valve is initially closed. Both the analytical solution of the JRP and the numerical solution of the VRP reach sonic conditions for the upstream vessel $k1$ and the flow cannot be further increased by increasing the suction in vessel $k2$. The initial large variation of energy between vessels leads to a fast opening of the valve, and flow limitation appears. In consequence, the jump in total energy between the two vessels is larger than the pressure drop generated by the resistance of the valve.

A large variation in the vessel deformation together with supersonic conditions in the upstream vessel is imposed in the test case VRP5, being the valve initially opened. The valve resistance generates a subsonic backward compression wave (BCW) and supersonic conditions appear in the downstream vessel, as shown in Figure 8. Figure 8 shows that flow across the valve decreases in time and that in this case the initial value of the pressure drop across the valve is

larger than the difference in total pressure between the vessels. They converge to same value when steady flow conditions are achieved.

In absence of a valve, the initial conditions in test case VRP11 in Figure 10, would lead to a flow from right to left, but the valve, initially opened, closes stopping the blood from flowing backwards. As initial conditions consider flow at rest in both vessels, two perturbations arising from the fast valve closing travel upstream and downstream the valve, as observed in Figure 10. If test case VRP11 is modified and a supersonic backward flow is imposed in downstream vessel $k2$ in test case VRP13, the valve immediately closes (Figure 12), generating a FCW in the downstream vessel, and a small perturbation traveling in the left direction in the upstream vessel, as shown in Figure 12. If initial flow conditions are supersonic backward flow in all the domain, as in test case VRP15, Figure 14 shows how the valve closes again stopping backward flow, leading now to a BDW in the upstream vessel and to a FCW in the downstream vessel.

Figures 3, 5, 7, 9, 11, 13 and 15 provide the numerical solutions the VRP's in test cases 1, 2, 4, 11, 13 and 15 with $\Delta x = 0.1$ cm. In all cases the numerical solution is equal to the one provided when the cell size is reduced ten times, $\Delta x = 0.01$ cm. Differences arise as a consequence of the numerical diffusion produced by the first order Godunov method used here.

2.4 | 0D Windkessel models

Lumped-parameter or Windkessel models are 0D models used to describe the dynamics of the vascular beds (involving arterioles, capillaries and venules) by simplifying the governing equations of hemodynamics in local regions. Windkessel models usually assume constant values of resistance $R = R_o$, inertace $L = L_o$ and compliance $C = C_o$ for each single compartment and are combined to form peripheral beds that connect arteries to veins. In each compartments pressure is defined as

$$p(t) = p_{tr}(t) + p_e^{\oplus}(t), \tag{88}$$

where $p_e^{\oplus} = p_e + \rho g \eta$. The volume stored in each compartment, $V = V_e + V_u$, is expressed in terms of the stressed volume V_e and the unstressed volume V_u. The relation between transmural pressure and stressed volume is linear and given by

$$p_{tr} = p_o + \frac{1}{C_o} V_e = p_o + \frac{1}{C_o}(V - V_u), \tag{89}$$

where p_o is a reference value. Accordingly, total volume becomes

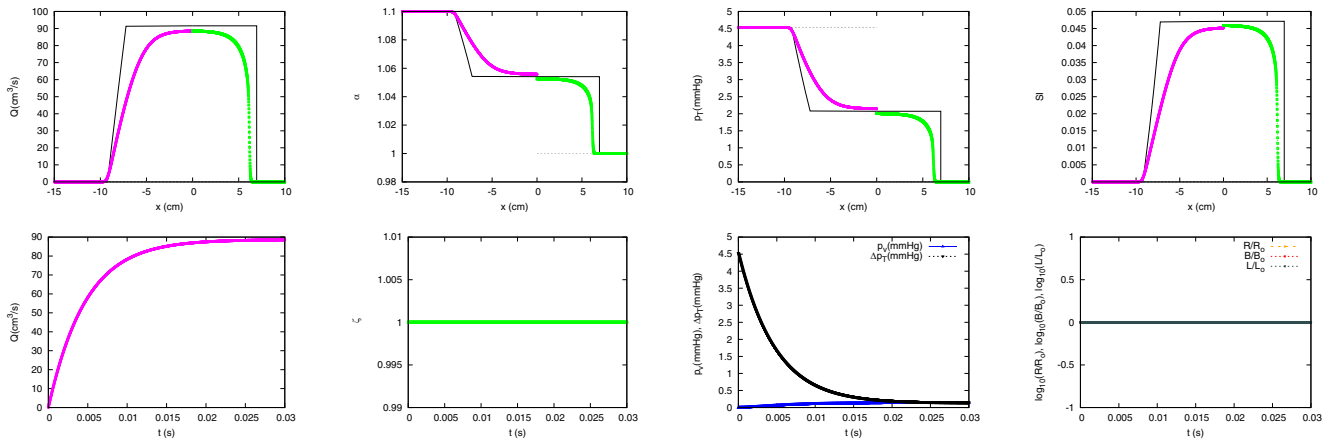

FIGURE 2 Section 2.3.2. Test VRP1. $\Delta x = 0.01$ cm. Initially open valve. Numerical solutions in space for vessels $k1$ and $k2$ located upstream and downstream the valve at $t = 0.030$ s (upper) and numerical solutions for the valve located at $x = 0$ in time (lower).

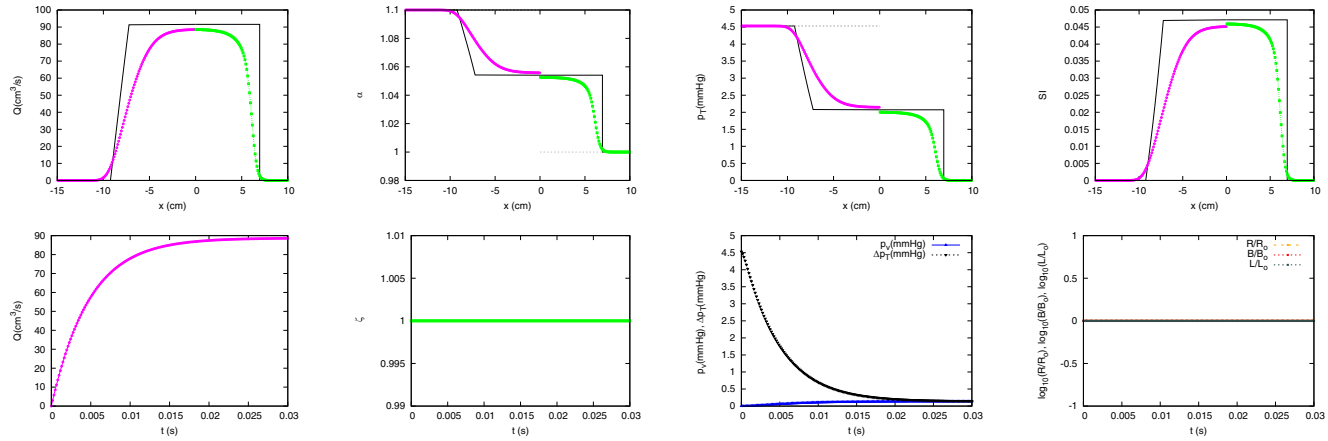

FIGURE 3 Section 2.3.2. Test VRP1. $\Delta x = 0.1$ cm. Initially open valve. Numerical solutions in space for vessels $k1$ and $k2$ located upstream and downstream the valve at $t = 0.030$ s (upper) and numerical solutions for the valve located at $x = 0$ in time (lower).

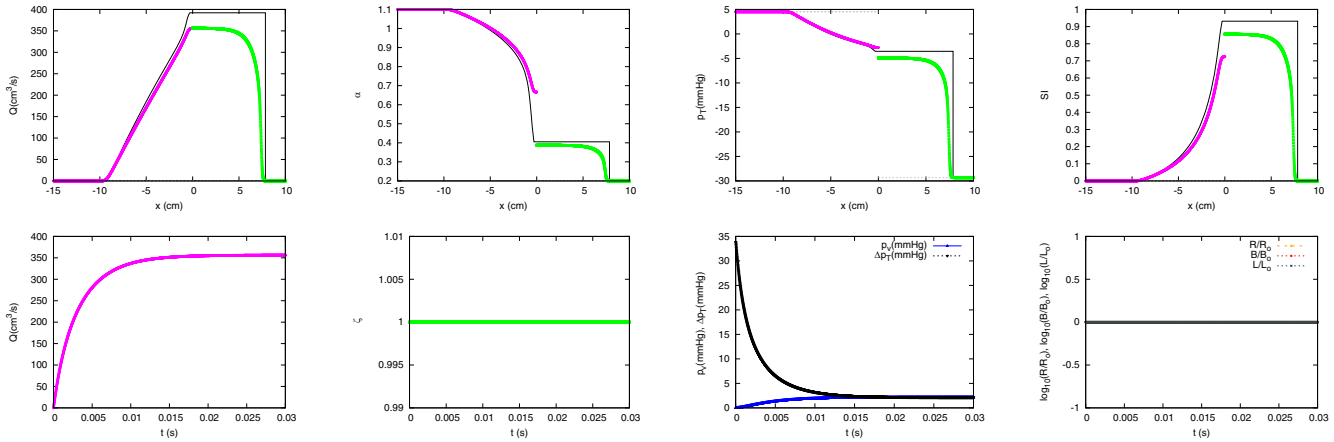

FIGURE 4 Section 2.3.2. Test VRP2. $\Delta x = 0.01$ cm. Initially open valve. Numerical solutions in space for vessels $k1$ and $k2$ located upstream and downstream the valve at $t = 0.030$ s (upper) and numerical solutions for the valve located at $x = 0$ in time (lower).

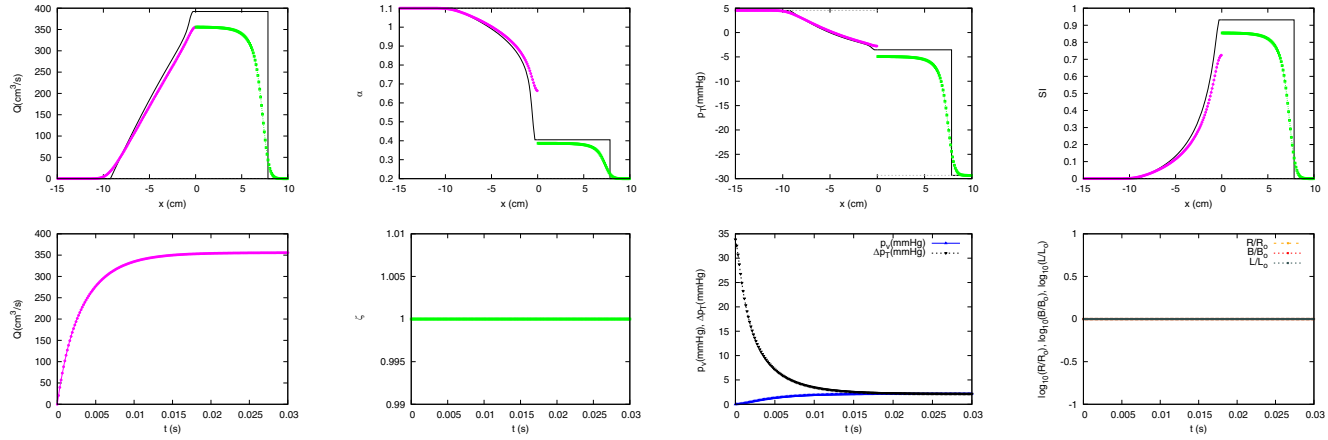

FIGURE 5 Section 2.3.2. Test VRP2. $\Delta x = 0.1$ cm. Initially open valve. Numerical solutions in space for vessels $k1$ and $k2$ located upstream and downstream the valve at $t = 0.030$ s (upper) and numerical solutions for the valve located at $x = 0$ in time (lower).

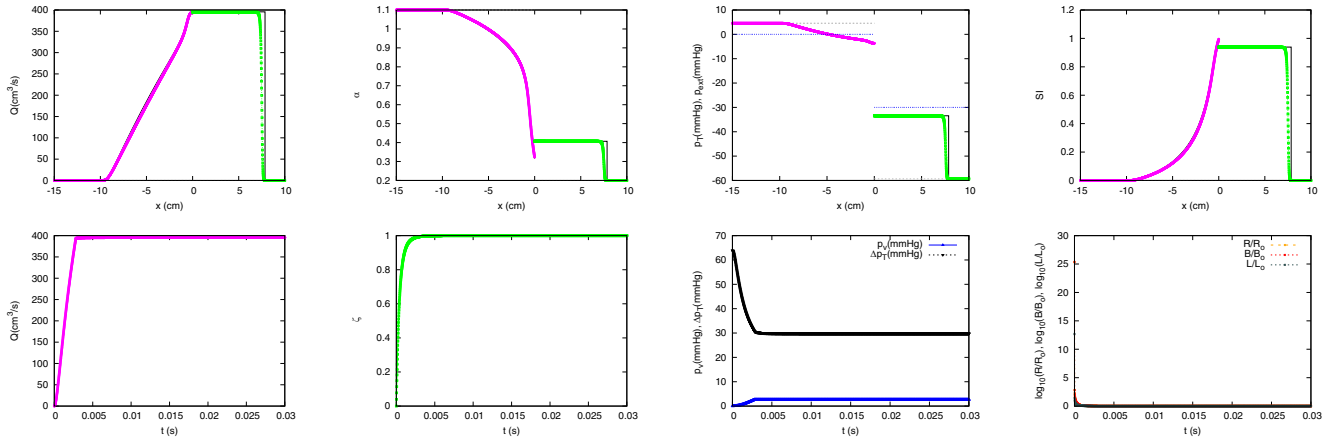

FIGURE 6 Section 2.3.2. Test VRP4. $\Delta x = 0.01$ cm. Initially closed valve. Numerical solutions and external pressure p_{ext} $(--)$ in space for vessels $k1$ and $k2$ located upstream and downstream the valve at $t = 0.030$ s (upper) and numerical solutions for the valve located at $x = 0$ in time (lower).

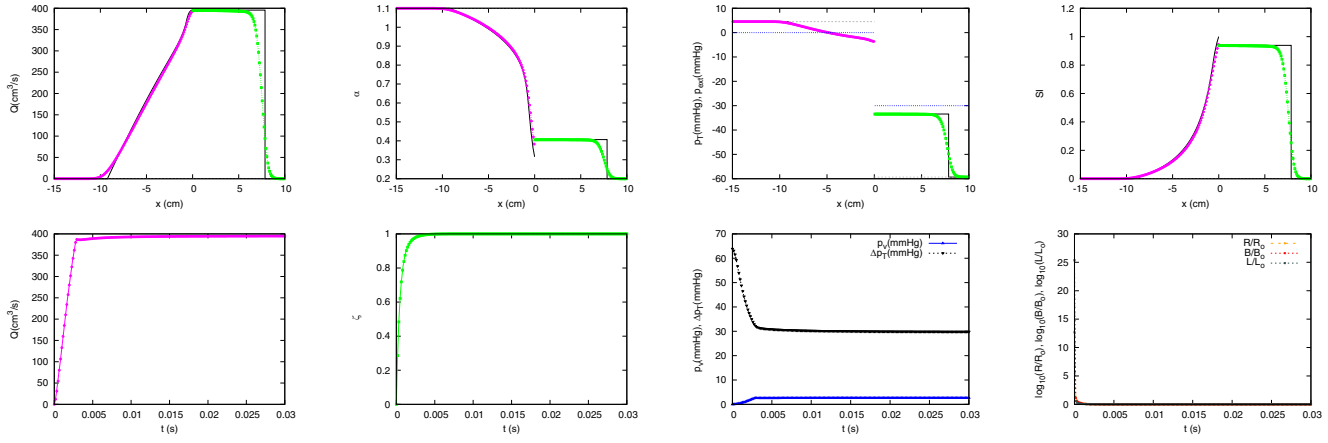

FIGURE 7 Section 2.3.2. Test VRP4. $\Delta x = 0.1$ cm. Initially closed valve. Numerical solutions and external pressure p_{ext} $(--)$ in space for vessels $k1$ and $k2$ located upstream and downstream the valve at $t = 0.030$ s (upper) and numerical solutions for the valve located at $x = 0$ in time (lower).

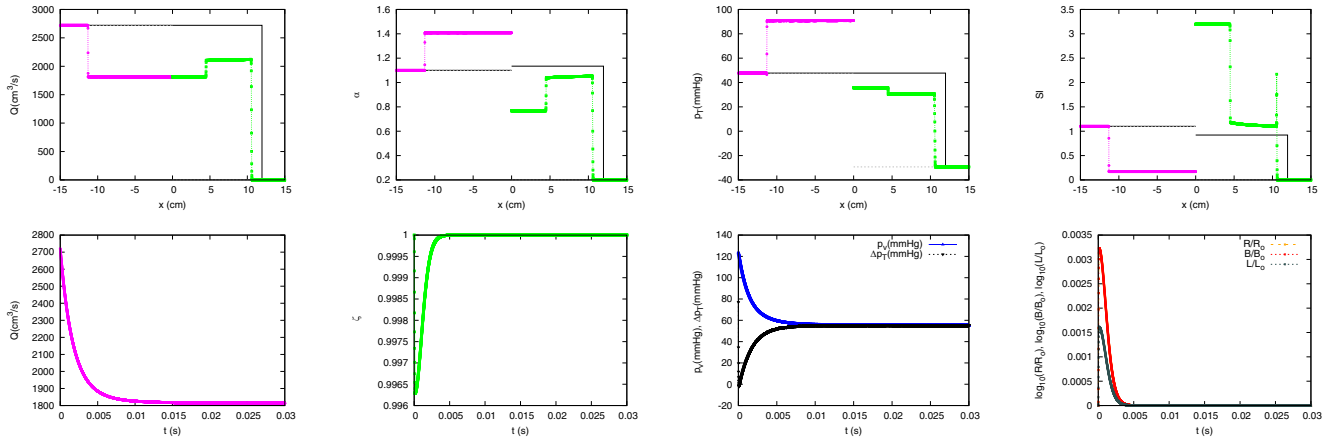

FIGURE 8 Section 2.3.2. Test VRP5. $\Delta x = 0.01$ cm. Initially open valve. Numerical solutions in space for vessels $k1$ and $k2$ located upstream and downstream the valve at $t = 0.030$ s (upper) and numerical solutions for the valve located at $x = 0$ in time (lower).

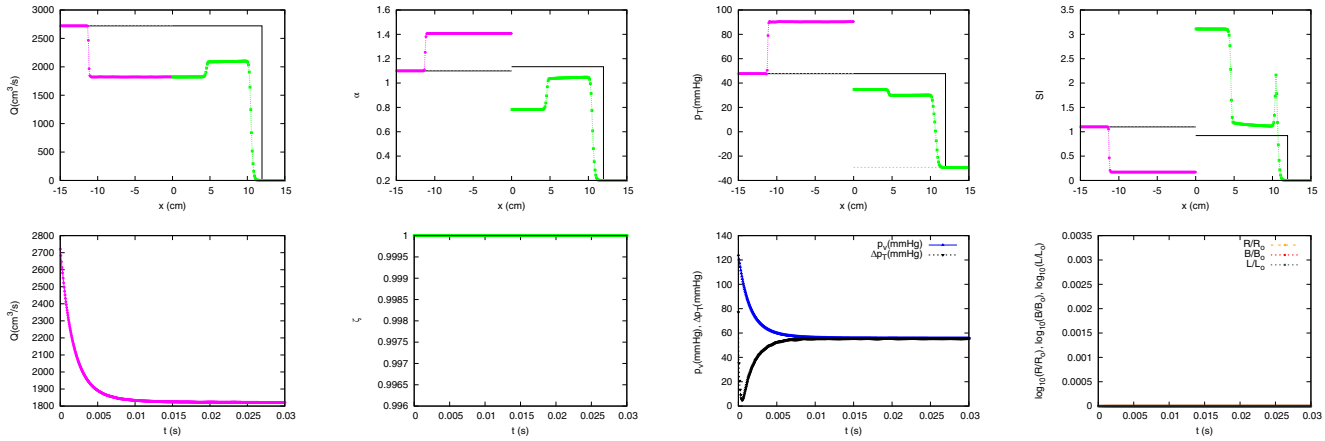

FIGURE 9 Section 2.3.2. Test VRP5. $\Delta x = 0.1$ cm. Initially open valve. Numerical solutions in space for vessels $k1$ and $k2$ located upstream and downstream the valve at $t = 0.030$ s (upper) and numerical solutions for the valve located at $x = 0$ in time (lower).

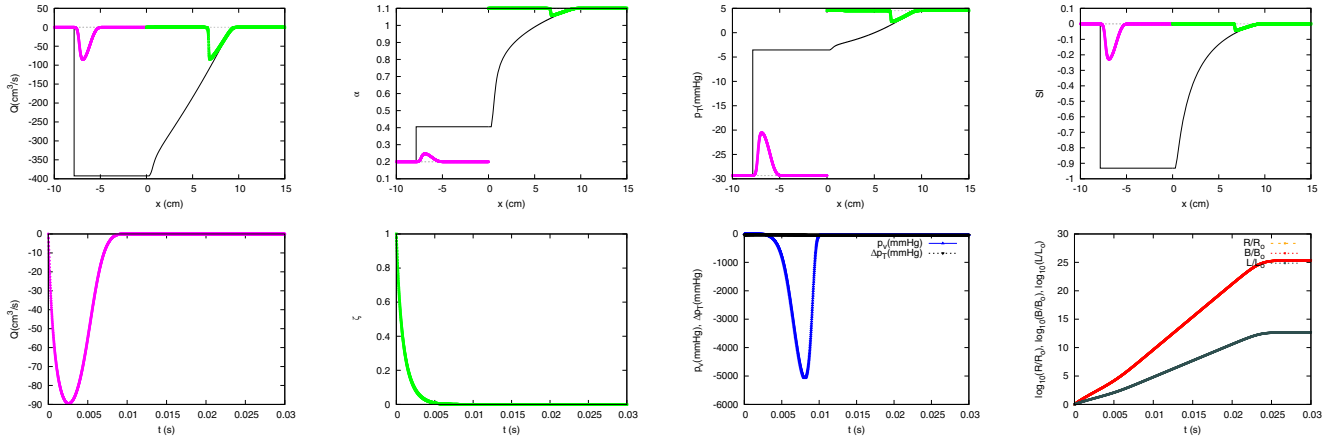

FIGURE 10 Section 2.3.2. Test VRP11. $\Delta x = 0.01$ cm. Initially open valve. Numerical solutions in space for vessels $k1$ and $k2$ located upstream and downstream the valve at $t = 0.030$ s (upper) and numerical solutions for the valve located at $x = 0$ in time (lower).

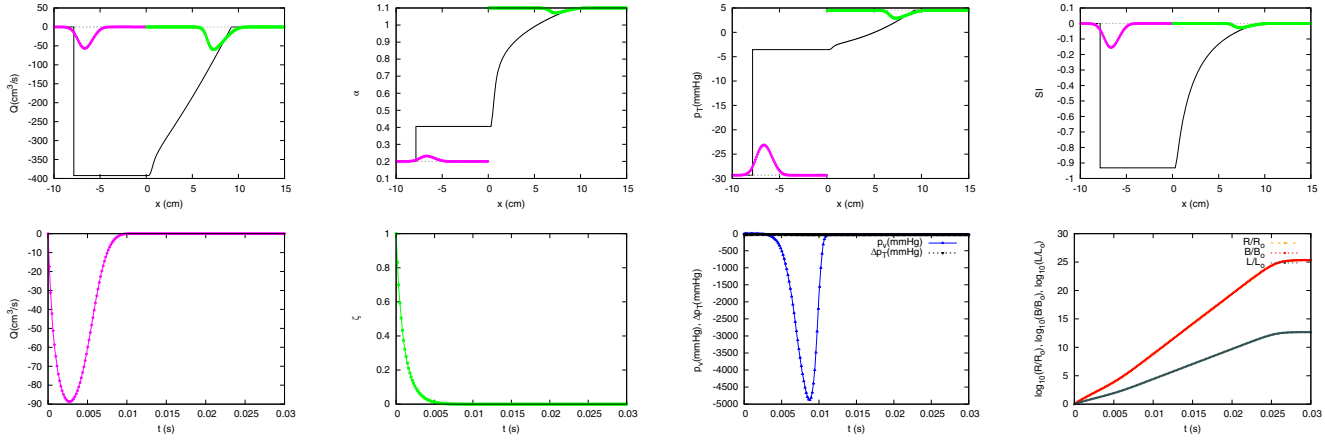

FIGURE 11 Section 2.3.2. Test VRP11. $\Delta x = 0.1$ cm. Initially open valve. Numerical solutions in space for vessels $k1$ and $k2$ located upstream and downstream the valve at $t = 0.030$ s (upper) and numerical solutions for the valve located at $x = 0$ in time (lower).

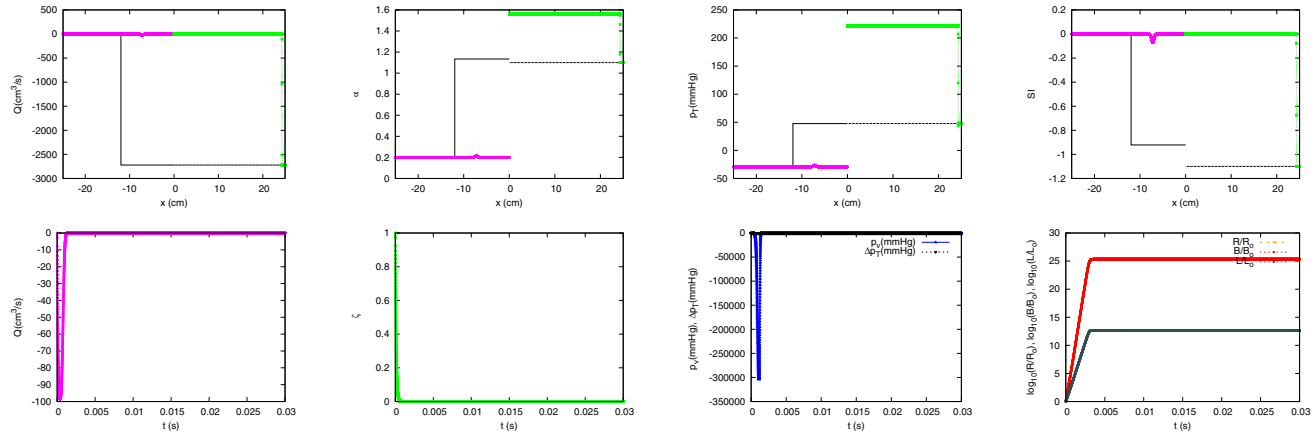

FIGURE 12 Section 2.3.2. Test VRP13. $\Delta x = 0.01$ cm. Initially open valve. Numerical solutions in space for vessels $k1$ and $k2$ located upstream and downstream the valve at $t = 0.030$ s (upper) and numerical solutions for the valve located at $x = 0$ in time (lower).

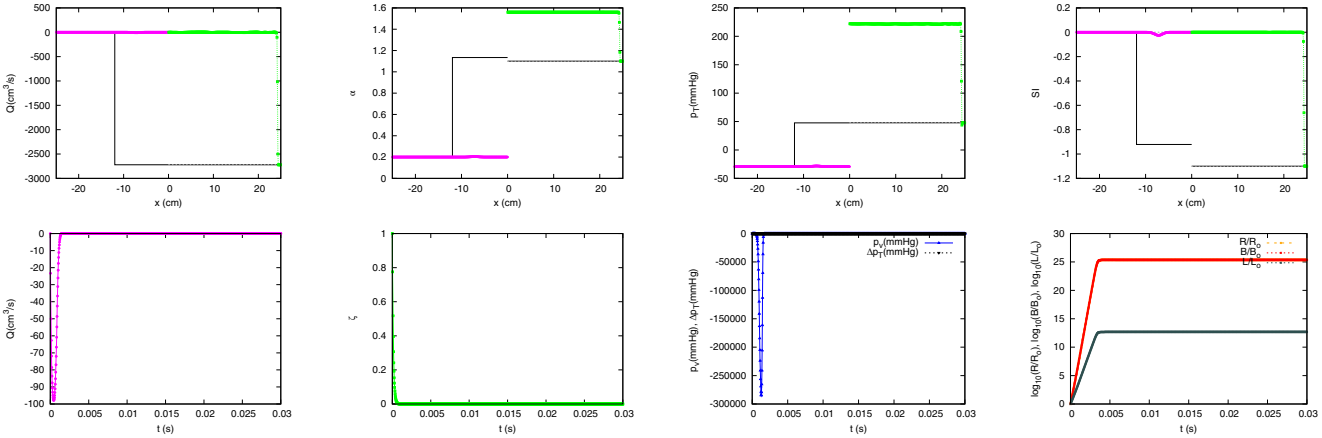

FIGURE 13 Section 2.3.2. Test VRP13. $\Delta x = 0.1$ cm. Initially open valve. Numerical solutions in space for vessels $k1$ and $k2$ located upstream and downstream the valve at $t = 0.030$ s (upper) and numerical solutions for the valve located at $x = 0$ in time (lower).

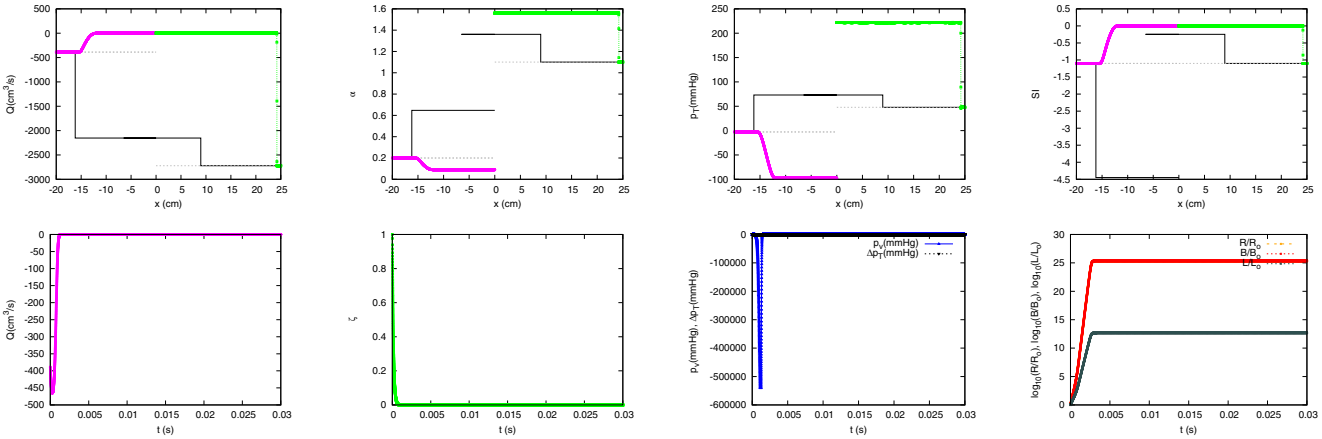

FIGURE 14 Section 2.3.2. Test VRP15. $\Delta x = 0.01$ cm. Initially open valve. Numerical solutions in space for vessels $k1$ and $k2$ located upstream and downstream the valve at $t = 0.030$ s (upper) and numerical solutions for the valve located at $x = 0$ in time (lower).

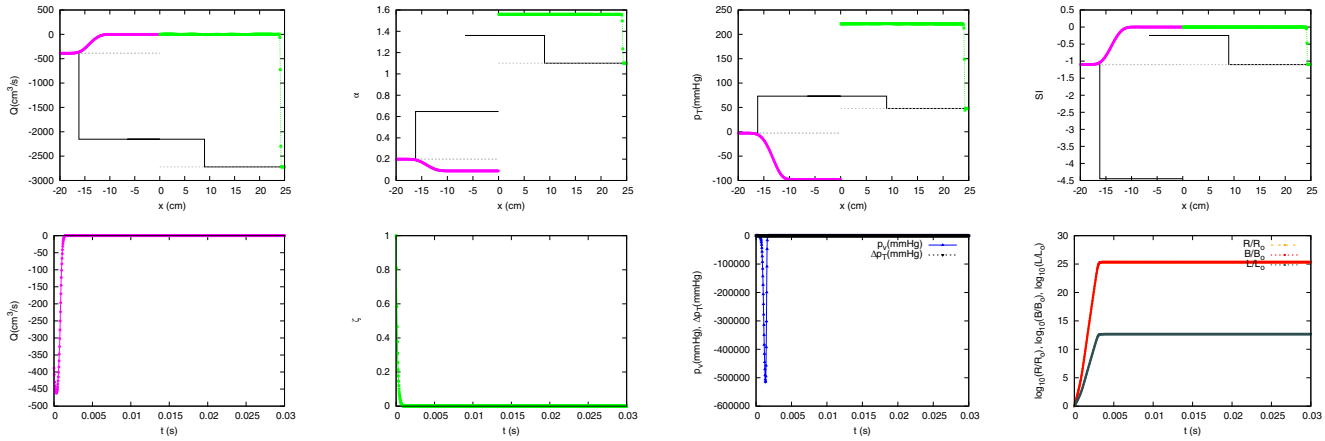

FIGURE 15 Section 2.3.2. Test VRP15. $\Delta x = 0.1$ cm. Initially open valve. Numerical solutions in space for vessels $k1$ and $k2$ located upstream and downstream the valve at $t = 0.030$ s (upper) and numerical solutions for the valve located at $x = 0$ in time (lower).

$$V = V_u + V_e = V_u + C_o(p_{tr} - p_o) = V_u + C_o\left(p - p_e^{\oplus} - p_o\right). \tag{90}$$

If we consider that in a vascular segment i variations in volume are provided by the difference between upstream vascular flow Q_{i-1} and the flow leaving the vascular segment i, mass conservation reads

$$\frac{d\,V_i}{dt} = Q_{i-1} - Q_i + \dot{I}_i = \frac{d\,V_e}{dt} + \frac{d\,V_u}{dt}, \tag{91}$$

where $\dot{I}$ is a source term accounting for an hemorrhage or an injection. Variation of transmural pressure in time is expressed as

$$C_{o,i}\frac{dp_{tr,i}}{dt} = Q_{i-1} - Q_i + \dot{I}_i - \frac{d\,V_u}{dt}, \tag{92}$$

leading to

$$\frac{dp_i}{dt} - \frac{dp_{e,i}^{\oplus}}{dt} = \frac{1}{C_{o,i}}\left(Q_{i-1} - Q_i + \dot{I}_i - \frac{d\,V_u}{dt}\right). \tag{93}$$

In this 0D model the momentum equation is reduced to

$$p_i - p_{i+1} = R_{o,i}Q_i + L_{o,i}\frac{dQ_i}{dt}, \tag{94}$$

that depends on the difference between the pressure in the vascular segment of interest p_i and the pressure in the downstream vascular segment p_{i+1}.

Numerical coupling of vessels with vascular beds can be done using different approaches: from a single compartment where only a feeding vessel is considered to multi-compartment combinations connecting feeding and collecting vessels. In Sections 2.4.1, 2.4.2, and 2.4.3, we will extend the solution of the JRP in (46) to three vascular models, with different level of complexity, providing new methodologies able to handle 1D-0D coupling models under any flow condition. In order to test the validity of the proposed techniques, the same numerical experiments will be conducted over vascular beds with equivalent properties.

2.4.1 | Four-element (RCLR) Windkessel/inertial model

The four-element (RCLR) Windkessel/inertial model,[34] defined by a single compartment, is shown in Figure 16, and is composed by a proximal resistance Z_0, a distal resistance R_1, an inertance L_1 and a capacitance C_1. Pressure p_{out} is the pressure at which flow to the microcirculation ceases. Volume, pressure and flow in the vascular bed V_1, p_1 and Q_1 respectively, have to be computed together with the unknown cross-sectional area $A^\star_{k1}$ and velocity $u^\star_{k1}$ in k_1 vessel. The solution of the JRP in (46) is adapted here to include the presence of the RCLR model.

In order to face any possible flow transition in the connecting vessel and to extend the methodology presented here to more complex 0D models, the solution is defined using two systems of equations. The unknowns are solved using Picard iterations between times t and $t+\Delta t$.

The first system is a non-linear system, involving relations for non-linear waves and the pressure drop between the boundary cell and the vascular bed, accounting for the Riemann problem at the interface between a 1D domain and then 0D outflow model, with

$$\mathbf{E}(\mathbf{X}) = \begin{bmatrix} (u^\star - u^n + g\mathcal{B})_{k1}\mathcal{D}_{w,k1} & + & du^\star_{k1}(1-\mathcal{D}_{w,k1}) \\ \left(g_{k1}\left(p^\star_{k1} - p_1^{n+1}\right) - Z_0 Q^\star_{k1}\right)\mathcal{Q}_{w,k1} & + & d\alpha^\star_{k1}(1-\mathcal{D}_{w,k1}) \end{bmatrix} = 0, \tag{95}$$

with $\mathbf{X} = \left[u^\star_{k1}, \alpha^\star_{k1}\right]$ and $g_{k1} = 1$, where the coupling condition has been numerically integrated here using an implicit discretization. Now, parameter $\mathcal{Q}_{w,k}$ is defined as

$$\mathcal{Q}_{w,k} = \mathcal{T}_{w,k}\mathcal{D}_{w,k}, \tag{96}$$

as there is only one eligible vessel. System of equations in (95) is indirectly solved using the equivalent linear system in (35) where the Jacobian matrix $\mathbf{J_E}$ is given by

$$\mathbf{J_E} = \begin{bmatrix} \mathcal{D}_{w,k1}(\mathcal{T}_{w,k1} - 1) + 1 & \mathcal{D}_{w,k1}\ a_{k1} \\ -R_{t,k1}\ b_{k1}\mathcal{Q}_{w,k1} + (1 - \mathcal{Q}_{w,k1}) & \left[\left(g\mathcal{D}_w K_o \frac{\partial\sigma}{\partial\alpha}\right)_{k1} - R_{t,k1}\ v_{k1}\right]\mathcal{Q}_{w,k1} + (1 - \mathcal{D}_{w,k1}) \end{bmatrix}. \tag{97}$$

The second system of equations, $\mathbf{H}(\mathbf{Y}) = 0$, is linear and provides the values for pressure and flow in the vascular segment using equations in (93) and (94) respectively

$$\mathbf{H}(\mathbf{Y}) = \begin{bmatrix} {p_1}^{n+1} - p_1^n - \dfrac{\Delta t}{C_1}\left(Q^\star_{k1} - {Q_1}^{n+1}\right) - \Delta p^{\circledast}_{e,1} - \dfrac{1}{C_1}\left(\dot{I}_1 \Delta t - \Delta V_{u,1}\right) \\ p_1^{n+1} - p_{out} - \left(\dfrac{L_1}{\Delta t} + R_1\right) Q_1^{n+1} + \left(\dfrac{L_1}{\Delta t}\right) Q_1^n \end{bmatrix}, \quad \mathbf{Y} = \begin{bmatrix} p_1^{n+1} \\ Q_1^{n+1} \end{bmatrix}, \tag{98}$$

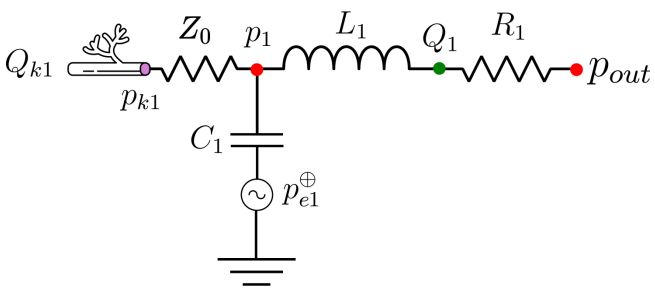

FIGURE 16 Lumped parameter element network RCLR.

where mass and momentum equation in (93) and (94) have been numerically integrated here using an implicit discretization. Once this system of linear equations is solved it is possible to update the volume stored in the compartment

$$V_1^{n+1} = V_1^n + \left(Q_{k1}^\star - {Q_1}^{n+1} + \dot{I}_1\right)\Delta t, \tag{99}$$

using the mass conservation equation.

2.4.2 | Serially arranged compartments

The vascular beds can be constructed by serially arranged compartments[42] including the arteriolar, capillary and venular compartments (from right to left), as shown in Figure 17. In each compartments pressure and flow (p_i, Q_i) are obtained by requiring mass and momentum conservation. The solution is provided by two systems of equations are solved using Picard iterations between times t and $t+\Delta t$. The first system in (95) provides the unknown cross-sectional area $A_{k1}^\star$ and velocity $u_{k1}^\star$ in k_1 vessel. The second system of equations, $\mathbf{H}(\mathbf{Y}) = 0$, provides the values for pressure and flow in the three vascular segments, with

$$\mathbf{H}(\mathbf{Y}) = \begin{bmatrix} {p_1}^{n+1} - \dfrac{\Delta t}{C_1}\left(Q_{k1}^\star - {Q_1}^{n+1}\right) - p_1^n - \Delta p_{e,1}^{\oplus} - \dfrac{1}{C_1}\left(\dot{I}_1\Delta t - \Delta V_{u,1}\right) \\ p_1^{n+1} - p_2^{n+1} - \left(\dfrac{L_1}{\Delta t} + R_1\right)Q_1^{n+1} + \left(\dfrac{L_1}{\Delta t}\right)Q_1^n \\ {p_2}^{n+1} - \dfrac{\Delta t}{C_2}\left(Q_1 - Q_2\right)^{n+1} - p_2^n - \Delta p_{e,2}^{\oplus} - \dfrac{1}{C_2}\left(\dot{I}_2\Delta t - \Delta V_{u,2}\right) \\ p_2^{n+1} - p_3^{n+1} - \left(\dfrac{L_2}{\Delta t} + R_2\right)Q_2^{n+1} + \left(\dfrac{L_2}{\Delta t}\right)Q_2^n \\ {p_3}^{n+1} - \dfrac{\Delta t}{C_3}\left(Q_2^{n+1} - Q_{k2}^\star\right) - p_3^n - \Delta p_{e,3}^{\oplus} - \dfrac{1}{C_3}\left(\dot{I}_3\Delta t - \Delta V_{u,3}\right) \\ p_3^{n+1} - p_{out} - \left(\dfrac{L_3}{\Delta t} + R_3\right)Q_3^{n+1} + \left(\dfrac{L_3}{\Delta t}\right)Q_3^n \end{bmatrix}, \quad \mathbf{Y} = \begin{bmatrix} p_1^{n+1} \\ Q_1^{n+1} \\ p_2^{n+1} \\ Q_2^{n+1} \\ p_3^{n+1} \\ Q_3^{n+1} \end{bmatrix}. \tag{100}$$

Once this system of linear equations is solved it is possible to update the volume in each compartment,

$$V_i^{n+1} = V_i^{n+1} + \left(Q_{i-1}^{n+1} - {Q_i}^{n+1} + \dot{I}_i\right)\Delta t, \quad i = 1,2,3. \tag{101}$$

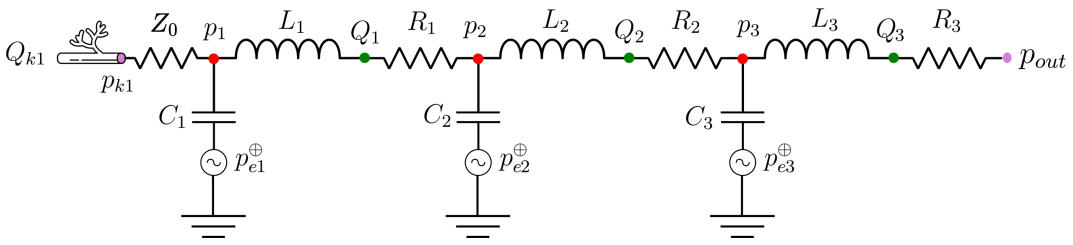

FIGURE 17 Vascular bed with serially arranged compartments. Lumped parameter element network.

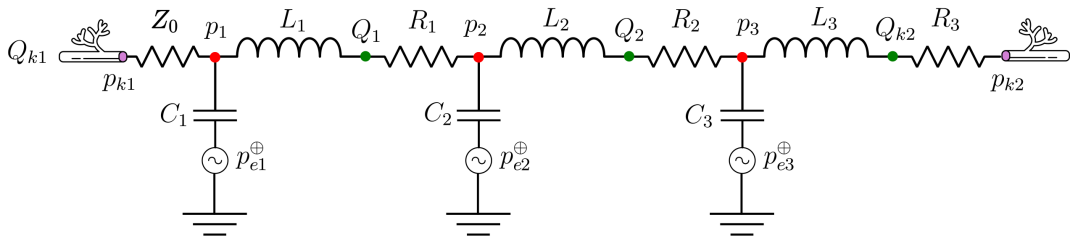

FIGURE 18 Vascular bed with serially arranged compartments and a collecting vessel. Lumped parameter element network.

2.4.3 | Serially arranged compartments with collecting vessels

Terminal vessel $k1$ can be linked to vessel $k2$ via a 0D lumped-parameter model that includes arterioles, capillaries and venules, as shown in Figure 4. Two systems of equations are provided to couple the solution (Figure 18). The first system is a non-linear system, involving relations for non-linear waves and the pressure drop between the boundary cells and the vascular bed, with

$$\mathbf{E}(\mathbf{X}) = \begin{bmatrix} (u^{\bullet} - u^n + g\mathcal{B})_{k1}\mathcal{D}_{w,k1} & + & du^{\star}_{k1}(1-\mathcal{D}_{w,k1}) \\ (u^{\bullet} - u^n + g\mathcal{B})_{k2}\mathcal{D}_{w,k2} & + & du^{\star}_{k2}(1-\mathcal{D}_{w,k2}) \\ \left(g_{k1}\left(p^{\star}_{k1} - p_1^{n+1}\right) - R_{t,k1}Q^{\star}_{k1} + L_{t,k1}Q^n_{k1}\right)\mathcal{Q}_{w,k1} & + & d\alpha^{\star}_{k1}(1-\mathcal{D}_{w,k1}) \\ \left(g_{k2}\left(p^{\star}_{k2} - p_3^{n+1}\right) - R_{t,k2}Q^{\star}_{k2} + L_{t,k2}Q^n_{k2}\right)\mathcal{Q}_{w,k2} & + & d\alpha^{\star}_{k2}(1-\mathcal{D}_{w,k2}) \end{bmatrix}, \tag{102}$$

with $\mathbf{X} = \left[u^{\star}_{k1}, u^{\star}_{k2}, \alpha^{\star}_{k1}, \alpha^{\star}_{k2}\right]$, $g_{k1} = 1$, $g_{k2} = -1$ and

$$R_{t,k1} = Z_0, \quad L_{t,k1} = 0, \quad R_{t,k2} = \frac{L_3}{\Delta t} + R_3, \quad L_{t,k2} = \frac{L_3}{\Delta t}. \tag{103}$$

System of equations in (102) is indirectly solved using an equivalent linear system where the Jacobian is given by

$$\mathbf{J_E} = \begin{bmatrix} \mathbf{J_{E,1}} & \mathbf{J_{E,2}} \\ \mathbf{J_{E,3}} & \mathbf{J_{E,4}} \end{bmatrix}_{4\times 4}, \tag{104}$$

where

$$\mathbf{J_{E,1}} = \mathbf{I}_{2\times 2}\begin{bmatrix} \mathcal{D}_{w,k1}(\mathcal{T}_{w,k1} - 1) + 1 & \\ & \mathcal{D}_{w,k2}(\mathcal{T}_{w,k2} - 1) + 1 \end{bmatrix}, \quad \mathbf{J_{E,2}} = \mathbf{I}_{2\times 2}\begin{bmatrix} \mathcal{D}_{w,k1}\ a_{k1} & \\ & \mathcal{D}_{w,k2}\ a_{k2} \end{bmatrix}. \tag{105}$$

Matrix $\mathbf{J_{E,3}}$ is split in $\mathbf{J_{E,3}} = \mathbf{J^a_{E,3}} + \mathbf{J^b_{E,3}}$, with

$$\mathbf{J}^a_{\mathbf{E},3} = \mathbf{I}_{2\times 2}\begin{bmatrix} -R_{t,k1}\ b_{k1}\mathcal{Q}_{w,k1} \\ \\ -R_{t,k2}\ b_{k2}\mathcal{Q}_{w,k2} \end{bmatrix}, \quad \mathbf{J}^b_{\mathbf{E},3} = \mathbf{I}_{2\times 2}\begin{bmatrix} (1-\mathcal{Q}_{w,k1}) \\ \\ (1-\mathcal{Q}_{w,k2}) \end{bmatrix}, \tag{106}$$

and matrix $\mathbf{J}_{\mathbf{F},\mathbf{4}}$ is split in $\mathbf{J}_{\mathbf{E},\mathbf{4}} = \mathbf{J}^a_{\mathbf{E},\mathbf{4}} + \mathbf{J}^b_{\mathbf{E},\mathbf{4}}$, defined as

$$\mathbf{J}^a_{\mathbf{E},\mathbf{4}} = \mathbf{I}_{2\times 2}\begin{bmatrix} \left[\left(g\mathcal{D}_w K_o \frac{\partial\sigma}{\partial\alpha}\right)_{k1} - R_{t,k1}\ v_{k1}\right]\mathcal{Q}_{w,k1} \\ \\ \left[\left(g\mathcal{D}_w K_o \frac{\partial\sigma}{\partial\alpha}\right)_{k2} - R_{t,k2}\ v_{k2}\right]\mathcal{Q}_{w,k2} \end{bmatrix}, \quad \mathbf{J}^b_{\mathbf{E},\mathbf{4}} = \mathbf{I}_{2\times 2}\begin{bmatrix} (1-\mathcal{D}_{w,k1}) \\ \\ (1-\mathcal{D}_{w,k2}) \end{bmatrix}. \tag{107}$$

The second system of equations, $\mathbf{H}(\mathbf{Y}) = 0$, is linear and provides the values for pressure and flow in the vascular segment using equations in (93) and (94) respectively

$$\mathbf{H}(\mathbf{Y}) = \begin{bmatrix} {p_1}^{n+1} - \frac{\Delta t}{C_1}\left(Q^\star_{k1} - {Q_1}^{n+1}\right) - p^n_1 - \Delta p^\oplus_{e,1} - \frac{1}{C_1}\left(\dot{I}_1\Delta t - \Delta V_{u,1}\right) \\ \\ p^{n+1}_1 - p^{n+1}_2 - \left(\frac{L_1}{\Delta t} + R_1\right)Q^{n+1}_1 + \left(\frac{L_1}{\Delta t}\right)Q^n_1 \\ \\ {p_2}^{n+1} - \frac{\Delta t}{C_2}\left(Q_1 - Q_2\right)^{n+1} - p^n_2 - \Delta p^\oplus_{e,2} - \frac{1}{C_2}\left(\dot{I}_2\Delta t - \Delta V_{u,2}\right) \\ \\ p^{n+1}_2 - p^{n+1}_3 - \left(\frac{L_2}{\Delta t} + R_2\right)Q^{n+1}_2 + \left(\frac{L_2}{\Delta t}\right)Q^n_2 \\ \\ {p_3}^{n+1} - \frac{\Delta t}{C_3}\left(Q^{n+1}_2 - Q^\star_{k2}\right) - p^n_3 - \Delta p^\oplus_{e,3} - \frac{1}{C_3}\left(\dot{I}_3\Delta t - \Delta V_{u,3}\right) \end{bmatrix}, \quad \mathbf{Y} = \begin{bmatrix} p^{n+1}_1 \\ \\ Q^{n+1}_1 \\ \\ p^{n+1}_2 \\ \\ Q^{n+1}_2 \\ \\ p^{n+1}_3 \end{bmatrix}. \tag{108}$$

2.4.4 | Numerical experiments in vascular beds

Although vascular bed models are usually defined to connect terminal arteries with veins, they can be used to accommodate incoming flow from veins when modeling a portal venous system. In the numerical experiments presented here, all vessels are considered veins, more subject to experience large deformations and therefore, helpful to define complex scenarios. In Sections 2.4.5–2.4.7 a collection of test cases is presented where mechanical and geometrical properties of the vessels are constant and given by: $m_\sigma = 10$ and $n_\sigma = -3/2$, reference diameter $d_{o,k} = 30.5$ mm, reference pulse wave velocity $c_{o,k} = 118.72$ cm s^{-1} and reference pressure $p_{o,k} = 80/5$ mmHg for entering/draining flow vessels.

2.4.5 | Numerical tests in RCLR vascular beds

In this first set of numerical problems in vascular beds, subsonic, sonic, and supersonic conditions appear in the terminal vessel $k1$ connecting with RCLR the vascular bed. The parameters in the RCLR vascular bed are $R_1 = R_o = 0.01$ mmHg/(ml/s), $C_1 = C_o = 10$ ml/mmHg, $L_1 = L_o = 0.01$ mmHg/(ml/s^2). In all cases external pressure in vascular models is $p^\oplus_e(t) = 0$. Reference pressure $p_{out} = 0$. The initial conditions for vessel $k1$ and the lumped model are given in Table 2. The prescribed external pressure in vessels is kept constant in time in all cases. Numerical results in Figures 19, 21, 23, 25 and 27 (upper) provide the solution at $t = 0.2$ s for the vessel area, flow, SI, total pressure and p_{ext} in the $k1$ terminal vessel as well as the pressure and flow in the RCLR vascular bed labeled as segment S_1.

TABLE 2 Numerical test in serially arranged compartments with collecting vessels.

Test case	g_{k1}	$p_{e,k1}$	SI_{k1}	α_{k1}	p_1	Q_1	p_2	Q_2	p_3	Q_3	g_{k2}	$p_{e,k2}$	SI_{k2}	α^n_{k2}
SegColl−1	1	0.00	0.90	1.20	80	0	40	0	10	0	−1	0	0	1.0
SegColl-2	1	30.00	0.90	1.20	80	0	40	0	10	0	−1	0	0	1.0
SegColl-3	1	60.00	0.90	1.20	80	0	40	0	10	0	−1	0	0	1.0
SegColl-4	1	60.00	1.10	1.20	80	0	40	0	10	0	−1	0	0	1.0
SegColl-5	1	60.00	1.10	1.20	180	0	40	0	10	0	−1	0	0	1.0

Note: Test case, father or daughter vessel g_k, external pressure $p_{e,k}$ (mmHg), initial speed index SI_k, initial relative area α_k and initial pressure (mmHg) and flow (ml/s).

Numerical results in Figures 19, 21, 23, 25 and 27 (upper) provide the solution at $t = 0.2$ s for the vessel area, flow, SI, total pressure and p_{ext} in the $k1$ terminal vessel. Pressure and flow in time in the single vascular compartments labeled as S_1 are displayed in Figures 20, 22, 24, 26 and 28 (upper) (Table 3).

2.4.6 | Numerical tests in serially arranged compartments

In this second set of numerical problems in vascular beds, a terminal vessel $k1$ connects with a vascular bed composed by serially arranged compartments. Following,[43] the parameters in the vascular bed are $R_1 = 2/3R_o$, $R_2 = 1/4R_o$, $R_3 = 1/12R_o$ mmHg/(ml/s), $C_1 = C_o$, $C_2 = 0.1C_o$ $C_2 = 3C_o$ ml/mmHg, $L_1 = 2/3L_o$, $L_2 = 1/4L_o$, $L_3 = 1/12L_o$ mmHg/(ml/s^2). Reference pressure $p_{out} = 0$. The initial conditions are given in Table 4 and for vessel $k1$ are equal to those prescribed in Section 2.4.5. Numerical results in Figures 19, 21, 23, 25 and 27 (middle) provide the solution at $t = 0.2$ s for the vessel area, flow, SI, total pressure and p_{ext} in the $k1$ terminal vessel. Pressure and flow in time, in the 3 vascular compartments labeled as segments S_1, S_2 and S_3 are displayed in Figures 20, 22, 24, 26 and 28 (middle).

2.4.7 | Numerical test in serially arranged compartments with collecting vessels

Test cases 3Seg-1 to 3Seg-5 are modified by replacing the pressure p_{out} by an infinitely long collecting vessel, k_2. Initial conditions for vessels $k1$ and $k2$ and the lumped model are given in Table 4. Numerical results in Figures 19, 21, 23, 25 and 27 (lower) provide the solution at $t = 0.2$ s for the vessel area, flow, SI, total pressure and p_{ext} in the terminal vessel $k1$ and in the collecting vessel k_2. Pressure and flow in time, in the 3 vascular compartments labeled as segments S_1, S_2 and S_3 are displayed in Figures 20, 22, 24, 26 and 28 (lower).

2.4.8 | Numerical results

In test case RCLR-1, initial vessel area and velocity, close to the sonic condition, in the terminal vessel k_1 enforces flow towards the vascular bed. The vascular bed generates a strong resistance and pressure p_1 and flow Q_1 in the vascular segment increase in time, as observed in Figure 20 (right). This resistance generates a BCW in the terminal vessel k_1, as observed in Figure 19 (upper) at $x \approx -16$ cm. When the vascular bed is replaced by the three serially arranged compartments with equivalent properties in test case 3Seg-1, the resulting BCW in the terminal vessel k_1 and pressure p_1 and flow Q_1 evolution in the first vascular segment of test case RCLR-1 are almost identically reproduced, as shown in Figure 20 (right) and (middle).

When a collecting vessel is defined in 3SegColl-1 differences become more noticeable as the presence of vessel $k2$ generates an extra resistance to flow advance due to its own impedance, that generates an opposition to passage of pressure waves. While for the upstream vessel $k1$ the registered waves have the same nature, now pressure and flow evolution in time vascular segment S_3 experiment a lower rate, as changes depend on the evolution of the FCW that appears in vessel k_2, as observed in Figure 20 (middle) and (right).

When the pressure difference between terminal vessel k_1 and the microcirculation is increased by pressurizing the terminal vessel up to 50 mmHg in test cases RCLR-2, 3Seg-2 and 3SegColl-2, the vascular segment $S1$ receives the

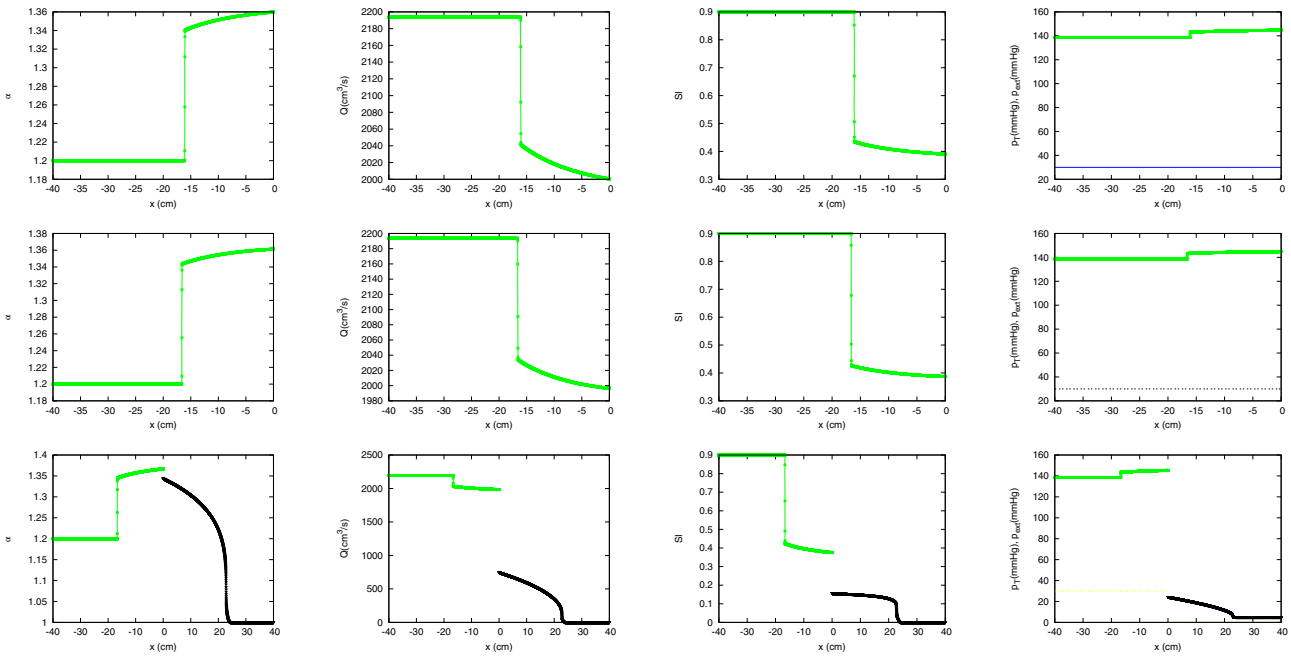

FIGURE 19 Section 2.4.4. Numerical solutions for the terminal vessels in test case RCLR-1 (upper), test case 3Seg-1 (middle) and test case 3SegColl-1 (lower), at $t = 0.2$ s.

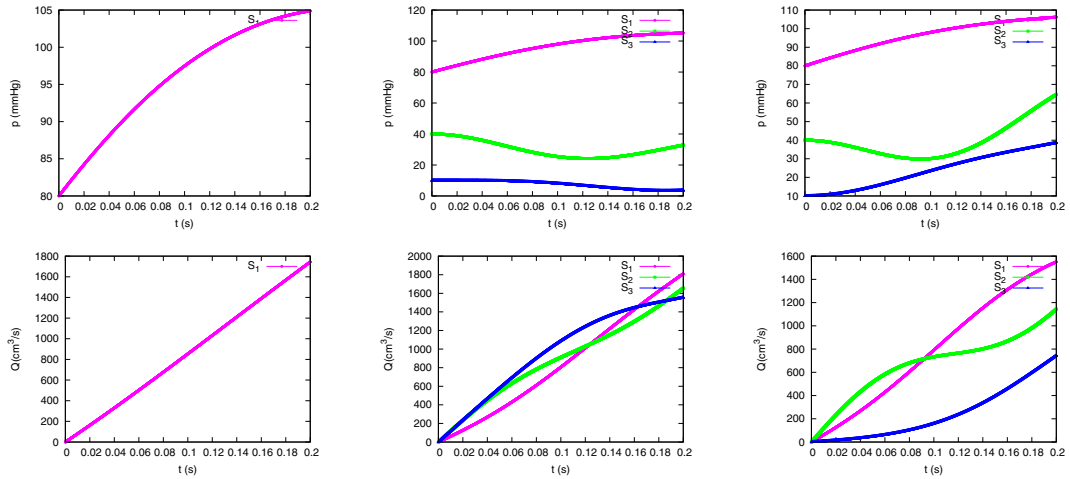

FIGURE 20 Section 2.4.4. Numerical solutions in time for pressure and flow in the vascular models in test case RCLR-1 (left), test case 3Seg-1 (middle) and test case 3SegColl-1 (right).

maximum amount of incoming flow that it is accelerated to sonic conditions, leading to BDW in vessel k_1, as shown in Figure 21 (upper), (middle) and (lower). The evolution in time for the pressure p_1 and flow Q_1 in the first vascular segment in the three cases is almost identical. The largest differences among models are provided by the presence of the collecting vessel, that provides an extra resistance to flow as seen in segment S_3 in Figure 22 (middle) and (right).

Figures 23 and 24 shows how further pressurization of vessel k_1 up to 60 mmHg in test case RCLR-3 do not change the solution in the vessel and in the vascular segment, as flow limitation has been already reached in test case RCLR-2.

When initial conditions in vessel k_1 are modified to lead to supersonic flow conditions in test cases RCLR-4, 3Seg-4, and 3SegColl-4, the flow cannot be further accelerated. Except in the vicinity of the coupling point, where a slow moving BDW appear, the vessel initial conditions remain constant in time, as observed in Figure 25. In this situation, the flow is transmitted to the vascular segment, and the flow decelerates to reach the subsonic condition, and the pressure drop between the vessel and the vascular segment is provided by the vessel impedance Z_0. The solution for the vascular

TABLE 3 Numerical tests in RCLR vascular beds.

Test case	g_{k1}	$p_{e,k1}$	SI_{k1}	α_{k1}	p_1	Q_1
RCLR−1	1	30.00	0.90	1.20	80	0
RCLR-2	1	50.00	0.90	1.20	80	0
RCLR-3	1	60.00	0.90	1.20	80	0
RCLR-4	1	60.00	1.10	1.20	80	0
RCLR-5	1	60.00	1.10	1.20	180	0

Note: Test case, father or daughter vessel g_k, external pressure $p_{e,k}$ (mmHg), initial speed index SI_k, initial relative area α_k and initial pressure (mmHg) and flow (ml/s).

TABLE 4 Serially arranged compartments.

Test case	g_{k1}	$p_{e,k1}$	SI_{k1}	α_{k1}	p_1	Q_1	p_2	Q_2	p_3	Q_3
Seg−1	1	30.00	0.90	1.20	80	0	40	0	10	0
Seg-2	1	50.00	0.90	1.20	80	0	40	0	10	0
Seg-3	1	60.00	0.90	1.20	80	0	40	0	10	0
Seg-4	1	60.00	1.10	1.20	80	0	40	0	10	0
Seg-5	1	60.00	1.10	1.20	180	0	40	0	10	0

Note: Test case, father or daughter vessel g_k, external pressure $p_{e,k}$ (mmHg), initial speed index SI_k, initial relative area α_k and initial pressure (mmHg) and flow (ml/s).

segment S_1 is almost equal for the three vascular models. Differences appear due to the resistance provided by the collecting vessel k_2, as shown in Figure 26.

In test cases RCLR-5, 3Seg-5, and 3SegColl-5, the initial condition for pressure in vascular segment S_1 in test cases RCLR-4, 3Seg-4, and 3SegColl-4, has been increased up to 180 mmHg, equal to the total pressure in the terminal vessel. The largest pressure drop between segments S_1 and p_{out} allow to increase the rate of the incoming flow to the vascular bed. In this case, and despite that initial supersonic conditions have been defined in k_1, the initial resistance to the flow generated by the vascular segment generates a BCW in vessel k_1, as shown in Figure 27. The solutions presents almost no remarkable differences among the three models. Pressure and flow variation when the vascular bed is represented by 1 or 3 segments is almost equal for vascular segment S_1, as shown in Figure 28 (left) and (middle). The resistance provided by collecting vessel k_2 has an impact in the evolution of vascular segments S_2 and S_3, as shown in Figure 28 (middle) and (right) leading to an increase in pressure and to a reduction of flow rate for S_3 when collecting vessel k_2 is present.

2.5 | Heart modeling

Heart is modeled using two ventricle-atrium (or half-heart) compartments or chambers, two valves and N vessels, as shown in Figure 5. The first chamber is connected with M vessels $(k1, kM)$ and the second valve with one vessel k_N. Pressure in each cardiac chamber is modeled using[42,44]

$$p_{ch,i} = p_{ext,ch,i} + e_{ch,i}(V_{ch} - V_{u,ch})_i + S_{ch,i}\frac{dV_{ch,i}}{dt}, \quad S_{ch,i} = K_{ch,i}p_{ch,i}, \quad i = 1,2, \tag{109}$$

where e_{ch} is the time-varying elastance, V_{ch} is the chamber volume, $V_{u,ch}$ refers to the dead volume, and S_{ch} is the viscoelasticity coefficient of the cardiac wall, which is related linearly to the cardiac pressure[44] by constant K_{ch}. Pressure in each cardiac chamber is evaluated using an implicit time discretization in time

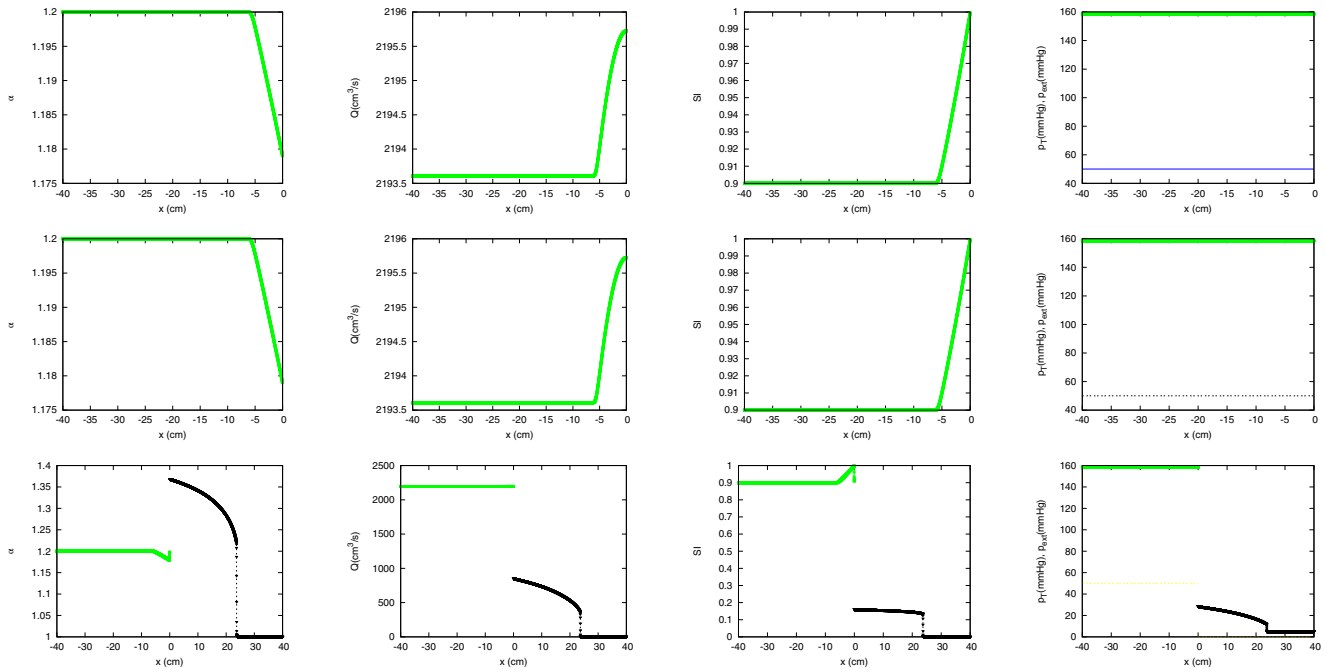

FIGURE 21 Section 2.4.4. Numerical solutions for the terminal vessels in test case RCLR-2 (upper), test case 3Seg-2 (middle) and test case 3SegColl-2 (lower), at $t = 0.2$ s.

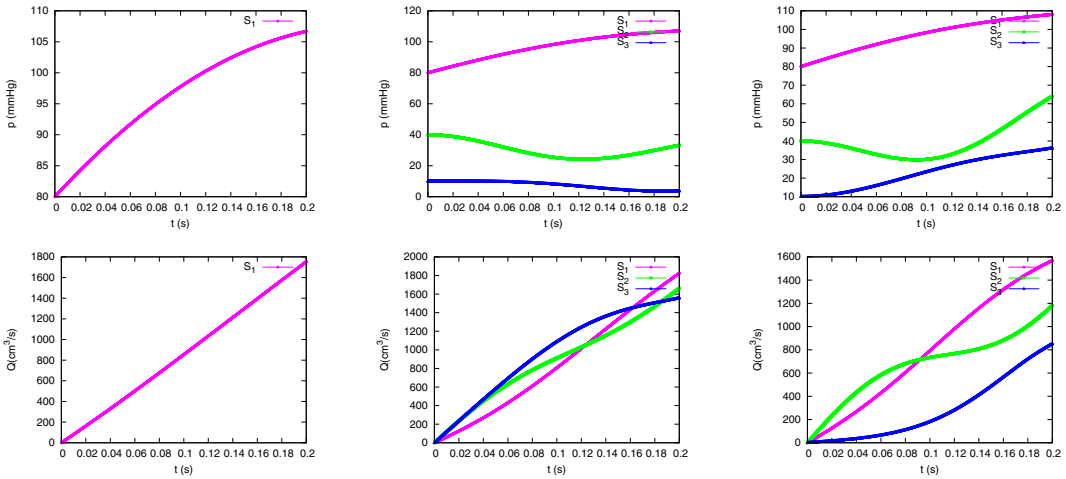

FIGURE 22 Section 2.4.4. Numerical solutions in time for pressure and flow in the vascular models in test case RCLR-2 (left), test case 3Seg-2 (middle) and test case 3SegColl-2 (right).

$$p_{ch}^{n+1} = \left[p_{ext,ch}^{n+1} + e_{ch}^{n}\left(V_{ch}^{n+1} - V_{u,ch}\right)\right]\left[1 - K_{ch}\frac{V_{ch}^{n+1} - V_{ch}^{n}}{\Delta t}\right]^{-1}. \tag{110}$$

Variations in chamber volume are given by;

$$\frac{dV_{ch,1}}{dt} = Q_{in} - Q_{v1}, \quad \frac{dV_{ch,2}}{dt} = Q_{v1} - Q_{v2}, \tag{111}$$

with Q_{in} the flow provided by the M terminal vessels,

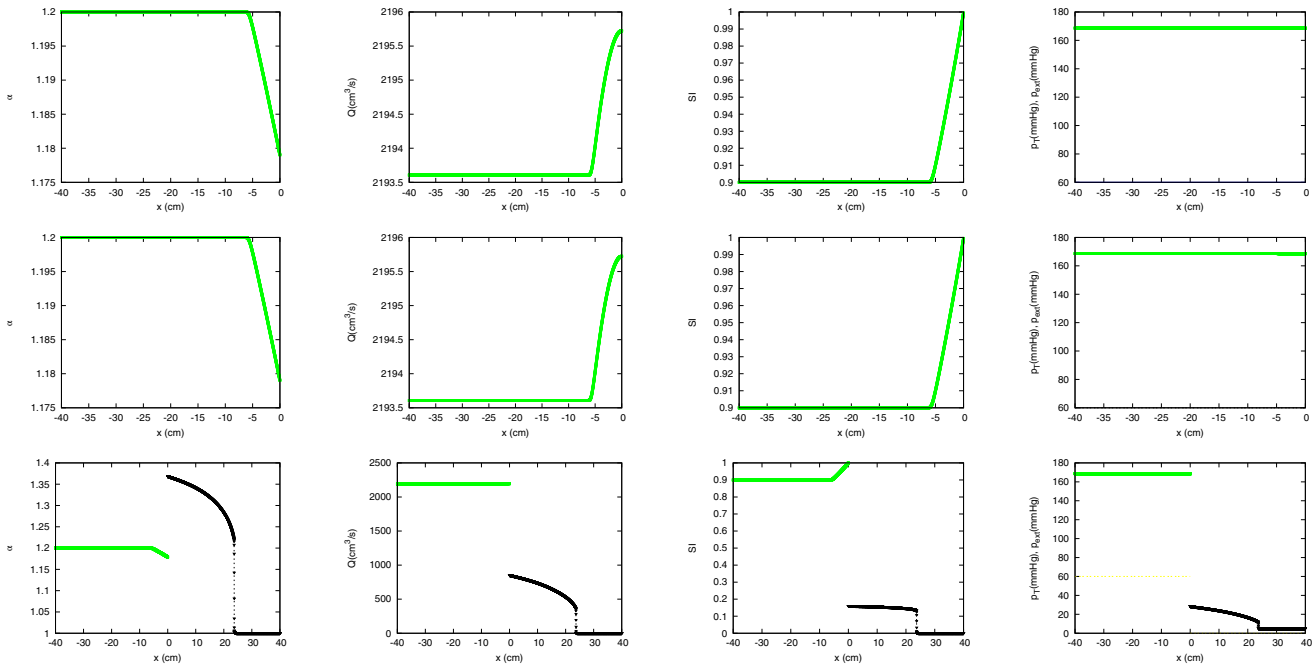

FIGURE 23 Section 2.4.4. Numerical solutions for the terminal vessels in test case RCLR-3 (upper), test case 3Seg-3 (middle) and test case 3SegColl-3 (lower), at $t = 0.2$ s.

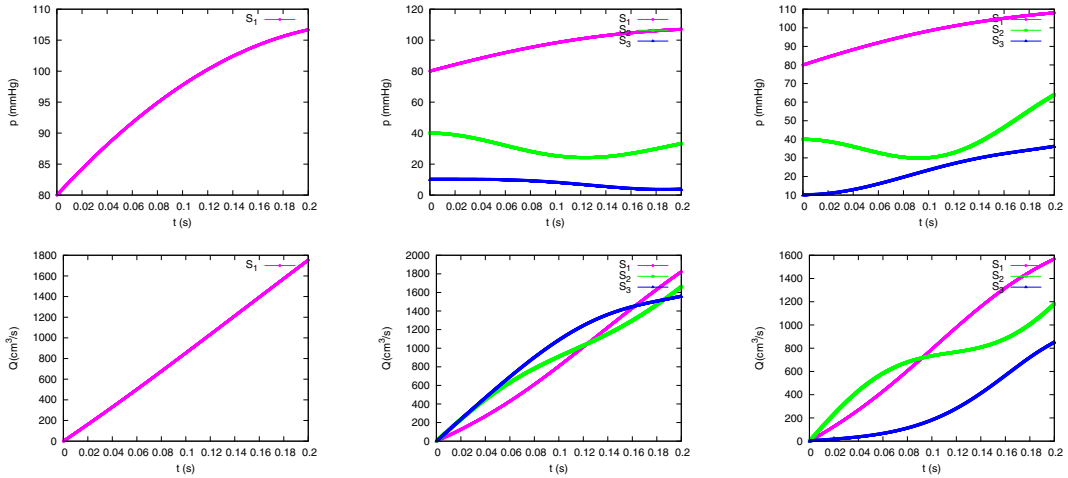

FIGURE 24 Section 2.4.4. Numerical solutions in time for pressure and flow in the vascular models in test case RCLR-3 (left), test case 3Seg-3 (middle) and test case 3SegColl-3 (right).

$$Q_{in} = \sum_{k=1}^{M} (u^{\star} \alpha^{\star} A_o \mathcal{D}_w)_k + \sum_{k=1}^{M} [(1 - \mathcal{D}_w)(Au)^n]_k, \tag{112}$$

and Q_{v1} and Q_{v2} the flow trough valves 1 and 2 respectively. The pressure drop across each valve is given by Equation (64) and now, linear resistance R_v, a quadratic resistance B_v and the inertance L_v, are defined as

$$R_v = R_{v,\zeta=1} \left(\frac{A_{e,\zeta=1}}{A_e} \right)^2, \quad B_v = B_{v,\zeta=1} \left(\frac{A_{e,\zeta=1}}{A_e} \right)^2, \quad L_v = L_{v,\zeta=1} \left(\frac{A_{e,\zeta=1}}{A_e} \right). \tag{113}$$

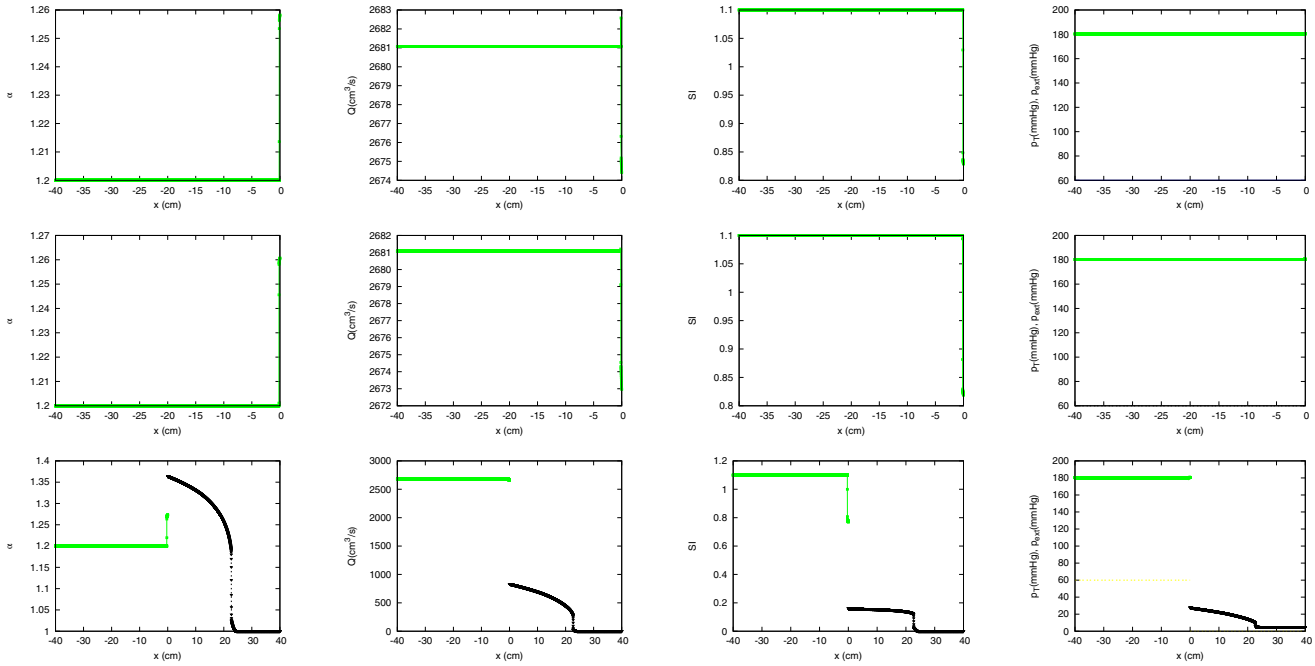

FIGURE 25 Section 2.4.4. Numerical solutions for the terminal vessels in test case RCLR-4 (upper), test case 3Seg-4 (middle) and test case 3SegColl-4 (lower), at $t = 0.2$ s.

The solution of the heart model is defined here by system $\mathbf{E}(\mathbf{X}) = 0$, where

$$\mathbf{E}(\mathbf{X}) = \begin{bmatrix} (u^{\star} - u^{n} + g\mathcal{B})_{k1}\mathcal{D}_{w,k1} & + & du^{\star}_{k1}(1-\mathcal{D}_{w,k1}) \\ \vdots & & \\ (u^{\star} - u^{n} + g\mathcal{B})_{kN}\mathcal{D}_{w,kN} & + & du^{\star}_{kN}(1-\mathcal{D}_{w,kN}) \\ \left(p^{\star}_{1} - p^{n+1}_{ch1}\right)\mathcal{Q}_{w,k1} & + & d\alpha^{\star}_{k1}(1-\mathcal{D}_{w,k1}) \\ \vdots & & \\ \left(p^{\star}_{M} - p^{n+1}_{ch1}\right)\mathcal{Q}_{w,kM} & + & d\alpha^{\star}_{kM}(1-\mathcal{D}_{w,kM}) \\ \left(p^{\star}_{N} - p^{n+1}_{ch2} + \Delta p^{n+1}_{v2}\right)\mathcal{Q}_{w,kN} & + & d\alpha^{\star}_{kN}(1-\mathcal{D}_{w,kN}) \\ p^{n+1}_{ch2} - p^{n+1}_{ch1} + \Delta p^{n+1}_{v1} & & \\ \Delta V_{ch,1} - \left(Q_{in} - Q^{\star}_{v1}\right)\Delta t & & \\ \Delta V_{ch,2} - \left(Q^{\star}_{v1} - Q^{\star}_{v2}\right)\Delta t & & \\ \left[(u^{\star}\alpha^{\star}A_o)_N - Q^{\star}_{v2}\right]\mathcal{D}_{w,N} & + & \left(Q^{n}_{N} - Q^{\star}_{v2}\right)(1-\mathcal{D}_{w,N}) \end{bmatrix}, \tag{114}$$

and

$$\mathbf{X} = \left[u^{\star}_{1} \ \ldots \ u^{\star}_{N} \ \alpha^{\star}_{1} \ \ldots \ \alpha^{\star}_{N} \ V_{ch1} \ V_{ch2} \ Q^{\star}_{v1} \ Q^{\star}_{v2} \ \right]^{T}, \tag{115}$$

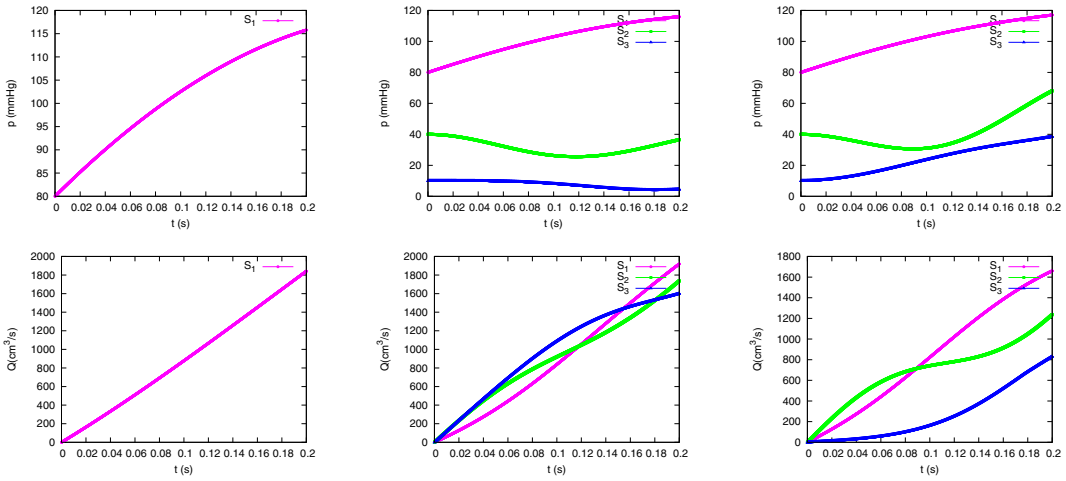

FIGURE 26 Section 2.4.4. Numerical solutions in time for pressure and flow in the vascular models in test case RCLR-4 (left), test case 3Seg-4 (middle) and test case 3SegColl-4 (right).

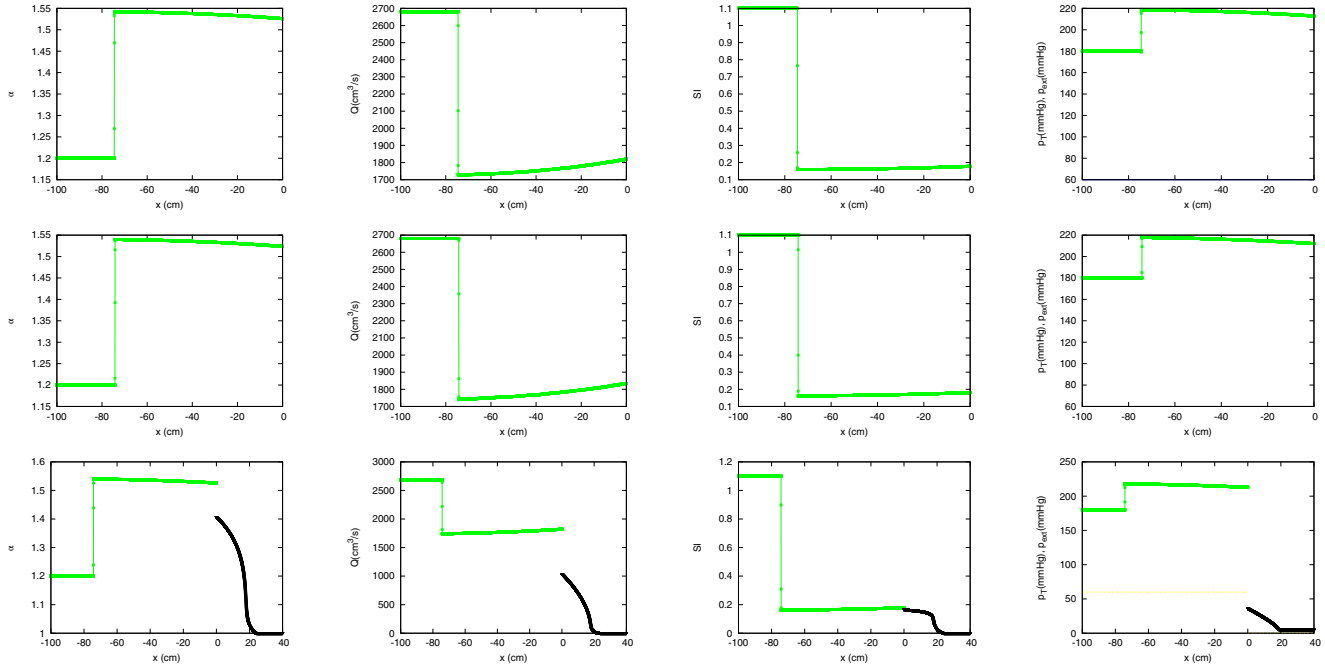

FIGURE 27 Section 2.4.4. Numerical solutions for the terminal vessels in test case RCLR-5 (upper), test case 3Seg-5 (middle) and test case 3SegColl-5 (lower), at $t = 0.2$ s.

where the first N equations are relations for non-linear waves and the next M equations involve conservation of chamber pressure p_{ch1} in the terminal vessels. Equations $2N$ and $2N+1$ define the pressure drop in valves 2 and 1. The following equations are the volume variations in chamber 1 and chamber 2. The last equation expresses the continuity of flow in valve 2 and vessel N. The parameter $\mathcal{Q}_{w,k} = \mathcal{T}_w \mathcal{D}_w$ avoids further acceleration of the flow in sonic and supersonic problems. System of equations in (114) is indirectly solved using the equivalent linear system in (35) where the Jacobian matrix $\mathbf{J_E}$ is given by

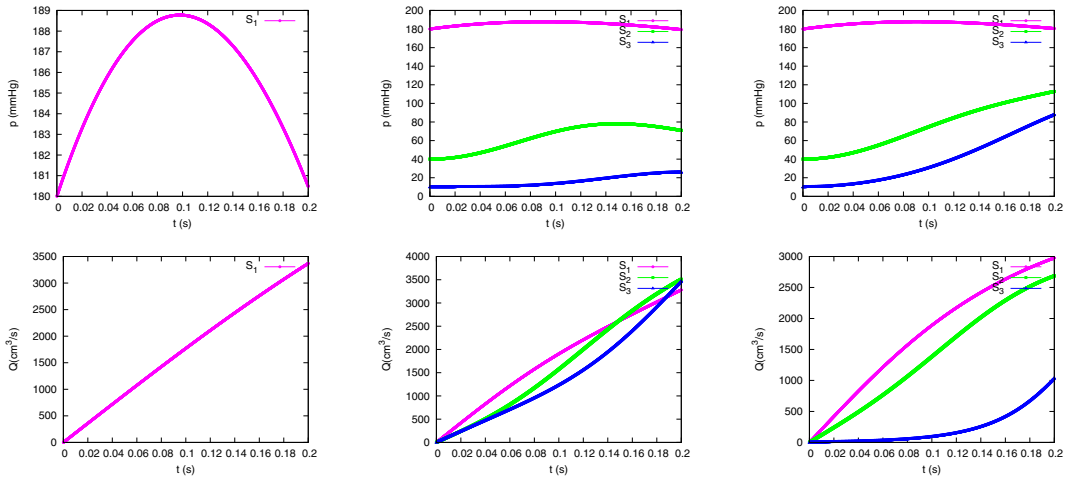

FIGURE 28 Section 2.4.4. Numerical solutions in time for pressure and flow in the vascular models in test case RCLR-5 (left), test case 3Seg-5 (middle) and test case 3SegColl-5 (right).

$$\mathbf{J_E} = \begin{bmatrix} \mathbf{J_{E,1}} & \mathbf{J_{E,2}} & \mathbf{J_{E,3}} \\ \mathbf{J_{E,4}} & \mathbf{J_{E,5}} & \mathbf{J_{E,6}} \\ \mathbf{J_{E,7}} & \mathbf{J_{E,8}} & \mathbf{J_{E,9}} \end{bmatrix}, \tag{116}$$

with

$$\mathbf{J_{E,1}} = \mathbf{I}_{N\times N} \begin{bmatrix} \mathcal{D}_{w,k1}(\mathcal{T}_{w,k1}-1)+1 \\ \vdots \\ \mathcal{D}_{w,kN}(\mathcal{T}_{w,kN}-1)+1 \end{bmatrix}, \quad \mathbf{J_{E,2}} = \mathbf{I}_{N\times N} \begin{bmatrix} \mathcal{D}_{w,k1}\ a_{k1} \\ \vdots \\ \mathcal{D}_{w,kN}\ a_{kN} \end{bmatrix}, \quad \mathbf{J_{E,3}} = \mathbf{0}_{N\times 4}, \tag{117}$$

$$\mathbf{J_{E,4}} = \mathbf{I}_{N\times N} \begin{bmatrix} (1-\mathcal{T}_{w,1})\mathcal{D}_{w,1} \\ \vdots \\ (1-\mathcal{T}_{w,M})\mathcal{D}_{w,M} \\ (1-\mathcal{T}_{w,N})\mathcal{D}_{w,N} \end{bmatrix}, \quad \mathbf{J_{E,5}} = \mathbf{I}_{N\times N} \begin{bmatrix} \left(\mathcal{Q}_w K_o \frac{\partial\sigma}{\partial\alpha}\right)_1 + (1-\mathcal{D}_{w,1}) \\ \vdots \\ \left(\mathcal{Q}_w K_o \frac{\partial\sigma}{\partial\alpha}\right)_M + (1-\mathcal{D}_{w,M}) \\ \left(\mathcal{Q}_w K_o \frac{\partial\sigma}{\partial\alpha}\right)_N + (1-\mathcal{D}_{w,N}) \end{bmatrix}, \tag{118}$$

$$\mathbf{J_{E,6}} = \begin{bmatrix} -d_{p_{ch},1}\mathcal{Q}_{w,1} & 0 & 0 & 0 \\ \vdots & \vdots & \vdots & \vdots \\ -d_{p_{ch},1}\mathcal{Q}_{w,M} & 0 & 0 & 0 \\ 0 & -d_{p_{ch},2}\mathcal{Q}_{w,N} & 0 & d_{v,2}\mathcal{Q}_{w,N} \end{bmatrix}_{N\times 4}, \tag{119}$$

where

$$d_{p_{ch}} = \left[e_{ch} + p_{ch}\frac{K_{ch}}{\Delta t}\right]\left[1 - K_{ch}\frac{\Delta V_{ch}}{\Delta t}\right]^{-1}, \tag{120}$$

and

$$\mathbf{J}_{\mathbf{E},7} = \begin{bmatrix} 0 & 0 & ... & 0 & 0 \\ -b_1\Delta t & -b_2\Delta t & ... & -b_M\Delta t & 0 \\ 0 & 0 & ... & 0 & 0 \\ 0 & 0 & ... & 0 & b_N \end{bmatrix}_{4\times N}, \quad \mathbf{J}_{\mathbf{E},8} = \begin{bmatrix} 0 & 0 & ... & 0 & 0 \\ -v_1\Delta t & -v_2\Delta t & ... & -v_M\Delta t & 0 \\ 0 & 0 & ... & 0 & 0 \\ 0 & 0 & ... & 0 & v_N \end{bmatrix}_{4\times N}, \tag{121}$$

$$\mathbf{J}_{\mathbf{E},9} = \begin{bmatrix} -d_{p_{ch,1}} & d_{p_{ch,2}} & d_{v,1} & 0 \\ 1 & 0 & \Delta t & 0 \\ 0 & 1 & -\Delta t & \Delta t \\ 0 & 0 & 0 & -1 \end{bmatrix}_{4\times N}. \tag{122}$$

After each Picard iteration the valve index ζ is updated with (83) or (85), where pressure drop in valves is computed as the difference in pressure as follows

$$\Delta p_{v1}^{\zeta} = p_{ch,2}^{m+1} - p_{ch,1}^{m+1}, \quad \Delta p_{v2}^{\zeta} = p_{ch,1}^{m+1} - p_N^{\star}. \tag{123}$$

With the new values of ζ^{m+1} the valve parameters in (113) are updated and finally pressure drop across the valve is computed using (64).

2.5.1 | Numerical test

In this section, five numerical experiments are performed over a half heart model with 3 upstream vessels and one downstream vessel. Mechanical and geometrical properties of the vessels are constant and given by: $m_\sigma = 10$ and $n_\sigma = -3/2$, reference diameter $d_{o,k} = 30.5$ mm, reference pulse wave velocity $c_{o,k} = 118.72$ cm s^{-1}. The reference pressure is $p_{o,k} = 20$ mmHg for the 3 terminal vessels and $p_{o,k} = 5$ mmHg for the collecting vessel. Initial conditions are defined in Figure 29 and are equal for the entering vessels. Conditions for pressure and external pressure in chamber 1 are also equal to those prescribed for the entering vessels and conditions for pressure and external pressure in chamber 2 are equal to the ones prescribed for the collecting vessel. In the two first numerical experiments, both valves are initially closed, and in the rest, both valves are initially open.

The chamber elastances are considered constant in time and equal to $e_{ch,1} = 0.09$ mmHg/ml and $e_{ch,2} = 0.08$ mmHg/ml. In the numerical tests proposed in this section the activation function of the heart has been neglected in order to define understandable scenarios while involving complex initial conditions.

Dead volumes are $V_{u,ch1} = 0$, $V_{u,ch2} = 100$ ml, and the viscoelasticity coefficient is $K_{ch} = 0.0005$ ml/s in both chambers. $M_{rg} = 0.0$, $M_{st} = 1.0$ and $dp_{vo} = 0.0$ in all cases. The rest of parameters for valve 1 are $R_{v,\zeta=1} = 0.001$ mmHg s ml^{-1}, $B_{v,\zeta=1} = 0.000016$ mmHg s^2 ml^{-2}, $L_{v,\zeta=1} = 0.0002$ mmHg s^2 ml^{-1}, $R_{v,\zeta=1} = 0.003$ mmHg s ml^{-1}, $k_{vo,1} = 0.002$ (cm s/g), $k_{vc,1} = 0.004$ (cm s/g), and the rest of parameters for valve 2 are $B_{v,\zeta=1} = 0.000025$ mmHg s^2 ml^{-2}, $L_{v,\zeta=1} = 0.0005$ mmHg s^2 ml^{-1}, $k_{vo,2} = 0.003$ (cm s/g), $k_{vc,2} = 0.004$ (cm s/g). This set of parameters is based on.[37,42] In order to assess the robustness of the numerical methods presented in limiting scenarios, in the numerical test performed here, subsonic, sonic, and supersonic conditions, including initial conditions of reversal flow are enforced.

Figure 30 displays the numerical solutions for the feeding vessels and the leaving vessel at time 0.03 s (upper), and the numerical solutions for the variables of the heart model in time in test case HR1. In this case both valves are initially closed, but initial conditions for vessel area and velocity generate a flow across both valves, much larger in valve 1 than in valve 2, as shown in Figure 30. As valves are initially closed, they generate a large resistance to flow and a BCW appears in the terminal vessels. The fast opening of the valves reduces the flow resistance and flow across valve 1, Q_{v1}, increases dramatically, and overcomes the value of the total flow delivered by the terminal vessels Q_{in} at $t \approx 0.015$ s. At this time, the variation of volume in chamber 1, $V_{ch,1}$ in time is negative, an pressure in chamber 1, p_{ch1},

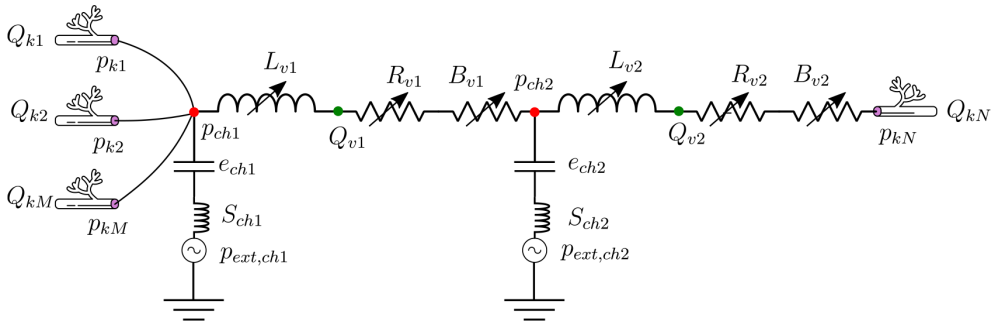

FIGURE 29 Lumped parameter for the heart.

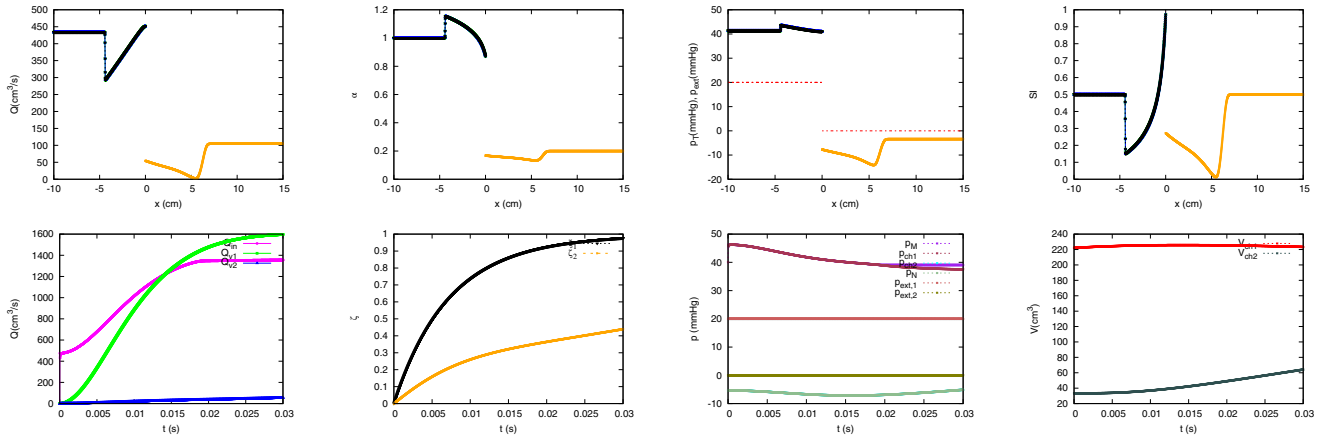

FIGURE 30 Section 2.5.1. Test case HR1. Initially closed valves. Numerical solutions for the feeding vessels and the leaving vessel at time 0.03 s (upper), and numerical solutions for the variables of the heart model in time (lower).

decreases, allowing an acceleration of the flow in the upstream vessels. Figure 30 shows how the upstream vessels reach sonic conditions at $t \approx 0.02$ s. For $t < 0.02$ s, the pressure in the outflow boundary section of the upstream vessels, p_M, is equal to the pressure in chamber 1, p_{ch1}. When flow in the upstream vessels becomes sonic, p_{ch1} becomes smaller than p_M, as flow limitation has already started and further flow cannot be delivered to chamber 1 from the upstream vessels. The total flow entering to the chamber, Q_{in} in Figure 30, becomes constant and a sonic BDW clearly appears in the upstream vessels. Regarding the collecting vessel kN, the ejection of flow across valve 2, Q_{v2}, is not high enough to counteract the inertia of the flow in kN, and a FDW appears. While pressure in chambers 1 and 2 are clearly different, the small pressure drop across valve 2 leads to almost indistinguishable results for the pressure in the leaving vessel, p_N and the pressure in chamber 2, p_{ch2}.

In test case HR2 the flow in the upstream vessel is increased by imposing initial supersonic conditions, leading to a larger amount of circulating flow, as shown in Figure 30. The valves, initially closed, generate a large resistance to flow and a BCW appears in the terminal vessels, as shown in Figure 31, but in this case the total flow entering to the chamber, Q_{in}, is larger than the one leaving the chamber across valve 1, Q_{v1}. An increase of volume in both chambers can be observed. In this case flow limitation does not appears, and along the simulation $p_M = p_{ch1}$.

In absence of valves, in test case HR3, the initial conditions for vessel deformation would induce reversal flow from the downstream vessel to the upstream vessels. In this test case both valves are initially open. As shown in Figure 32, at $t = 0$, $p_{ch2} > p_{ch1}$, and reversal flow is produced in valve 1 leading to its closure. At the same time, the extra volume added from chamber 2 to chamber 1 is transmitted to the upstream vessels, leading to small perturbation traveling in the backward direction. The flow inertia in the collecting vessel generates a suction in chamber 2 and a FDW in the same vessel. Once valve 1 is almost closed, flow can only be extracted from chamber 2. The FDW leads to a dramatic reduction of vessel area in vessel kN together with the increase in flow through valve 2, Q_{v2}, that remains fully open. The tail of the FDW is limited by a sonic point, and therefore flow limitation appears in the second valve governing the

coupling point between the collecting vessel and chamber 2. Another second peak in the *SI* appears, this time leading to supersonic flow conditions. It is generated in the tail of the FDW and can be explained by examining the shape of the PWV.[33] In veins, the dimensionless PWV $c/c(\alpha=1)$ is not a monotonically increasing function as in arteries, is a convex function with a minimum value at $\alpha_{min}=(n/m)^{2/(m-n)}\approx 0.72$. As in this test case the flow velocity increases between the tail and the head of the FDW, and in the same region the celerity c has a minimum, supersonic conditions are likely to be achieved.

In test case HR4, the initial condition for velocity in the upstream vessel in test case HR3 is modified by imposing a flow towards the heart in the upstream vessel. At time $t=0.03$ s, reversal flow conditions are avoided by the closure of both valves, as show in Figure 33. Both valves close almost at the same rate, and some fluid migrates from the collecting vessel to chamber 2, from chamber 2 to chamber 1, and from chamber 1 to the terminal vessels. The closure of valve 1 leads to backward traveling perturbation in the downstream vessels, while the closure of valve 2 leads to FCW in the upstream vessels. Figure 34 shows how when in test case HR5 the velocity in the upstream vessel is increased and supersonic flow conditions are imposed, valve 2 closes much faster that valve 1, and the speed of the resulting FCW is higher than the observed in test case HR4 (Table 5).

2.6 | Ethics statement

No experimentation occurred on human or animal subjects for this work.

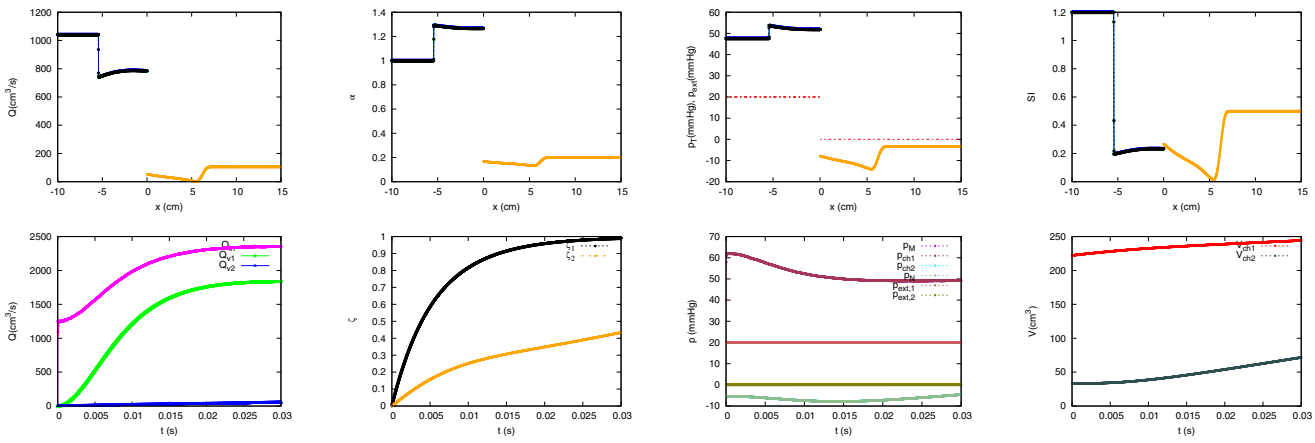

FIGURE 31 Section 2.5.1. Test case HR2. Initially closed valves. Numerical solutions for the feeding vessels and the leaving vessel at time 0.03 s (upper), and numerical solutions for the variables of the heart model in time (lower).

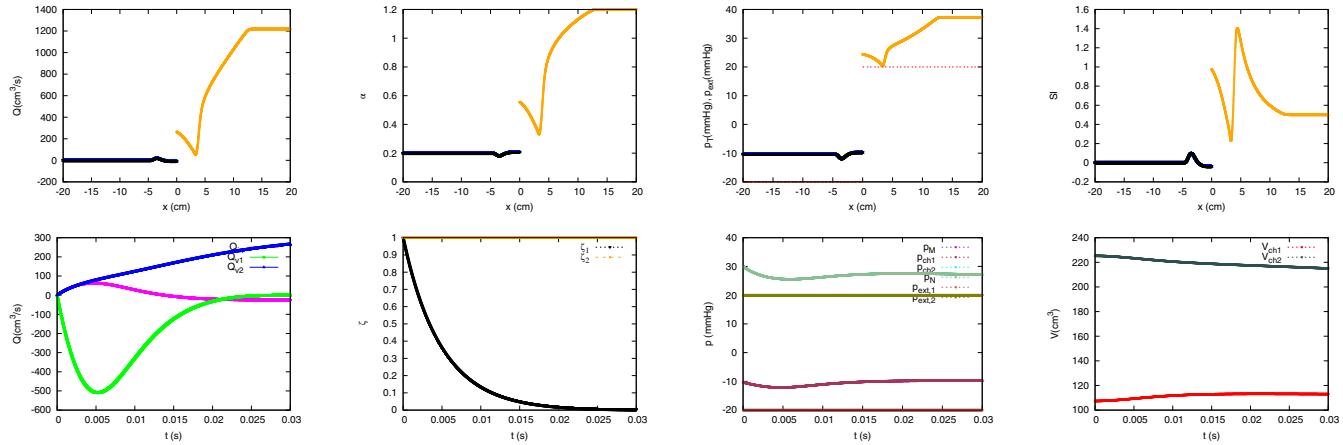

FIGURE 32 Section 2.5.1. Test case HR3. Initially open valves. Numerical solutions for the feeding vessels and the leaving vessel at time 0.03 s (upper), and numerical solutions for the variables of the heart model in time (lower).

3 | NUMERICAL SIMULATION OF A SUDDEN HEAD-UP TILT IN A GLOBAL MULTISCALE MATHEMATICAL MODEL

The effect of gravity over the flow regime conditions during a sudden induced postural changed in a closed loop model during a graded HUT from 0° (supine) to 90° (upright) is analyzed here. The closed loop model used here is composed by a comprehensive 1D model representing anatomically realistic systemic arterial/venous networks (including cerebral circulation) and pulmonary arterial/venous networks. Lumped parameter 0D models are used to represent cardiac function for the left and right heart and Windkessel-like 0D models are used to represent microvascular beds. This numerical experiment will allow to observe the coupling among the different models and numerical techniques described in this paper. The reflex control of the CVS or the autoregulatory mechanism has not been included, as we will focus in robustness of the numerical strategies proposed here and their effects when simulating a closed loop model.

Figure 35 shows the schematic representation of the 1D systemic arterial tree,[6,7] involving 88 vessels. The schematic representation of the 1D systemic venous tree is plotted in Figures 36 and 37, involving 188 vessels.[6,7] The distribution of 17 venous valves[37] is shown in Figure 35. Figure 38 shows the 1D vascular networks for the arterial and venous pulmonary vessels, including 57 arteries and 54 veins.[8] The complete vessel network is given the Appendix A in Table A1. The heart is considered as the reference elevation point with $\eta = 0$. Table A provides proximal and distal values of η for each vessel. Elevation η varies linearly inside each vessel. In the vascular segments, η is defined as the arithmetic mean provided by the values of η at the terminal computational cells in arteries and veins involved in each vascular bed.

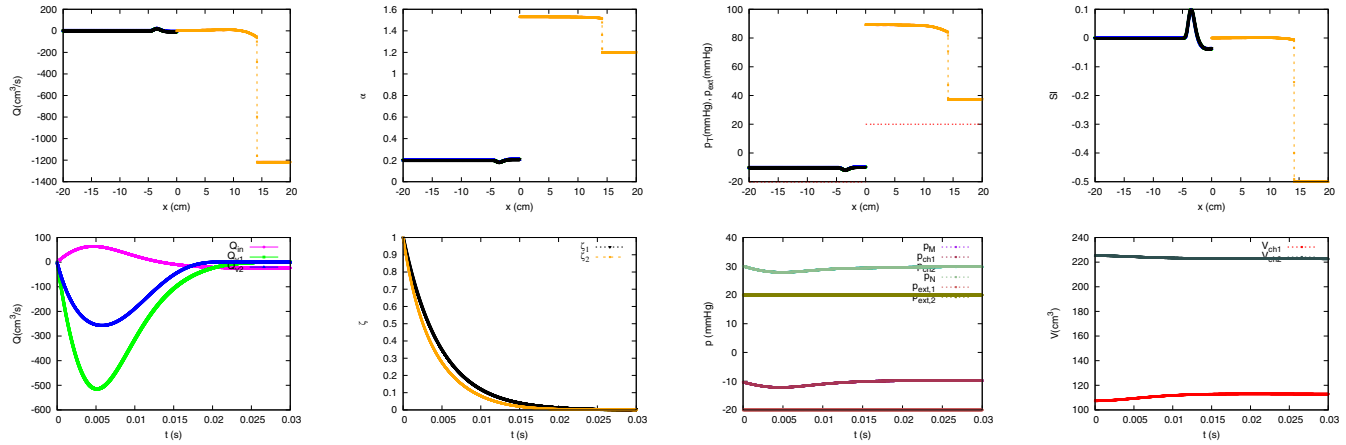

FIGURE 33 Section 2.5.1. Test case HR4. Initially open valves. Numerical solutions for the feeding vessels and the leaving vessel at time 0.03 s (upper), and numerical solutions for the variables of the heart model in time (lower).

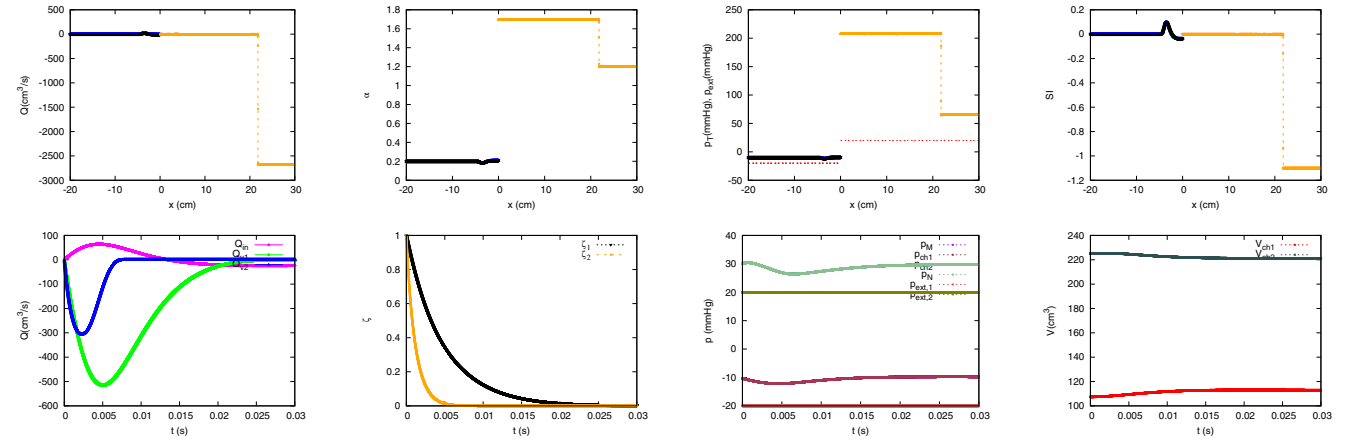

FIGURE 34 Section 2.5.1. Test case HR5. Initially open valves. Numerical solutions for the feeding vessels and the leaving vessel at time 0.03 s (upper), and numerical solutions for the variables of the heart model in time (lower).

TABLE 5 Heart model.

Test case	k	g_k	$p_{e,k}$	SI	α
HR1	1	1	20.00	0.50	1.00
	2	1	20.00	0.50	1.00
	3	1	20.00	0.50	1.00
	4	−1	0.00	0.50	0.20
HR2	1	1	20.00	1.20	1.00
	2	1	20.00	1.20	1.00
	3	1	20.00	1.20	1.00
	4	−1	0.00	0.50	0.20
HR3	1	1	−20.00	0.0	0.20
	2	1	−20.00	0.0	0.20
	3	1	−20.00	0.0	0.20
	4	−1	20.00	0.50	1.20
HR4	1	1	−20.00	0.0	0.20
	2	1	−20.00	0.0	0.20
	3	1	−20.00	0.0	0.20
	4	−1	20.00	−0.50	1.20
HR5	1	1	−20.00	0.0	0.20
	2	1	−20.00	0.0	0.20
	3	1	−20.00	0.0	0.20
	4	−1	20.00	−1.10	1.20

Note: Test case, upstream or downstream vessel g_k, external pressure $p_{e,k}$ (mmHg), initial speed index SI_k and initial relative area α_k in the vessels of the lumped heart model.

Model parameters used to represent the systemic circulation follow those used in.[37] Model parameters used to represent the pulmonary circulation follow those used in.[8] Model parameters for the cardiac function, heart chambers parameters and cardiac valves parameters follow the ones used in.[10] Venous valves parameters are defined as in.[37] Vascular models have been modeled using the artery–veins connections described in.[7,37] The total resistance of the systemic/pulmonary circulation was 0.85/0.136 mmHg/(ml s^{-1}) and the compliance was estimated assuming a time constant of the exponential fall-off of pressure during diastole given by $\tau = R_T C_T = 1.79/0.5$, according to[45] and[46] respectively. The procedure for the determination of Windkessel parameters presented in Reference 35 is used to calibrate the resistance and compliance of the serially arranged compartments used to define the vascular beds. Compliance and resistance inside each vascular bed are distributed following.[43] Peripheral inertances in vascular beds are not considered here, as they can be neglected in normal conditions.[34] Vessel are spatially discretized using a cell size $\Delta x = 0.1$ cm and the time step evolves using a Courant–Friedrichs–Lewy (CFL) condition equal to 0.5. The reference wave velocity used to compute the time step is provided by the initial solution stored in each cell and depends on the evolved solution in the internal boundary conditions. The time step is uniform for all vessel cells and all internal boundary conditions. The time step is selected as the most restrictive time step, $\Delta t = \min\{\Delta t_c, \Delta t_w\}$, comparing the most restrictive time step provided by all i computational cells of all vessels, Δt_c

$$\Delta t_c = CFL\ \Delta t_{min,c}, \quad \Delta t_{min,c} = \frac{\Delta x}{\max\{|u_i|^n + c_i^n\}}, \tag{124}$$

and the most restrictive time step provided by all the boundary walls at the internal boundary conditions Δt_w

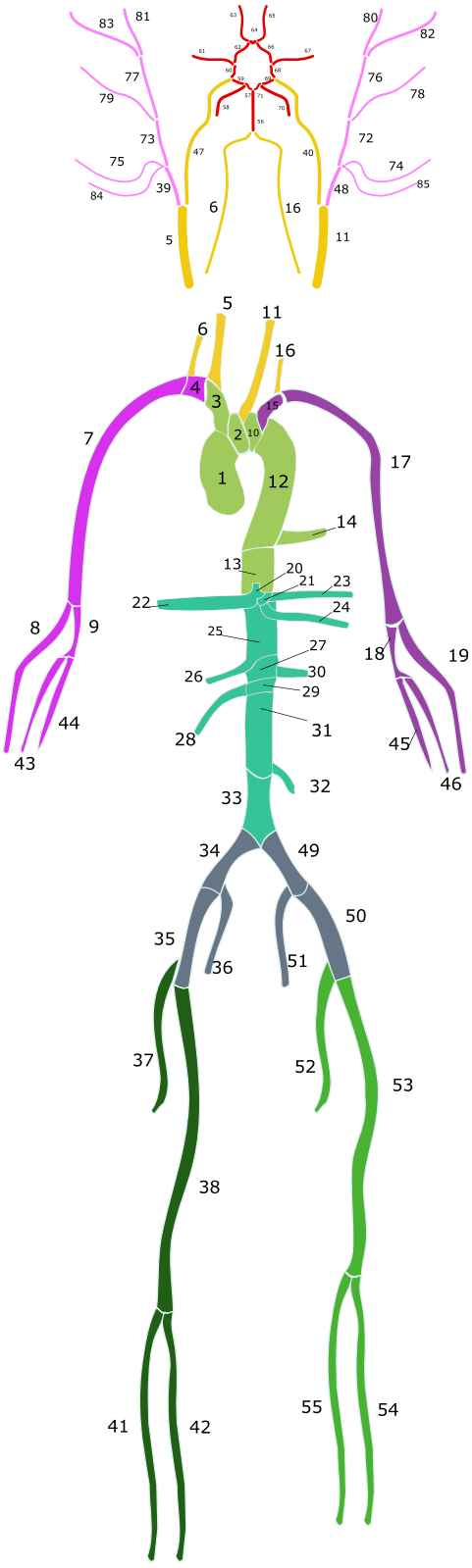

FIGURE 35 Section 3. Schematic representation of the 1D systemic arterial tree.[6,7]

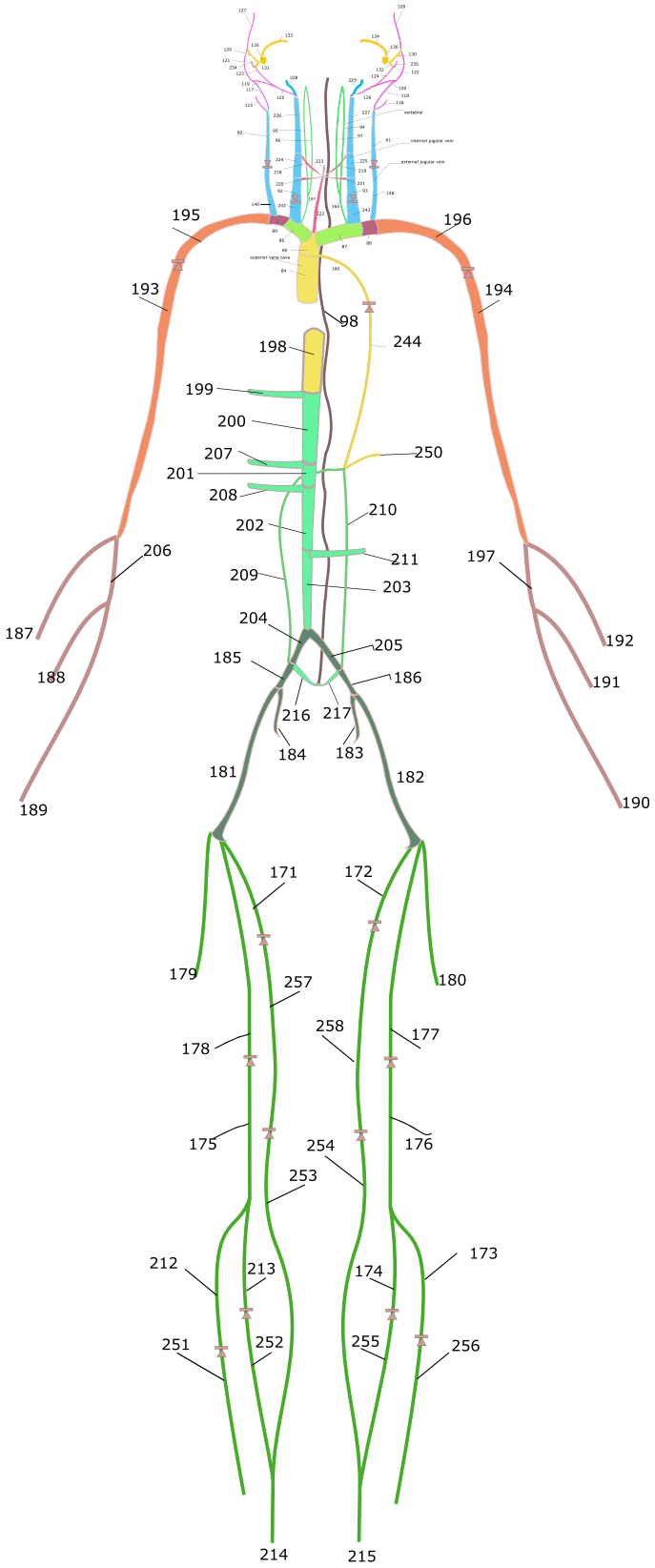

FIGURE 36 Section 3. Schematic representation of the 1D systemic venous tree.[6,7]

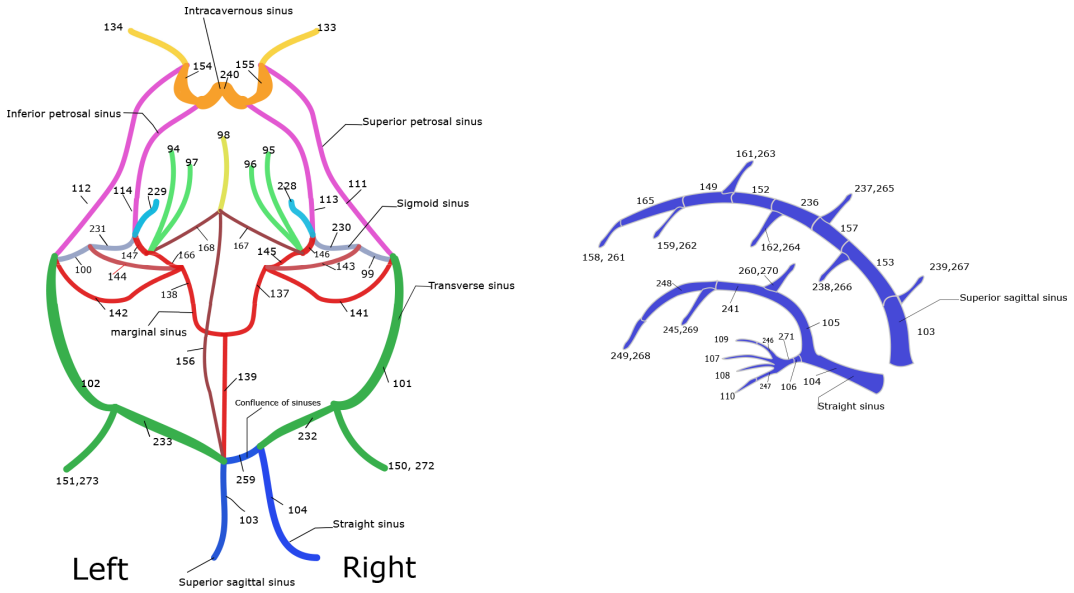

FIGURE 37 Section 3. Schematic representation of the 1D head veins.[6,7]

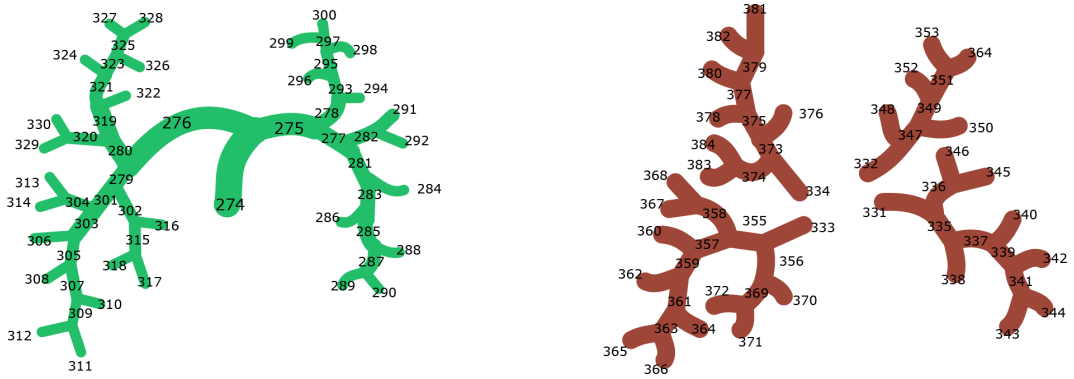

FIGURE 38 Section 3. Schematic representation of the 1D pulmonary circulation.[8]

$$\Delta t_w = CFL\ \Delta t_{min,w}, \qquad \Delta t_{min,w} = \frac{\Delta x}{\max\left\{\left|S^{\star}_{g,k}\right| + \left|\lambda^{\star}_{1g,k}\right|\right\}}. \tag{125}$$

Numerical simulation of the passive head-up tilt is performed defining the vessel elevation of each cell vessel as a function of time $\eta(t) = \eta_{max}\sin(\alpha_T(t))$, where η_{max} is the effective length of the cell vessel and $\alpha_T(t)$ is the tilt angle, that represents the orientation of the particular vessel segment with respect to the horizontal plane. The time course of $\alpha_T(t)$ is given by

$$\alpha_T(t) = \begin{cases} 0, & t \le 0.8 \\ \frac{\pi}{2}(t-1), & 0.8 \le t \le 1.8 \\ \frac{\pi}{2}, & t > 1.8 \end{cases}. \tag{126}$$

This rapid tilt from the supine posture to the head-up induces strong accelerations in the flow and changes in the pressure distribution. The HUT simulated in this section is rapid and completed in only one second. Therefore, the

centrifugal force might be not negligible compared with gravity. In this work we will not consider this point in the computational model since we are focused on the coupling method. The head-up tilt maneuver is performed after periodicity in supine position is reached. As will be shown in the results, only a few seconds are necessary in the model to reach periodicity after the postural change. Is this verified on all vessels, including venous vessels and the related peripheral beds.

3.1 | Effect of HUT in the systemic arterial tree

The evolution of the pressure, flow and *SI* in different systemic arteries is plotted in Figures 39 and 40 in the proximal (x_o), medium (x_1) and distal (x_2) computational cell to the heart. In all the arteries, the flow is kept under subsonic conditions.

Figure 39 (upper) shows how in the ascending aorta a drop in both systolic and diastolic pressure is produced during the head tilt up, due to the overall shift of fluid volume produced by this postural maneuver. The maximum value of aortic blood flow increases suddenly during the head tilt up, as heart collects more volume from the neck and cranial regions, and finally decreases smoothly.

Pressure evolution in the right radius and in the upper limbs is plotted in Figure 39 (middle) and (lower) respectively. In this case and increase in the pressure is observed, due to the presence of the hydrostatic contribution due to the blood column between the heart and the vessel. Despite of the large amount of flow circulating along the abdominal aorta, if compared to the flow in the in the right radius, a nearly equal increase in pressure is observed, as the hydrostatic pressure contribution is similar.

A large blood column between the heart and the right posterior tibial artery in the lower limbs results in a large pressure increase, as plotted in plotted in Figure 40. The maximum value of blood flow increases suddenly during the head tilt up, decreasing smoothly to achieve a new stationary maximum value, close to the initial one in the supine position. In the vessels located above the heart, the fluid column produces the opposite effect, and the pressure decreases, as can be seen in Figure 40 (middle) and (lower), for the right internal carotid artery in the neck and the right superficial temporal frontal branch in the extracranial region. In this case, the maximum value of blood flow rate is attenuated during the head tilt up and recovers smoothly over time.

3.2 | Effect of HUT in the systemic venous tree

Contrary to arterial flow, the tracings of the venous flow wave are said to be biphasic due to the presence of alternating peaks and troughs, as shown in Figure 41. The same applies to the venous pressure pulse, where also, very low variations around the mean pressure are observed if compared with arteries. The rapid postural change reproduced here leads to a very interesting description of the fluid dynamics behavior in the venous circulation.

Figure 41 shows the evolution in time for flow and pressure for the superior vena cana I and II (No. 84 and 85) and the Azygos vein (No. 160) connected by the same junction. The high compliance of the vena cava leads to large variations in the *SI* in this vein. The HUT increases suddenly the flow from the neck and cranial region towards the right atria while the contribution of the hydrostatic pressure leads to a dramatic reduction of the vena cava area (up to 60%). As a result, while subsonic conditions appear in the connecting cell of vena cava I with the right atrium, supersonic flow conditions are reached within this vein. Sonic conditions are observed in vena cava II during HUT. Flow in the Azygos I vein, which is much stiffer than the vena cava, remains subsonic. The methodology used to solve the JRP is capable of handling the subsonic, sonic and supersonic conditions that appear simultaneously in these three vessels.

In the Azygos I vein, located below the heart, the effect of HUT causes a displacement of the fluid towards the lower part of the body and a transient reverse flow appears together with a reduction of the vessel area at the proximal point. Being much stiffer, the variation in vessel area is not as great as in the superior vena cava. Drainage of the reverse flow is stopped by the presence of a valve, between veins Azygos I and II (No. 244), which closes during HUT, as shown in Figure 42. In veins Azygos I and II, flow to the right atrium is restored. In vein Azygos II, which communicates the thorax with the abdomen, due to the presence of a notable fluid column, a large variation in pressure and area from the proximal to the distal point is observed in Figure 42.

The HUT also produces an increase in the collected flow through the right and left brachiocephalic veins (No. 86 and 87) as shown in Figure 43. Being more elevated that the heart, a strong reduction of the vessel area is produced and pressure becomes subatmospheric at the distal points. Strong variations in the SI are observed, leading almost to sonic flow in the left brachiocephalic vein. Figure 44 shows how the venous valve between the left internal jugular vein I and V (No. 93 and 243) is held open during HUT, producing minimal resistance. The internal jugular vein picks up flow from the intracranial region. The large reduction experienced in vessel area combined with the large flow acceleration leads to a strong variation in the *SI* index.

The stiffness of each vessel influences vessel deformation during HUT. Figure 45 shows the evolution of the vessel ratio area α for the left internal jugular vein II (No. 225), the right transverse sinus I (n^o 101) and the confluence of sinuses (n^o 259), both in the dural sinuses. The transverse sinuses are two areas under the brain that allow blood to drain from the confluence of the sinuses, the back of the head, and send the flow into the internal jugular vein. While the left internal jugular vein II experiences a huge reduction in vessel area, due to the physiologically rigid nature of the dural sinuses, the vessel area in the right transverse sinus and sinus confluence remains almost unaltered. All three vessels experience a large variation in pressure. The flow at the confluence of the sinuses remains almost zero during HUT, whereas the flow through the right transverse sinus temporarily increases.

The sudden change in posture has also an impact in the flow in the inferior vena cava. Figure 46 shows the evolution in time for flow and pressure for the inferior vena cava (vessels No. 198 and No. 199) and the hepatic vein (vessel No. 200) connected by the same junction. The displacement of volume in the thorax and abdomen towards the lower part of the body leads to reverse flow conditions in these three vessels. This volume shift produces a great acceleration of the flow. On the other hand, the right atrium controls the pressure wave form and therefore the pressure in the proximal point connecting the inferior vena cava with the right atrium. As consequence, although in this proximal point the change in vessel are is not of relevance, sonic flow or limiting flow conditions are produced. In the rest of the inferior cava, a large vessel area deformations are observed, as a result of the presence of the column of fluid.

When HUT is initiated, the valve located between the left subclavian vein III and left subclavian vein II in the upper limbs closes almost immediately, preventing the evolution of retrograde flow, as shown in Figure 47. During valve closure, the pressure changes in both vessels according to their position in the fluid column, resulting in large vessel area deformations. Once the new pressure levels are established, the valve opens and the biphasic flow to the right atrium is established again.

Being in the most distal position, the performance of the valve located between the left anterior tibial veins I and II during the HUT is shown in Figure 48 (upper). The valve is closed for a shorter time interval. In both vessels, area increases up to 30% leading to an storage of fluid. Figure 49 show the evolution of flow and pressure across the vascular bed connecting the left posterior tibial artery (No. 54) with the left posterior tibial vein I (No. 256). The raise in pressure in the left posterior tibial artery is almost immediate, but the raise in pressure of the posterior tibial vein I increases smoothly in time. The evolution of the transmural pressure in the compartments of the vascular bed implies and increase of the stored fluid in the same bed, in particular in the venous segment. Once steady conditions are restored, the pressure in the posterior tibial vein becomes approximately 100 mmHg, which is consistent with the in vivo measurements.[47]

3.3 | Effect of HUT in the pulmonary tree

Figure 50 shows the evolution for flow and pressure for the vascular bed 54 (upper) connecting terminal artery RSA4 1 52 (No. 328) (middle) with collecting vein RSV4 1 52 (No. 328) (lower), in the upper part of the lungs. In this model the effect of the HUT does not lead to relevant changes in the pressure and the flow wave form in the vascular tree in the lungs.

3.4 | Effect of HUT in the heart model

Figure 51 shows the evolution of flow, pressure and volume in the right heart (upper) and in the left heart (lower). The injection of flow from the inferior and superior vena cava to the right atrium (Q_{vc} in Figure 51 (upper)) is reduced leading briefly to reverse flow conditions at its inflow during HUT. This effect is produced by the shift of volume in the inferior vena cava (46) that is attenuated by the increase in flow received towards the right atrium by the superior vena cava (Figure 41). As a consequence of the appearance of reversal flow, the tricuspid valve briefly closes and reversal

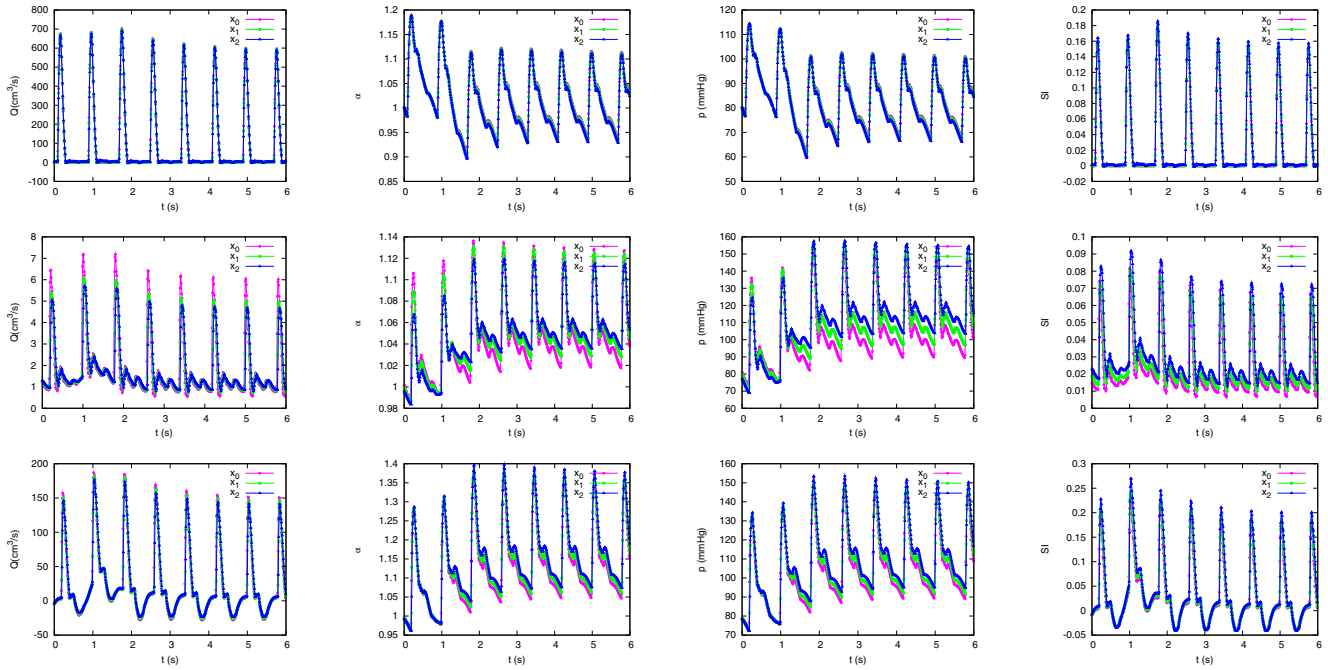

FIGURE 39 Section 3.1. Numerical solutions for the ascending aorta I in the thorax (No. 84) (upper), for the right radius in the upper limbs (No. 8) (middle) and for the abdominal aorta v (No. 33) (lower).

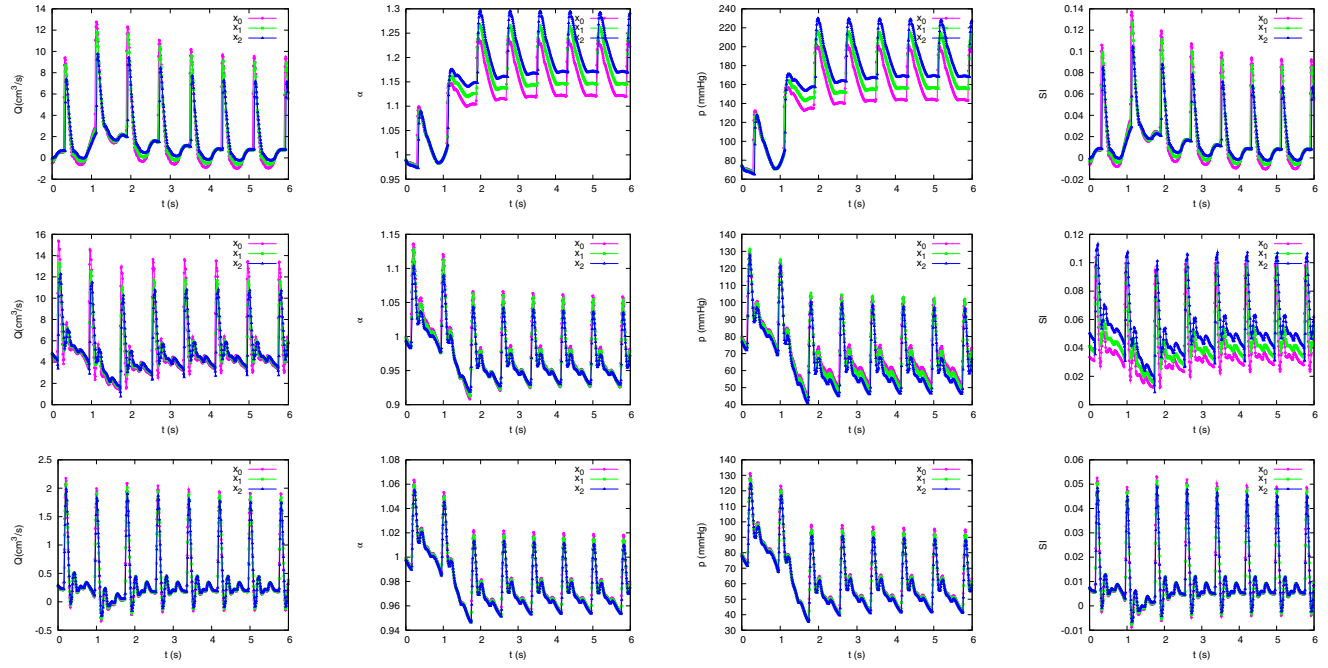

FIGURE 40 Section 3.1. Numerical solutions for the right posterior tibial artery (No. 41) in the lower limbs (upper), for the right internal carotid artery I (No. 47) in the neck (middle)and for the right superficial temporal frontal branch (No. 81) in the extracranial region (lower).

flow in the inlet ceases. The decrease in the injection of flow in the right ventricle through the tricuspid valve (Q_{tri}) leads to a noticeable reduction of the end-diastolic volume (EDV) in the right ventricle and of the peak flow through the pulmonary valve (Q_{pul}), that is partially recovered later. Both end-systolic volume (ESV) and EDV decrease in the right ventricle, but the reduction of the EDV is larger than the reduction in the ESV, leading to a reduction of the cardiac output in the pulmonary valve. Systolic and diastolic pressures decrease in the main pulmonary artery (No. 274).

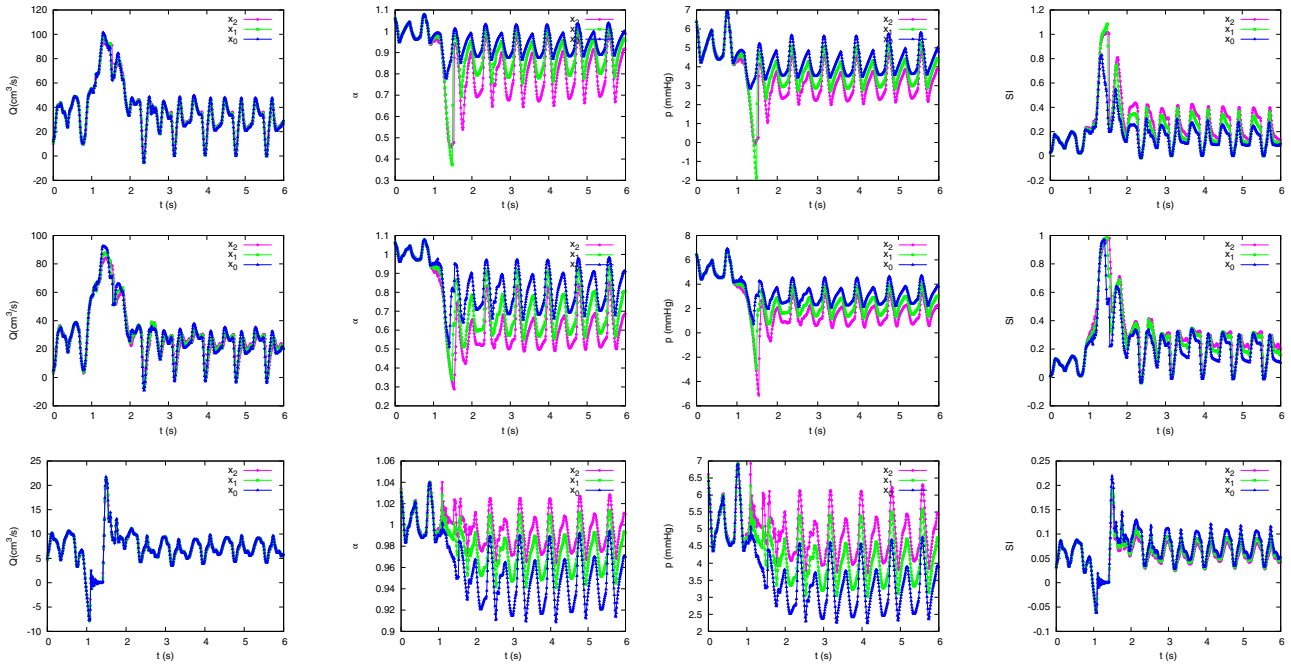

FIGURE 41 Section 3.2. Numerical solutions for the superior vena cava I (upper) (No. 84), for the superior vena cava II (No. 85) (middle) and for the Azygos vein I (No. 160) (lower), in the thorax.

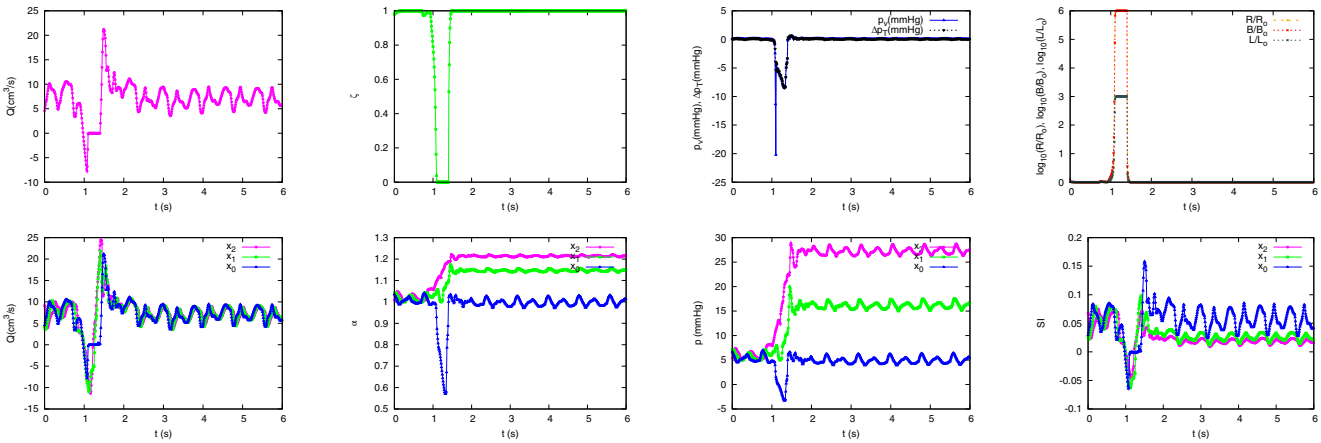

FIGURE 42 Section 3.2. Numerical solutions for valve 7 (upper), between the Azygos vein II (No. 244) (middle) and the Azygos vein I (No. 160) (lower) in the thorax.

The injection of flow from the left/right inferior/superior pulmonary veins (No. 331, 332, 333, 334), Q_{pv} in Figure 51 (lower), to the left atrium does not experience a significant variation, and the same is valid for the mitral valve, Q_{mit}. The peak flow in the aortic valve initially increases during the HUT and then decreases smoothly. The reduction of the end-systolic volume (ESV) and end-diastolic volume (EDV) in the left ventricle due to the HUT is initially similar, but the EDV continues to reduce smoothly in time leading to a decrease of the cardiac output in the aortic valve.

3.5 | Volume shift after HUT

In this section the fluid volume redistribution is considered. During HUT, gravity induces a primary rapid intravascular fluid shift. A secondary slow fluid shift appears, from the intravascular to the interstitial fluid compartment. In this numerical experiment, we only consider primary rapid intravascular fluid shift. Figure 52 shows the variation of

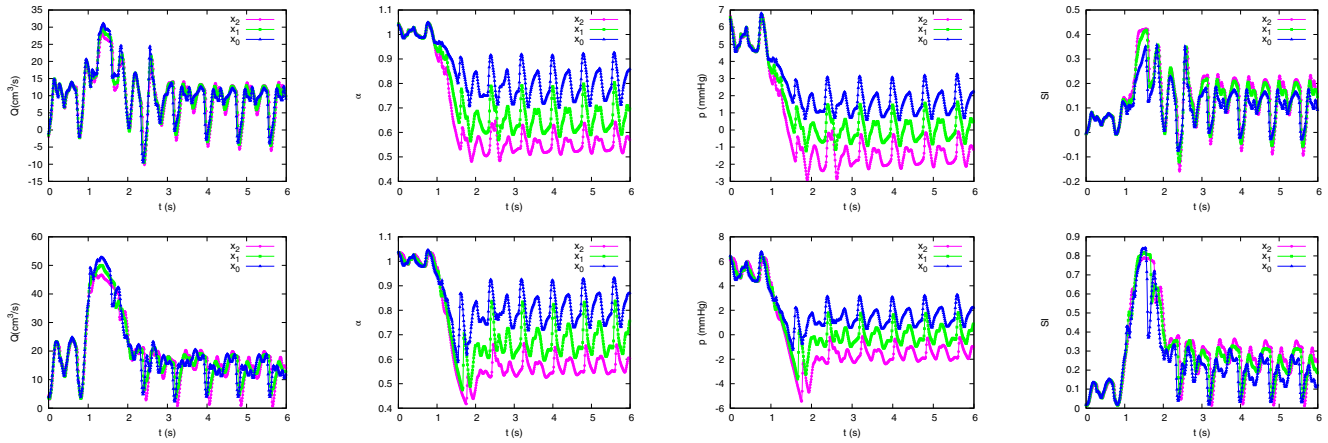

FIGURE 43 Section 3.2. Numerical solutions for the right brachiocephalic vein (No. 86) (upper) and for the left brachiocephalic vein (No. 87) (lower) in the thorax.

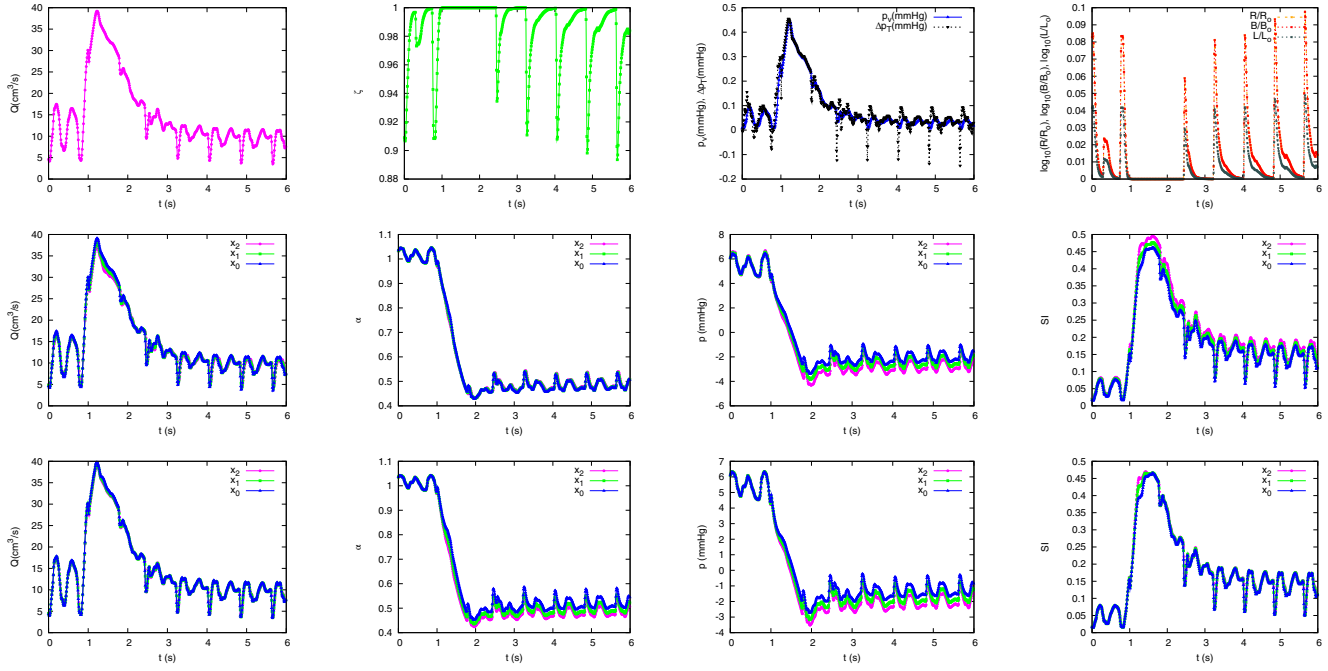

FIGURE 44 Section 3.2. Numerical solutions for valve 4 (upper) between the left internal jugular vein I (No. 93) (middle) and the left internal jugular vein V (No. 243) (lower) in the neck.

stressed or intravascular volume in body regions in time for: (left) the Right upper limbs (RUL), the Left upper limbs (LUL), the Right lower limbs (RLL)and the Left lower limbs (LLL); (middle) the dural sinuses (DS), the extracranial region (EC), the intracranial region (IC), the neck and the pelvis; (right) the dural thorax, the abdomen and the lungs for a 1 s HUT from the supine position to 80°. Numerical results are almost equal to those provided when a 1 s HUT from the supine position to 90° is performed.

The volume variation in each anatomical region is compared with the results provided a lumped parameter model in Reference 48 in Table 6. This model includes the left and right heart, ventricular interaction through the septum and pericardium, the systemic and pulmonary circulations, nonlinear pressure volume relationship of the lower body compartment, arterial and cardiopulmonary baroreceptors, and autoregulatory mechanisms. The systemic circulation was divided in six parallel vascular districts: cerebral, upper body, coronary, splanchnic, renal, and lower body which

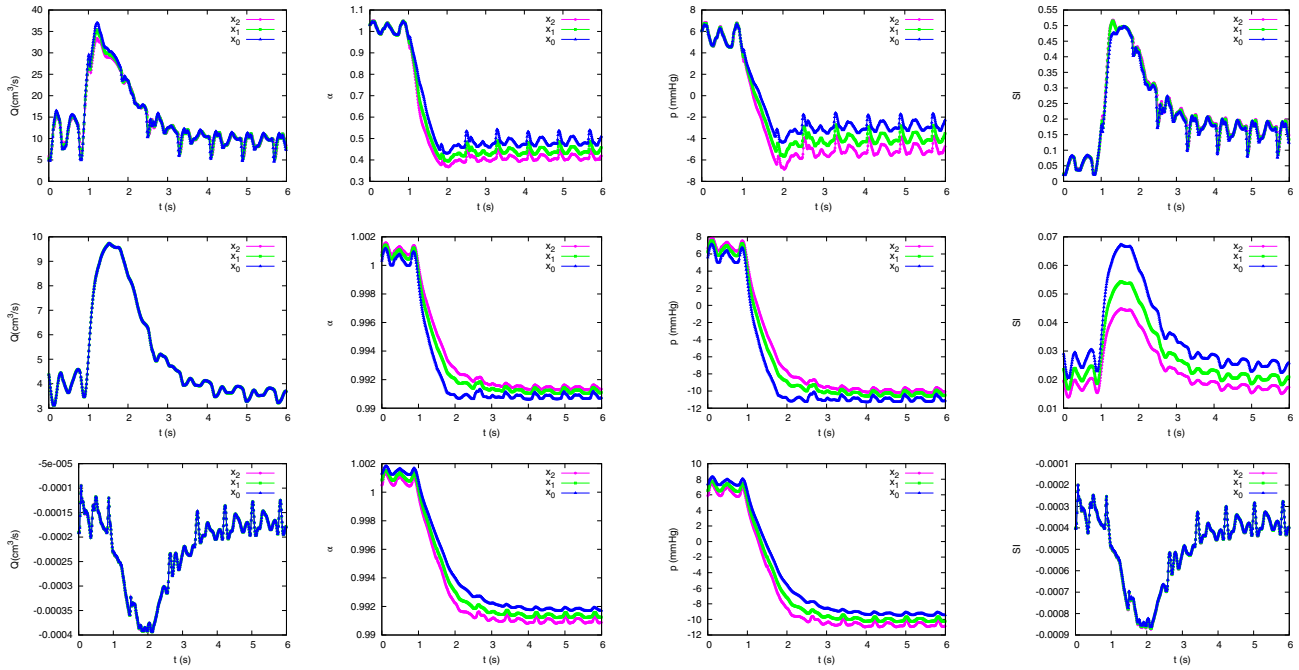

FIGURE 45 Section 3.2. Numerical solutions for the left internal jugular vein II in the neck (No. 225) (upper), for the right transverse sinus I in the Dural sinuses (No. 101) (middle) and the confluence of sinuses in the Dural sinuses (No. 257) (lower).

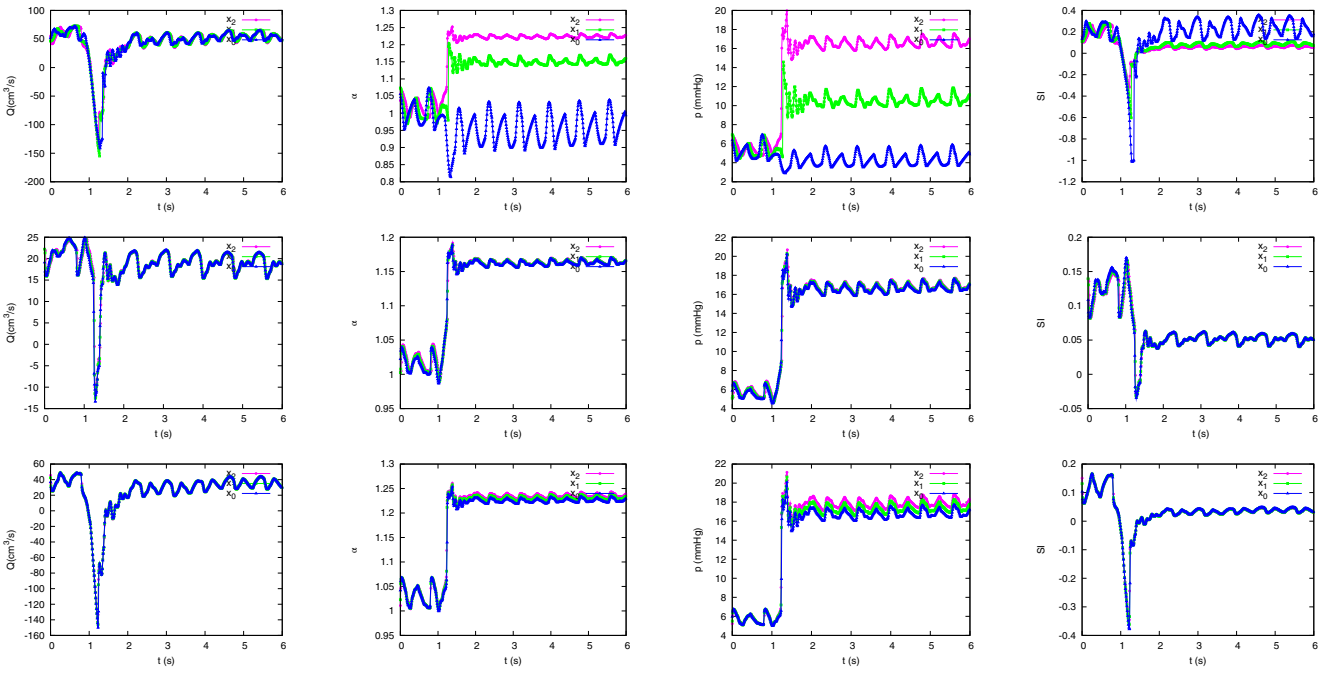

FIGURE 46 Section 3.2. Numerical solutions for vessel the inferior vena cava I (No. 198) (upper), for the hepatic vein in the abdomen (No. 199) (middle), and for the inferior vena cava II (No. 200) (lower).

includes the leg and pelvic region, accounting for the hydrostatic reference point located at the heart level. The model was optimized using experimental data during graded head-up tilt (HUT) from the supine position to 80°.

In this section we made a rough comparison between the results of this two different models. Figure 52 shows how once the new stationary state is achieved the volume in the dural sinues is almost unaltered. Dural sinues are located in

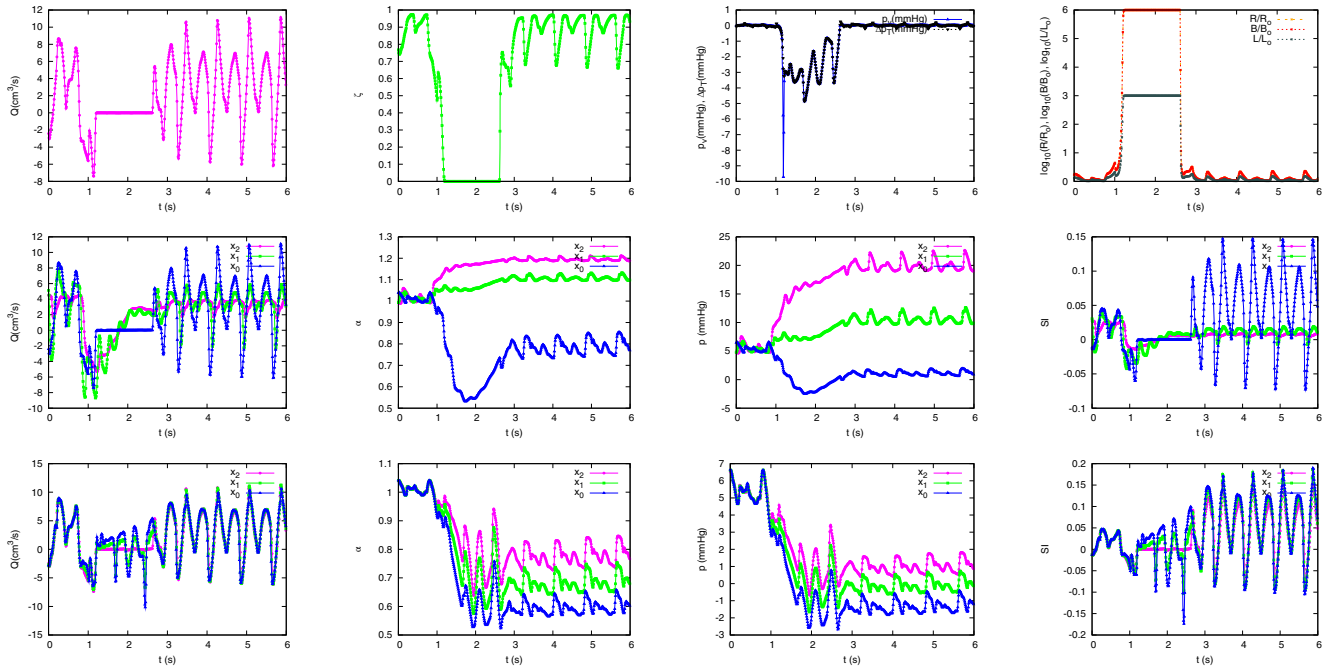

FIGURE 47 Section 3.2. Numerical solutions for valve 5 (upper) between the left subclavian vein III (No. 193) (middle) and the left subclavian vein II (No. 195) (lower) in the upper limbs.

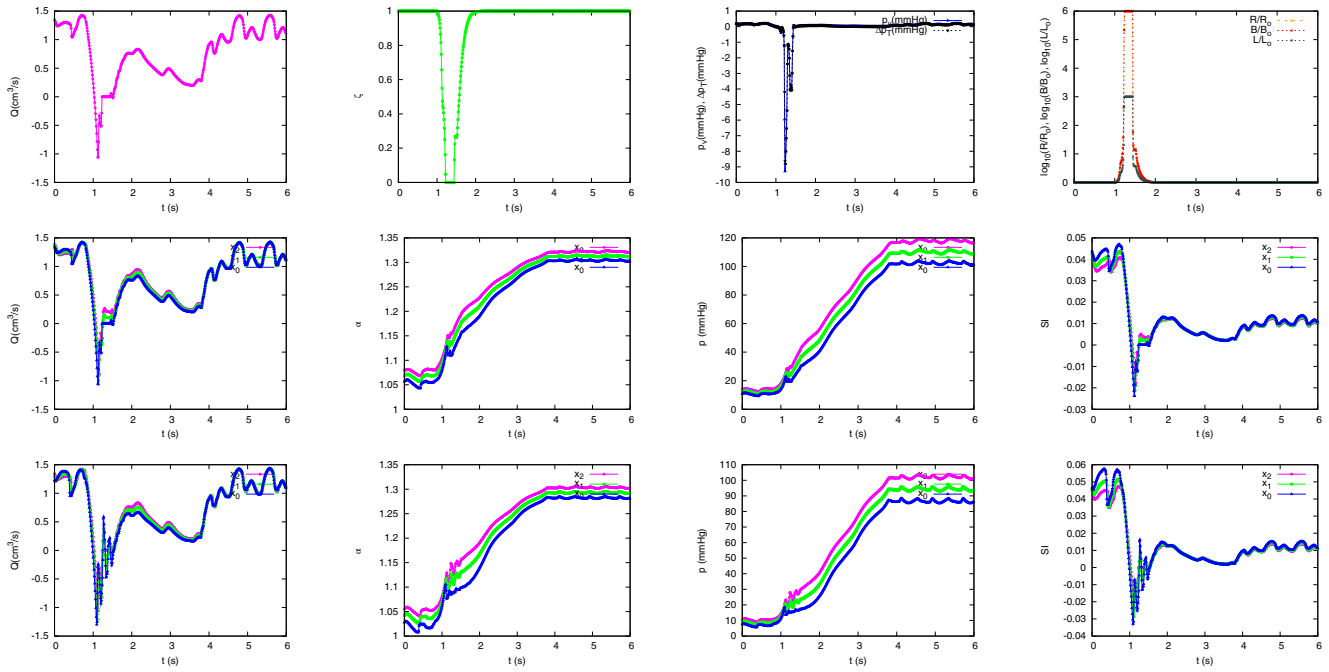

FIGURE 48 Section 3.2. Numerical solutions for valve 9 (upper) between the left posterior tibial vein I (No. 256) (middle) and the left posterior tibial vein I (No. 173) (lower), in the lower limbs.

the dura mater and are more rigid than cerebral veins. Extracranial and intracranial volume strongly decreases (−47.77% and −93.84, respectively) with a more moderate variation of volume in the neck (−19.11%). The decrease in total volume in our model for the cerebral circulation (CC) is attenuated up to −37.43%, smaller than the one predicted in Reference 48 (−52.40%). Thorax and lungs experience a less severe decrease of stressed volume, −7.14% (−29.20%[48]).

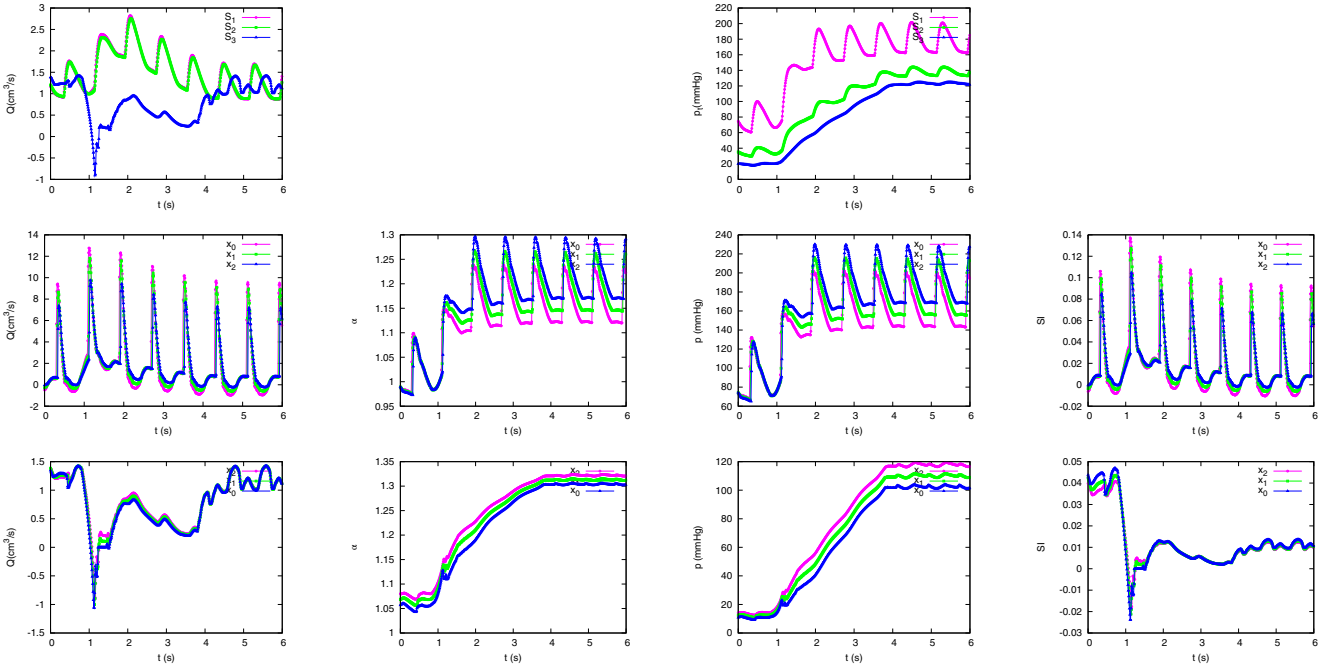

FIGURE 49 Section 3.2. Numerical solutions for vascular bed 11 (upper) connecting the left posterior tibial artery (No. 54) (middle) with the left posterior tibial vein I) (No. 256) (lower), in the lower limbs.

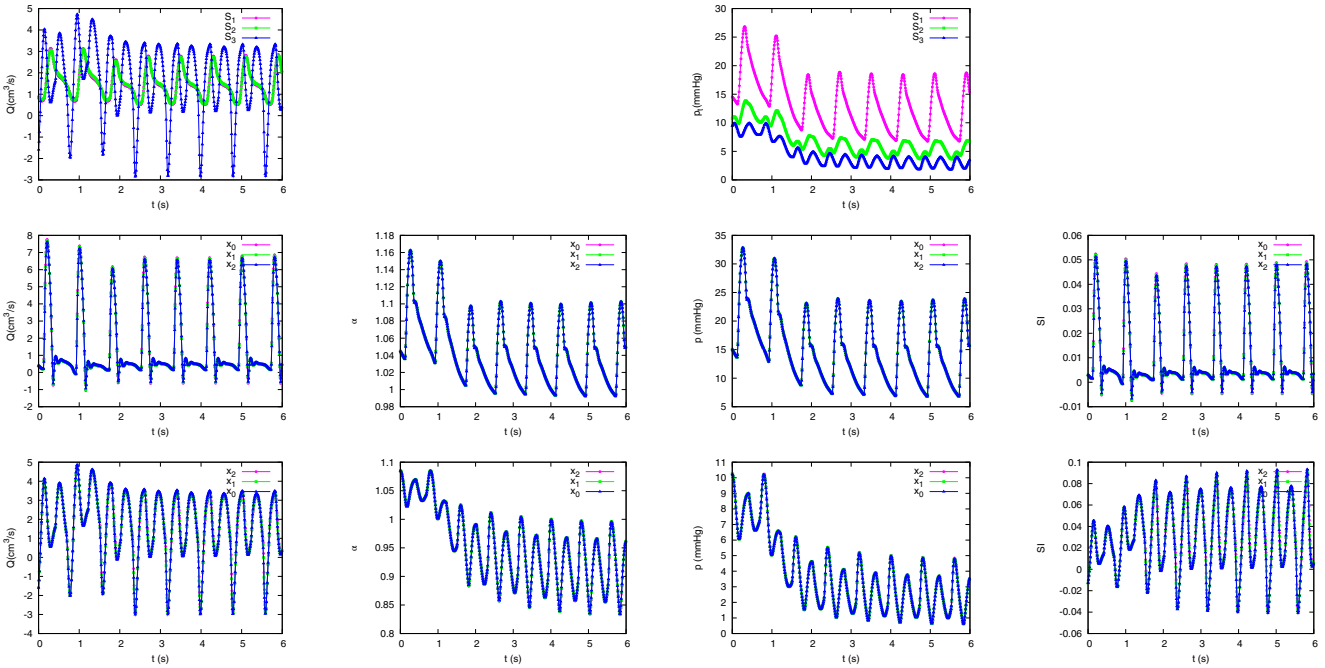

FIGURE 50 Section 3.3. Numerical solutions for vascular bed 54 (upper) connecting terminal artery RSA4 1 52 (No. 328) (middle) with collecting vein RSV4 1 52 (No. 328) (lower) in the lungs.

The upper limbs experience a moderate increase in volume (11.91%), while in Reference 48 a moderate decrease is predicted (−16.20%). The lower body region experiences a large increase of fluid volume in our model, up to 46.03%, almost the double than the one predicted in Reference 48 (25.50%). Differences can be attributed to the lack of regulatory systems in our model. The rapid intravascular fluid shift from the cerebral and thoracic regions to the rest of the vasculature triggers the cardiopulmonary reflex that counteracts the reduction in arterial pressure and central blood volume.

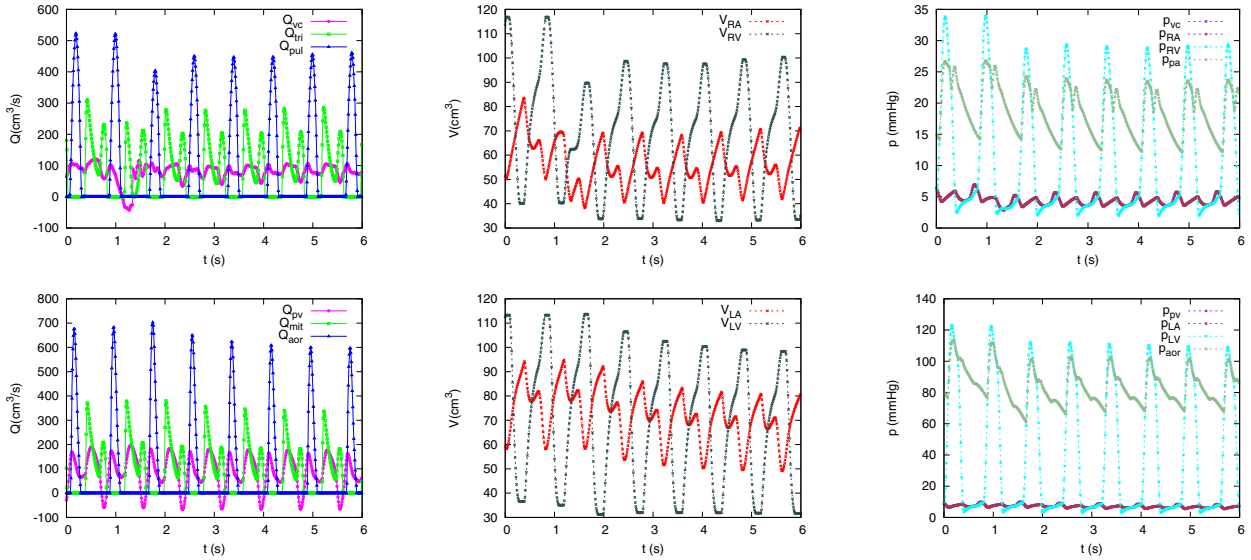

FIGURE 51 Section 3.4. Numerical solutions for the right heart (upper) and for the left heart (lower).

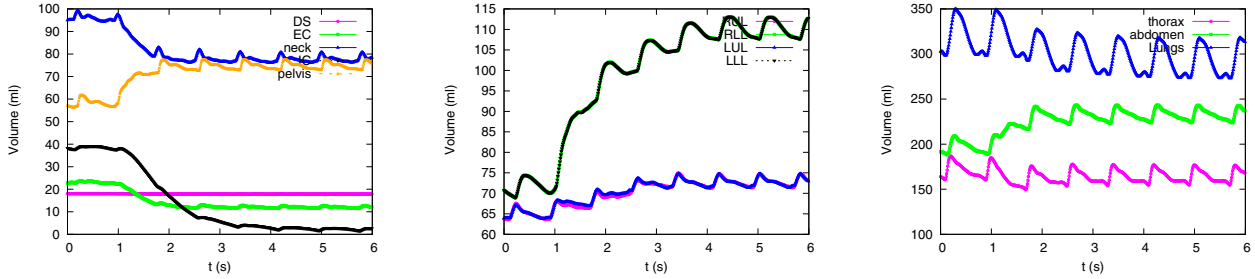

FIGURE 52 Section 3.5. Variation of stressed or intravascular volume in body regions for a 1 s HUT from the supine position to 80° in time for: (left) the Right upper limbs (RUL), the Left upper limbs (LUL), the Right lower limbs (RLL)and the Left lower limbs (LLL); (middle) the dural sinuses (DS), the extracranial region (EC), the intracranial region (IC), the neck and the pelvis; (right) the dural thorax, the abdomen and the lungs.

TABLE 6 Section 3.5. Stressed volume in body regions and stressed volume variation after 80° HUT.

Region	0° HUT	80° HUT	ΔV	ΔV[48]
DS (ml)	18.05	17.88	−0.96%	
EC (ml)	23.13	12.08	−47.77%	
IC (ml)	38.63	2.38	−93.84%	
Neck (ml)	96.03	77.68	−19.11%	
CC (ml)	175.84	110.02	−37.43%	−52.40%
Thorax (ml)	171.67	164.06	−4.43%	
Lungs	319.07	291.62	−8.60%	
Thorax and lungs (ml)	490.74	455.69	−7.14%	−29.20%
Abdomen (ml)	197.60	232.62	17.72%	
RUL (ml)	65.03	72.79	11.93%	
LUL (ml)	64.99	72.72	11.89%	
Upper body (ml)	130.02	145.51	11.9%	−16.20%
RLL (ml)	71.86	110.28	53.48%	
LLL (ml)	71.86	110.28	53.48%	
Pelvis	58.51	74.74	27.74%	
Lower body (ml)	202.23	295.31	46.03	25.50%

4 | CONCLUSIONS

The numerical procedure defined for solving the JRP in Reference 33 has been extended to different scenarios. One of the applications is numerical modeling of valves. The numerical extension of JRP proposed in Section 2.3 can handle the VRP under any conditions. These include, among others, sonic limiting in an initially closed valve, characterized by a total energy jump greater than the pressure drop generated by the valve resistance and the closure of an initially open valve under supersonic backward flow conditions.

The solution of the JRP can be extended if other than subsonic flow conditions are of interest in vascular beds, as done in Section 2.4. The correct modeling and coupling between terminal vessels and lumped models representing vascular bed has been tested including conditions of limiting flow even when departing from supersonic conditions. We have shown how the presence of the serially arranged compartments in combination with a proper distribution of the lumped parameters has almost no influence on the solution for the terminal vessel. Differences are more noticeable when a collecting vessel is defined. The presence of collecting vessels generates an extra resistance to flow advance due to its own impedance, that generates an opposition to passage of pressure waves.

In Section 2.5, the coupling between vessels and a heart model has been tested in different scenarios, in which the activation function of the heart has been neglected in order to define understandable scenarios while involving complex initial conditions. To analyze the behavior of the proposed numerical methodology for modeling the heart, all vessels have been defined as veins, which are much more deformable than arteries. Numerical experimentation shows how it is possible to handle problems with any value of the initial conditions, including those leading to flow limitation or valve opening and closing under supersonic conditions.

The numerical methods presented for the VRP, vascular beds and heart modeling can be easily modified if other valve, vascular or heart models are desired. The numerical methods presented are independent of the 1D solver used to compute the flow evolution in the vessels.

In Section 3 the effect of HUT in an integrated closed model of the CVS has been analyzed. Considering that in this work we focus only on the mathematical coupling of the vessel network with the internal boundary conditions, the several critical auto-regulations mechanism of the cerebro-cardiovascular system, among others, were not included in the mathematical model of this study. We have demonstrated the potential and capability of the numerical techniques presented here when dealing with the sudden change in flow conditions. Even the predictions, when the new steady conditions after HUT are achieved, show how venous and arterial pressure are modified by the presence of a continuous hydrostatic column, the transient flow regime is of great complexity, in particular in the veins located in the thorax, leading, in this model, to limiting flow conditions in the right atrium.

The set of numerical experiments presented here when testing the different numerical models described in this manuscript in Sections 2.3, 2.4 and 2.5 have no clinical relevance. But when numerical experiments are used to predict the evolution of flow and pressure during a sudden postural maneover in a closed-loop, multiscale mathematical model as done in Section 2.5, it is necessary to ensure that the techniques used are capable of handling any flow condition. Sonic or supersonic conditions are not expected throughout the simulation, but if the evolved states of the solution do not converge in a coupling element in a given time the solution methods fail and the simulation is ruined. Therefore, after first showing the potential and capability the numerical methods in limit situations, we can be assured that the predictions of the closed-loop model are in agreement with the fundamental basis of the mathematical models used.

ACKNOWLEDGEMENTS

This work has been funded by Gobierno de Aragón through Fondo Social Europeo (T32-20R and E24-17R, Feder 2019-2021 "Construyendo Europa desde Aragón").

CONFLICT OF INTEREST STATEMENT

The authors declare that there is no conflict of interest.

DATA AVAILABILITY STATEMENT

Data available on request from the authors.

REFERENCES

1. Morgan P, Parker K. A mathematical model of flow through a collapsible tube–I. Model and steady flow results. *J Biomech*. 1989;22(11): 1263-1270. doi:10.1016/0021-9290(89)90229-7

2. Pedley T, Luo X. Modelling flow and oscillations in collapsible tubes. *Theor Comput Fluid Dyn*. 1998;10:277-294.
3. Bassez S, Flaud P, Chauveau M. Modeling of the deformation of flexible tubes using a single law: application to veins of the lower limb in man. *J Biomech Eng*. 2001;123(1):58-65. doi:10.1115/1.1336143
4. Marchandise E, Flaud P. Accurate modelling of unsteady flows in collapsible tubes. *Comput Methods Biomech Biomed Engin*. 2010;13(2):279-290. PMID: 20373183. doi:10.1080/10255840903190726
5. Ho H, Mithraratne K, Hunter P. Numerical simulation of blood flow in an anatomically-accurate cerebral venous tree. *IEEE Trans Med Imaging*. 2013;32:85-91.
6. Müller LO, Toro EF. A global multiscale mathematical model for the human circulation with emphasis on the venous system. *Int J Numer Methods Biomed Eng*. 2014;30(7):681-725. doi:10.1002/cnm.2622
7. Müller LO, Toro EF. Enhanced global mathematical model for studying cerebral venous blood flow. *J Biomech*. 2014;47(13):3361-3372. doi:10.1016/j.jbiomech.2014.08.005
8. Mynard JP, Smolich JJ. One-dimensional Haemodynamic modeling and wave dynamics in the entire adult circulation. *Ann Biomed Eng*. 2015;43:1443-1460. doi:10.1007/s10439-015-1313-8
9. Pfaller MR, Pham J, Verma A, et al. Automated generation of 0D and 1D reduced-order models of patient-specific blood flow. *Int J Numer Meth Biomed Eng*. 2021;38(10):e3639. doi:10.1002/cnm.3639
10. Zhang X, Noda S, Himeno R, Liu H. Gravitational effects on global hemodynamics in different postures: a closed-loop multiscale mathematical analysis. *Acta Mech Sinica*. 2017;33(3):595-618. doi:10.1007/s10409-016-0621-z
11. Shapiro AH. Steady flow in collapsible tubes. *J Biomech Eng*. 1977;99(3):126-147. doi:10.1115/1.3426281
12. Permutt SRS. Hemodynamics of collapsible vessels with tone: the vascular waterfall. *J Appl Physiol*. 1963;18(5):924-932.
13. Magder S. Volume and its relationship to cardiac output and venous return. *Crit Care*. 2016;20:271. doi:10.1186/s13054-016-1438-7
14. Guyton ACAL. Quantitative aspects of the collapse factor in relation to venous return. *Am J Phys*. 1954;177(3):523-527.
15. Siviglia A, Toffolon M. Multiple states for flow through a collapsible tube with discontinuities. *J Fluid Mech*. 2014;761:105-122. doi:10.1017/jfm.2014.635
16. Anliker M, Rockwell RL, Ogden E. Nonlinear analysis of flow pulses and shock waves in arteries. *Z Ang Math Phys*. 1971;22(2):217-246.
17. Pedley TJ. *The Fluid Mechanics of Large Blood Vessels*. Cambridge Monographs on MechanicsCambridge University Press; 1980.
18. Brook BS, Falle SAEG, Pedley TJ. Numerical solutions for unsteady gravity-driven flows in collapsible tubes: evolution and roll-wave instability of a steady state. *J Fluid Mech*. 1999;396:223-256. doi:10.1017/S0022112099006084
19. Brook B, Pedley T. A model for time-dependent flow in (giraffe jugular) veins: uniform tube properties. *J Biomech*. 2002;35(1):95-107. doi:10.1016/S0021-9290(01)00159-2
20. Fullana JM, Zaleski S. A branched one-dimensional model of vessel networks. *J Fluid Mech*. 2009;621:183-204. doi:10.1017/S0022112008004771
21. Murillo J, Navas-Montilla A, García-Navarro P. Formulation of exactly balanced solvers for blood flow in elastic vessels and their application to collapsed states. *Comput Fluids*. 2019;186:74-98. doi:10.1016/j.compfluid.2019.04.008
22. Sherwin SJ, Formaggia L, Peiró J, Franke V. Computational modelling of 1D blood flow with variable mechanical properties and its application to the simulation of wave propagation in the human arterial system. *Int J Numer Methods Fluids*. 2003;43(6–7):673-700. doi:10.1002/fld.543
23. Delestre O, Lagrée PY. A 'well-balanced' finite volume scheme for blood flow simulation. *Int J Numer Methods Fluids*. 2013;72(2):177-205. doi:10.1002/fld.3736
24. Müller LO, Toro EF. Well-balanced high-order solver for blood flow in networks of vessels with variable properties. *Int J Numer Methods Biomed Eng*. 2013;29(12):1388-1411. doi:10.1002/cnm.2580
25. Murillo J, García-Navarro P. A roe type energy balanced solver for 1D arterial blood flow and transport. *Comput Fluids*. 2015;117:149-167. doi:10.1016/j.compfluid.2015.05.003
26. Toro EF, Siviglia A. Flow in collapsible tubes with discontinuous mechanical properties: mathematical model and exact solutions. *Commun Comput Phys*. 2013;13(2):361-385. doi:10.4208/cicp.210611.240212a
27. Müller LO, Parés C, Toro EF. Well-balanced high-order numerical schemes for one-dimensional blood flow in vessels with varying mechanical properties. *J Comput Phys*. 2013;242:53-85. doi:10.1016/j.jcp.2013.01.050
28. Murillo J, García-Navarro P. Augmented versions of the HLL and HLLC Riemann solvers including source terms in one and two dimensions for shallow flow applications. *J Comput Phys*. 2012;231(20):6861-6906. doi:10.1016/j.jcp.2012.06.031
29. Sherwin S, Franke V, Peiró J, Parker K. One-dimensional modelling of a vascular network in space-time variables. *J Eng Math*. 2003;47(3/4):217-250. doi:10.1023/b:engi.0000007979.32871.e2
30. Huang PG, Muller LO. Simulation of one-dimensional blood flow in networks of human vessels using a novel TVD scheme. *Int J Numer Methods Biomed Eng*. 2015;31(5):e02701. doi:10.1002/cnm.2701
31. Müller LO, Blanco PJ. A high order approximation of hyperbolic conservation laws in networks: application to one-dimensional blood flow. *J Comput Phys*. 2015;300:423-437. doi:10.1016/j.jcp.2015.07.056
32. Bellamoli F, Müller LO, Toro EF. A numerical method for junctions in networks of shallow-water channels. *Appl Math Comput*. 2018;337:190-213. doi:10.1016/j.amc.2018.05.034
33. Murillo J, García-Navarro P. A solution of the junction Riemann problem for 1D hyperbolic balance Laws in networks including supersonic flow conditions on elastic collapsible tubes. *Symmetry*. 2021;13(9):1658. doi:10.3390/sym13091658

34. Alastruey J, Parker KH, Peiró J, Sherwin SJ. Lumped parameter outflow models for 1-D blood flow simulations: effect on pulse waves and parameter estimation. *Commun Comput Phys*. 2008;4(2):317-336.
35. Xiao N, Alastruey J, Alberto FC. A systematic comparison between 1-D and 3-D hemodynamics in compliant arterial models. *Int J Numer Methods Biomed Eng*. 2014;30(2):204-231. doi:10.1002/cnm.2598
36. Mynard JP, Davidson MR, Penny DJ, Smolich JJ. A simple, versatile valve model for use in lumped parameter and one-dimensional cardiovascular models. *Int J Numer Methods Biomed Eng*. 2012;28(6–7):626-641. doi:10.1002/cnm.1466
37. Toro EF, Celant M, Zhang Q, et al. Cerebrospinal fluid dynamics coupled to the global circulation in holistic setting: mathematical models, numerical methods and applications. *Int J Numer Methods Biomed Eng*. 2022;38(1):e3532. doi:10.1002/cnm.3532
38. Borsche R, Kall J. High order numerical methods for networks of hyperbolic conservation laws coupled with ODEs and lumped parameter models. *J Comput Phys*. 2016;327:678-699. doi:10.1016/j.jcp.2016.10.003
39. LeVeque RJ. Balancing source terms and flux gradients in high-resolution Godunov methods: the quasi-steady wave-propagation algorithm. *J Comput Phys*. 1998;146(1):346-365. doi:10.1006/jcph.1998.6058
40. Toro E. *The ADER Path to High-Order Godunov Methods*. Springer International Publishing; 2020:359-366.
41. Keijsers J, Leguy C, Huberts W, Narracott A, Rittweger J, van de Vosse FN. Global sensitivity analysis of a model for venous valve dynamics. *J Biomech*. 2016;49(13):2845-2853. doi:10.1016/j.jbiomech.2016.06.029
42. Liang F, Takagi S, Himeno R, Liu H. Multi-scale modeling of the human cardiovascular system with applications to aortic valvular and arterial stenoses. *Med Biol Eng Comput*. 2009;47(7):743-755. doi:10.1007/s11517-009-0449-9
43. Liang F, Takagi S, Himeno R, Liu H. Biomechanical characterization of ventricular–arterial coupling during aging: a multi-scale model study. *J Biomech*. 2009;42:692-704.
44. Su Y, Beshara M, Lucariello R, Chiaramida S. A comprehensive model for right-left heart interaction under the influence of pericardium and baroreflex. *Am J Phys*. 1997;272:H1499. doi:10.1152/ajpheart.1997.272.3.H1499
45. Simon AC, Safar ME, Levenson JA, London GM, Levy BI, Chau NP. An evaluation of large arteries compliance in man. *Am J Physiol Heart Circ Phys Ther*. 1979;237(5):H550. doi:10.1152/ajpheart.1979.237.5.H550
46. Najjar E, Lund LH, Hage C, Nagy AI, Johnson J, Manouras A. The differential impact of the left atrial pressure components on pulmonary arterial compliance–resistance relationship in heart failure. *J Card Fail*. 2021;27(3):277-285. doi:10.1016/j.cardfail.2020.09.008
47. Meissner MH. Lower extremity venous anatomy. *Semin Interv Radiol*. 2005;22(3):147-156.
48. Lim E, Chan GSH, Dokos S, et al. A cardiovascular mathematical model of graded head-up tilt. *PLoS One*. 2013;8(10):1-12. doi:10.1371/journal.pone.0077357

How to cite this article: Murillo J, García-Navarro P. Numerical coupling of 0D and 1D models in networks of vessels including transonic flow conditions. Application to short-term transient and stationary hemodynamic simulation of postural changes. *Int J Numer Meth Biomed Engng*. 2023;e3751. doi:10.1002/cnm.3751

APPENDIX A

A.1 | A Network

Table A1 provides the number, name, length and radii and elevation of each vessel in the network.

TABLE A1 Geometrical and mechanical parameters of the network.

No.	Vessel name	L (cm)	r_0 (cm)	r_1 (cm)	η_0 (cm)	η_1 (cm)
1	Ascending aorta I	2	1.525	1.47	0	2
2	Aortic arch I	3	1.42	1.342	2	5
3	Brachiocephalic artery	3.5	0.65	0.62	2	5.5
4	Right subclavian artery I	3.5	0.425	0.407	5.5	7.5
5	Right carotid artery	17.7	0.4	0.37	5.5	17.89
6	Right vertebral artery	13.5	0.15	0.136	7.5	21
7	Right subclavian artery II	39.8	0.407	0.23	7.5	−32.3
8	Right radius	22	0.175	0.14	−32.3	−54.3
9	Right ulnar artery I	6.7	0.215	0.215	−32.3	−39
10	Aortic arch II	4	1.342	1.246	5	5
11	Left carotid artery	20.8	0.4	0.37	5	17.89
12	Thoracic aorta I	5.5	1.246	1.124	5	−0.5
13	Thoracic aorta II	10.5	1.124	0.924	−0.5	−11
14	Intercostal artery	7.3	0.3	0.3	−0.5	−0.5
15	Left subclavian artery I	3.5	0.425	0.407	5	7.5
16	Left vertebral artery	13.5	0.15	0.136	7.5	21
17	Left subclavian artery II	39.8	0.407	0.23	7.5	−32.3
18	Left ulnar artery I	6.7	0.215	0.215	−32.3	−39
19	Left radius	22	0.175	0.14	−32.3	−54.3
20	Celiac artery I	2	0.35	0.3	−11	−11
21	Celiac artery II	2	0.3	0.25	−11	−11
22	Hepatic artery	6.5	0.275	0.25	−11	−11
23	Splenic artery	5.8	0.175	0.15	−11	−11
24	Gastric artery	5.5	0.2	0.2	−11	−11
25	Abdominal aorta I	5.3	0.924	0.838	−11	−16.3
26	Superior mesenteric artery	5	0.4	0.35	−16.3	−16.3
27	Abdominal aorta II	1.5	0.838	0.814	−16.3	−17.8
28	Right renal artery	3	0.275	0.275	−19.3	−19.3
29	Abdominal aorta III	1.5	0.814	0.792	−17.8	−19.3
30	Left renal artery	3	0.275	0.275	−17.8	−17.8
31	Abdominal aorta IV	12.5	0.792	0.627	−19.3	−31.8
32	Inferior mesenteric artery	3.8	0.2	0.175	−31.8	−31.8
33	Abdominal aorta v	8	0.627	0.55	−31.8	−39.8
34	Right common iliac artery	5.8	0.4	0.37	−39.8	−45.6
35	Right external iliac artery	14.5	0.37	0.314	−45.6	−60.1
36	Right internal iliac artery	4.5	0.2	0.2	−45.6	−50.1
37	Right deep femoral artery	11.3	0.2	0.2	−60.1	−71.4
38	Right femoral artery	44.3	0.314	0.275	−60.1	−104.4

(Continues)

TABLE A1 (Continued)

No.	Vessel name	L (cm)	r_0 (cm)	r_1 (cm)	η_0 (cm)	η_1 (cm)
39	Right external carotid artery I	4.1	0.2	0.15	17.89	21.99
40	Left internal carotid artery I	17.6	0.25	0.2	17.89	22
41	Right posterior tibial artery	34.4	0.175	0.175	−104.4	−138.8
42	Right anterior tibial artery	32.2	0.25	0.25	−104.4	−136.6
43	Right interosseous artery	7	0.1	0.1	−39	−46
44	Right ulnar artery II	17	0.203	0.18	−39	−56
45	Left ulnar artery II	17	0.203	0.18	−39	−56
46	Left interosseous artery	7	0.1	0.1	−39	−46
47	Right internal carotid artery I	17.6	0.25	0.2	17.89	22
48	Left external carotid artery I	4.1	0.2	0.15	17.89	21.99
49	Left common iliac artery	5.8	0.4	0.37	−39.8	−45.6
50	Left external iliac artery	14.5	0.37	0.314	−45.6	−60.1
51	Left internal iliac artery	4.5	0.2	0.2	−45.6	−50.1
52	Left deep femoral artery	11.3	0.2	0.2	−60.1	−71.4
53	Left femoral artery	44.3	0.314	0.275	−60.1	−104.4
54	Left posterior tibial artery	34.4	0.175	0.175	−104.4	−138.8
55	Left anterior tibial artery	32.2	0.25	0.25	−104.4	−136.6
56	Basilar artery	2.9	0.162	0.162	21	22
57	Right posterior cerebral artery I	0.5	0.107	0.107	22	22
58	Right posterior cerebral artery II	8.6	0.105	0.105	22	22
59	Right posterior communicating artery	1.5	0.073	0.073	22	22
60	Right internal carotid artery II	0.5	0.2	0.2	22	22
61	Right middle cerebral artery	11.9	0.143	0.143	22	22
62	Right anterior cerebral artery I	1.2	0.117	0.117	22	22
63	Right anterior cerebral artery II	10.3	0.12	0.12	22	22
64	Anterior communicating artery	0.3	0.1	0.1	22	22
65	Left anterior cerebral artery II	10.3	0.12	0.12	22	22
66	Left anterior cerebral artery I	1.2	0.117	0.117	22	22
67	Left middle cerebral artery	11.9	0.143	0.143	22	22
68	Left internal carotid artery II	0.5	0.2	0.2	22	22
69	Left posterior communicating artery	1.5	0.073	0.073	22	22
70	Left posterior cerebral artery II	8.6	0.105	0.105	22	22
71	Left posterior cerebral artery I	0.5	0.107	0.107	22	22
72	Left external carotid artery II	6.1	0.2	0.2	21.99	28.09
73	Right external carotid artery II	6.1	0.2	0.2	21.99	28.09
74	Left superior thyroid artery	10.1	0.1	0.1	21.99	21.99
75	Right superior thyroid artery	10.1	0.1	0.1	21.99	21.99
76	Left superficial temporal artery	6.1	0.16	0.16	28.09	28.09
77	Right superficial temporal artery	6.1	0.16	0.16	28.09	28.09
78	Left maxillary artery	9.1	0.11	0.11	28.09	28.09
79	Right maxillary artery	9.1	0.11	0.11	28.09	28.09
80	Left superficial temporal frontal branch	10	0.11	0.11	28.09	28.09
81	Right superficial temporal frontal branch	10	0.11	0.11	28.09	28.09

TABLE A1 (Continued)

No.	Vessel name	L (cm)	r_0 (cm)	r_1 (cm)	η_0 (cm)	η_1 (cm)
82	Left superficial temporal parietal branch	10.1	0.11	0.11	28.09	28.09
83	Right superficial temporal parietal branch	10.1	0.11	0.11	28.09	28.09
84	Superior vena cava I	1.5	0.8	0.8	1.5	0
85	Superior vena cava II	2	0.8	0.8	3.5	1.5
86	Right brachiocephalic vein	4	0.564	0.564	7.5	3.5
87	Left brachiocephalic vein	7.5	0.535	0.535	7.5	3.5
88	Left subclavian vein I	3	0.564	0.564	7.5	7.5
89	Right subclavian vein I	3	0.564	0.564	7.5	7.5
90	Right external jugular vein	10	0.252	0.252	17.5	12.5
91	Left external jugular vein	10	0.252	0.357	17.5	12.5
92	Right internal jugular vein I	2.5	0.399	0.399	9.5	8.5
93	Left internal jugular vein I	2.5	0.564	0.618	9.5	8.5
94	Left vertebral vein II	11	0.138	0.16	22	12.5
95	Right vertebral vein II	11	0.138	0.16	22	12.5
96	Right deep cervical vein	13	0.16	0.16	22	12.5
97	Left deep cervical vein	13	0.16	0.16	22	12.5
98	Vertebral venous plexus	71	0.368	0.368	22	−46.4
99	Right sigmoid sinus II	3.5	0.252	0.252	22	22
100	Left sigmoid sinus II	3.5	0.357	0.378	22	22
101	Right transverse sinus I	3.5	0.218	0.178	22	22
102	Left transverse sinus I	3.5	0.437	0.309	22	22
103	Sup. sagittal sinus	2.5	0.35	0.367	22	22
104	Straight sinus	4	0.25	0.25	22	22
105	Inf. sagittal sinus	3.67	0.16	0.16	22	22
106	Vein of Galen	0.6	0.366	0.4	22	22
107	Left internal cerebral vein	5	0.126	0.126	22	22
108	Right internal cerebral vein	5	0.126	0.126	22	22
109	Left basal vein of Rosenthal I	1	0.126	0.126	22	22
110	Right basal vein of Rosenthal I	1	0.126	0.126	22	22
111	Right superior petrosal sinus	5.7	0.149	0.149	22	22
112	Left superior petrosal sinus	5.7	0.149	0.149	22	22
113	Right inferior petrosal sinus	3.2	0.08	0.16	22	22
114	Left inferior petrosal sinus	3.2	0.08	0.16	22	22
115	Right posterior auricular vein	5	0.08	0.08	22.5	17.5
116	Left posterior auricular vein	5	0.08	0.08	22.5	17.5
117	Right posterior retromandibular vein	3.52	0.25	0.25	19.25	17.5
118	Left posterior retromandibular vein	3.52	0.25	0.25	19.25	17.5
119	Right anterior retromandibular vein	3.15	0.235	0.235	19.25	16.1
120	Left anterior retromandibular vein	3.15	0.235	0.235	19.25	16.1
121	Right retromandibular vein	4.5	0.26	0.26	22	19.25
122	Left retromandibular vein	4.5	0.26	0.26	22	19.25
123	Right facial vein II	6	0.132	0.178	22	16.1
124	Left facial vein II	6	0.132	0.178	22	16.1

(Continues)

TABLE A1 (Continued)

No.	Vessel name	L (cm)	r_0 (cm)	r_1 (cm)	η_0 (cm)	η_1 (cm)
125	Right common facial vein	0.9	0.18	0.18	16.1	15.2
126	Left common facial vein	0.9	0.18	0.18	16.1	15.2
127	Right superficial temporal vein	5	0.19	0.19	27	22
128	Left superficial temporal vein	5	0.19	0.19	27	22
129	Right maxillary vein	1	0.175	0.175	22	22
130	Left maxillary vein	1	0.175	0.175	22	22
131	Right deep facial vein	0.9	0.25	0.25	22	22
132	Left deep facial vein	0.9	0.25	0.25	22	22
133	Right emissary vein	3	0.1	0.1	22	22
134	Left emissary vein	3	0.1	0.1	22	22
135	Right pterygoid plexus	0.9	0.15	0.15	22	22
136	Left pterygoid plexus	0.9	0.15	0.15	22	22
137	Right marginal sinus	4	0.1	0.1	22	22
138	Left marginal sinus	4	0.1	0.1	22	22
139	Occipital sinus	3.5	0.235	0.235	22	22
140	Right external jugular vein	10	0.252	0.252	12.5	7.5
141	Right mastoid emissary vein	7.2	0.175	0.175	22	22
142	Left mastoid emissary vein	7.2	0.175	0.175	22	22
143	Right posterior condylar vein	3	0.315	0.315	22	22
144	Left posterior condylar vein	3	0.315	0.315	22	22
145	Right suboccipital sinus	1	0.45	0.45	22	22
146	Right lateral anterior condylar vein	3	0.315	0.315	22	22
147	Left lateral anterior condylar vein	3	0.315	0.315	22	22
148	Left external jugular vein	10	0.252	0.357	12.5	7.5
149	Superior sagittal sinus	4.33	0.229	0.258	22	22
150	R. Labbe v.	5	0.15	0.15	22	22
151	L. Labbe v.	5	0.15	0.15	22	22
152	Superior sagittal sinus	4.33	0.258	0.287	22	22
153	Superior sagittal sinus	2.5	0.334	0.35	22	22
154	Left cavernous sinus	1.5	0.1	0.1	22	22
155	Right cavernous sinus	1.5	0.1	0.1	22	22
156	Occipital vein	5	0.126	0.126	22	22
157	Superior sagittal sinus	5	0.3	0.334	22	22
158	Cerebral vein	5	0.15	0.15	22	22
159	Cerebral vein	5	0.15	0.15	22	22
160	Azygos vein I	2	0.425	0.425	−0.5	1.5
161	Cerebral vein	5	0.15	0.15	22	22
162	Cerebral vein	5	0.15	0.15	22	22
163	Right vertebral vein I	5	0.16	0.16	12.5	7.5
164	Left vertebral vein I	5	0.16	0.16	12.5	7.5
165	Superior sagittal sinus III	4.33	0.2	0.229	22	22
166	Left suboccipital sinus	1	0.45	0.45	22	22
167	Right anastomotic vein	2	0.1	0.1	22	22

TABLE A1 (Continued)

No.	Vessel name	L (cm)	r_0 (cm)	r_1 (cm)	η_0 (cm)	η_1 (cm)
168	Left anastomotic vein	2	0.1	0.1	22	22
169	Right facial artery	11.6	0.13	0.13	21.99	21.99
170	Left facial artery	11.6	0.13	0.13	21.99	21.99
171	Right great saphenous vein I	7.5	0.222	0.23	−66.5	−59
172	Left great saphenous vein I	7.5	0.222	0.23	−66.5	−59
173	Left posterior tibial vein I	17.3	0.15	0.15	−120.7	−103.4
174	Left anterior tibial vein I	16	0.15	0.15	−119.4	−103.4
175	Right popliteal vein	19	0.34	0.34	−103.4	−84.4
176	Left popliteal vein	19	0.34	0.34	−103.4	−84.4
177	Left femoral vein	25.4	0.35	0.35	−84.4	−59
178	Right femoral vein	25.4	0.35	0.35	−84.4	−59
179	Right deep femoral vein	12.6	0.35	0.35	−71.6	−59
180	Left deep femoral vein	12.6	0.35	0.35	−71.6	−59
181	Right external iliac vein	14.4	0.5	0.5	−59	−44.6
182	Left external iliac vein	14.4	0.5	0.5	−59	−44.6
183	Left internal iliac vein	5	0.15	0.15	−49.6	−44.6
184	Right internal iliac vein	5	0.15	0.15	−49.6	−44.6
185	Right common iliac vein II	2	0.575	0.575	−44.6	−42.6
186	Left common iliac vein II	2	0.575	0.575	−44.6	−42.6
187	Right radial vein	40.6	0.2	0.2	−60.1	−19.5
188	Left interosseous vein	7	0.1	0.1	−36.5	−29.5
189	Right ulnar vein II	30.6	0.2	0.2	−60.1	−29.5
190	Left ulnar vein II	30.6	0.2	0.2	−60.1	−29.5
191	Left interosseous vein	7	0.1	0.1	−36.5	−29.5
192	Left radial vein	40.6	0.2	0.2	−60.1	−19.5
193	Left subclavian vein III	27	0.52	0.52	−19.5	4.5
194	Right subclavian vein III	27	0.52	0.52	−19.5	4.5
195	Left subclavian vein II	3	0.52	0.52	4.5	7.5
196	Right subclavian vein II	3	0.52	0.52	4.5	7.5
197	Left ulnar vein I	10	0.2	0.2	−29.5	−19.5
198	Inferior vena cava I	15.3	0.762	0.762	−15.3	0
199	Hepatic vein	6.8	0.485	0.485	−15.3	−15.3
200	Inferior vena cava II	1.5	0.762	0.762	−16.8	−15.3
201	Inferior vena cava III	1.5	0.762	0.762	−18.3	−16.8
202	Inferior vena cava IV	12.5	0.762	0.762	−30.8	−18.3
203	Inferior vena cava V	8	0.762	0.762	−38.8	−30.8
204	Right common iliac vein I	3.8	0.575	0.575	−42.6	−38.8
205	Left common iliac vein I	3.8	0.575	0.575	−42.6	−38.8
206	Right ulnar vein I	10	0.2	0.2	−29.5	−19.5
207	Left renal vein	3.2	0.25	0.25	−16.8	−16.8
208	Right renal vein	3.2	0.25	0.25	−18.3	−18.3
209	Ascending lumbar vein	23	0.2	0.2	−42.6	−28.5
210	Hemiazygos vein	23	0.28	0.28	−42.6	−28.5

(Continues)

TABLE A1 (Continued)

No.	Vessel name	L (cm)	r_0 (cm)	r_1 (cm)	η_0 (cm)	η_1 (cm)
211	Inferior mesenteric vein	6	0.45	0.45	−30.8	−30.8
212	Right posterior tibial vein I	17.3	0.15	0.15	−120.7	−103.4
213	Right anterior tibial vein I	16	0.15	0.15	−119.4	−103.4
214	Right anterior tibial vein II	2	0.6	0.6	−136	−134
215	Left anterior tibial vein II	2	0.6	0.6	−136	−134
216	Right lumbar vein	3.8	0.1	0.1	−46.4	−42.6
217	Left lumbar vein	3.8	0.1	0.1	−46.4	−42.6
218	Right superior thyroid vein	4	0.15	0.15	12.5	10.5
219	Left superior thyroid vein	4	0.15	0.15	12.5	10.5
220	Right middle thyroid vein	3	0.1	0.1	10.5	9.5
221	Left middle thyroid vein	3	0.1	0.1	10.5	9.5
222	Inferior thyroid vein	7	0.126	0.126	10.5	3.5
223	Thyroid connection	2	0.16	0.16	12.5	10.5
224	Right internal jugular vein II	3	0.357	0.357	12.5	9.5
225	Left internal jugular vein II	3	0.564	0.564	12.5	9.5
226	Right internal jugular vein III	2.7	0.252	0.357	15.2	12.5
227	Left internal jugular vein III	2.7	0.564	0.564	15.2	12.5
228	Right internal jugular vein IV	6.8	0.252	0.252	22	15.2
229	Left internal jugular vein IV	6.8	0.399	0.564	22	15.2
230	Right sigmoid sinus I	1.5	0.252	0.252	22	22
231	Left sigmoid sinus I	1.5	0.378	0.399	22	22
232	Right transverse sinus II	3.5	0.178	0.252	22	22
233	Left transverse sinus II	3.5	0.309	0.357	22	22
234	Right facial vein I	2	0.113	0.132	22	22
235	Left facial vein I	2	0.113	0.132	22	22
236	Superior sagittal sinus II	2	0.287	0.3	22	22
237	Cerebral vein	5	0.15	0.15	22	22
238	Cerebral vein	5	0.15	0.15	22	22
239	Cerebral vein	5	0.15	0.15	22	22
240	Intracavernous sinus	2	0.126	0.126	22	22
241	Inferior sagittal sinus	3.67	0.16	0.16	22	22
242	Right internal jugular vein V	1	0.399	0.399	8.5	7.5
243	Left internal jugular vein V	1	0.618	0.618	8.5	7.5
244	Azygos vein II	28	0.425	0.425	−28.5	−0.5
245	Cerebral vein	3	0.15	0.15	22	22
246	Left basal vein of Rosenthal II	7	0.126	0.126	22	22
247	Right basal vein of Rosenthal II	7	0.126	0.126	22	22
248	Inferior sagittal sinus	3.67	0.16	0.16	22	22
249	Cerebral vein	3	0.15	0.15	22	22
250	Intercostal vein	2	0.4	0.4	−28.5	−28.5
251	Right posterior tibial vein II	17.3	0.15	0.15	−138	−120.7
252	Right anterior tibial vein II	16	0.15	0.15	−134	−119.4
253	Right great saphenous vein II	37.5	0.145	0.188	−134	−96.5

TABLE A1 (Continued)

No.	Vessel name	L (cm)	r_0 (cm)	r_1 (cm)	η_0 (cm)	η_1 (cm)
254	Left great saphenous vein II	37.5	0.145	0.188	−134	−96.5
255	Left anterior tibial vein II	16	0.15	0.15	−134	−119.4
256	Left posterior tibial vein I	17.3	0.15	0.15	−138	−120.7
257	Right great saphenous vein III	30	0.188	0.222	−96.5	−66.5
258	Left great saphenous vein III	30	0.188	0.222	−96.5	−66.5
259	Confluence of sinuses	1	0.01	0.01	22	22
260	Cerebral vein	3	0.15	0.15	22	22
261	Terminal cerebral vein	1	0.15	0.15	22	22
262	Terminal cerebral vein	1	0.15	0.15	22	22
263	Terminal cerebral vein	1	0.15	0.15	22	22
264	Terminal cerebral vein	1	0.15	0.15	22	22
265	Terminal cerebral vein	1	0.15	0.15	22	22
266	Terminal cerebral vein	1	0.15	0.15	22	22
267	Terminal cerebral vein	1	0.15	0.15	22	22
268	Terminal cerebral vein	1	0.15	0.15	22	22
269	Terminal cerebral vein	1	0.15	0.15	22	22
270	Terminal cerebral vein	1	0.15	0.15	22	22
271	Terminal cerebral vein	1	0.309	0.366	22	22
272	Terminal cerebral vein	1	0.15	0.15	22	22
273	Terminal cerebral vein	1	0.15	0.15	22	22
274	Main pulmonary artery	4.3	1.35	1.35	0	1.075
275	Left pulmonary artery	2.5	0.9	0.9	1.075	2.325
276	Right pulmonary artery	5.8	1.1	1.1	1.075	2.325
277	Left inferior pulmonary artery	2.1	0.843	0.843	2.325	1.065
278	Left superior pulmonary artery	1.2	0.481	0.481	2.325	3.525
279	Right inferior pulmonary artery	2.4	0.923	0.923	2.325	1.125
280	Right superior pulmonary artery	1.9	0.755	0.755	2.325	3.275
281	LIA1 0 2	1.9	0.757	0.757	1.065	−0.075
282	LIA0 1 3	1.3	0.514	0.514	1.065	1.065
283	LIA2 0 4	1.7	0.681	0.681	−0.075	−1.095
284	LIA1 1 5	1.2	0.461	0.461	−0.075	−0.075
285	LIA3 0 6	1.6	0.612	0.612	−1.095	−2.055
286	LIA2 1 7	1.1	0.415	0.415	−1.095	−1.095
287	LIA4 0 8	1.4	0.55	0.55	−2.055	−2.895
288	LIA3 1 9	1	0.373	0.373	−2.055	−2.055
289	LIA5 0 10	1.3	0.494	0.494	−2.895	−2.895
290	LIA4 1 11	0.9	0.335	0.335	−2.895	−2.895
291	LIA1 1 12	1.2	0.461	0.461	1.065	1.065
292	LIA0 2 13	0.8	0.313	0.313	1.065	1.065
293	LSA1 0 15	1.1	0.433	0.433	3.525	4.625
294	LSA0 1 16	0.7	0.294	0.294	3.525	3.525
295	LSA2 0 17	1	0.389	0.389	4.625	5.625
296	LSA1 1 18	0.7	0.264	0.264	4.625	4.625

(Continues)

TABLE A1 (Continued)

No.	Vessel name	L (cm)	r_0 (cm)	r_1 (cm)	η_0 (cm)	η_1 (cm)
297	LSA3 0 19	0.9	0.35	0.35	5.625	6.525
298	LSA2 1 20	0.6	0.237	0.237	5.625	5.625
299	LSA4 0 21	0.8	0.314	0.314	6.525	6.525
300	LSA3 1 22	0.5	0.213	0.213	6.525	6.525
301	RIA1 0 24	2.1	0.829	0.829	1.125	0.075
302	RIA0 1 25	1.4	0.562	0.562	1.125	1.125
303	RIA2 0 26	1.9	0.745	0.745	0.075	−0.875
304	RIA1 1 27	1.3	0.506	0.506	0.075	0.075
305	RIA3 0 28	1.7	0.67	0.67	−0.875	−1.725
306	RIA2 1 29	1.2	0.454	0.454	−0.875	−0.875
307	RIA4 0 30	1.5	0.602	0.602	−1.725	−2.475
308	RIA3 1 31	1	0.408	0.408	−1.725	−1.725
309	RIA5 0 32	1.4	0.541	0.541	−2.475	−3.175
310	RIA4 1 33	0.9	0.367	0.367	−2.475	−2.475
311	RIA6 0 34	1.2	0.486	0.486	−3.175	−3.175
312	RIA5 1 35	0.8	0.33	0.33	−3.175	−3.175
313	RIA2 1 36	1.2	0.454	0.454	0.075	0.075
314	RIA1 2 37	0.8	0.308	0.308	0.075	0.075
315	RIA1 1 38	1.3	0.506	0.506	1.125	1.125
316	RIA0 2 39	0.9	0.343	0.343	1.125	1.125
317	RIA2 1 40	1.2	0.454	0.454	1.125	1.125
318	RIA1 2 41	0.8	0.308	0.308	1.125	1.125
319	RSA1 0 43	1.7	0.678	0.678	3.275	4.125
320	RSA0 1 44	1.2	0.46	0.46	3.275	3.275
321	RSA2 0 45	1.6	0.61	0.61	4.125	4.925
322	RSA1 1 46	1.1	0.413	0.413	4.125	4.125
323	RSA3 0 47	1.4	0.548	0.548	4.925	5.625
324	RSA2 1 48	0.9	0.372	0.372	4.925	4.925
325	RSA4 0 49	1.3	0.492	0.492	5.625	6.275
326	RSA3 1 50	0.9	0.334	0.334	5.625	5.625
327	RSA5 0 51	1.1	0.443	0.443	6.275	6.275
328	RSA4 1 52	0.8	0.3	0.3	6.275	6.275
329	RSA1 1 53	1.1	0.413	0.413	3.275	3.275
330	RSA0 2 54	0.7	0.28	0.28	4.925	4.925
331	Left inferior pulmonary vein	2.1	0.641	0.641	−0.735	0
332	Left superior pulmonary vein	1.2	0.715	0.715	1.864	0
333	Right inferior pulmonary vein	2.4	0.864	0.864	−0.672	0
334	Right superior pulmonary vein	1.9	0.823	0.823	1.349	0
335	LIV1 0 2	1.9	0.576	0.576	−1.4	−0.735
336	LIV0 1 3	1.3	0.391	0.391	−1.19	−0.735
337	LIV2 0 4	1.7	0.518	0.518	−1.995	−1.4
338	LIV1 1 5	1.2	0.351	0.351	−1.4	−1.4
339	LIV3 0 6	1.6	0.466	0.466	−2.555	−1.995

TABLE A1 (Continued)

No.	Vessel name	L (cm)	r_0 (cm)	r_1 (cm)	η_0 (cm)	η_1 (cm)
340	LIV2 1 7	1.1	0.316	0.316	−1.995	−1.995
341	LIV4 0 8	1.4	0.418	0.418	−3.045	−2.555
342	LIV3 1 9	1	0.284	0.284	−2.555	−2.555
343	LIV5 0 10	1.3	0.376	0.376	−3.045	−3.045
344	LIV4 1 11	0.9	0.255	0.255	−3.045	−3.045
345	LIV1 1 12	1.2	0.351	0.351	−1.19	−1.19
346	LIV0 2 13	0.8	0.238	0.238	−1.19	−1.19
347	LSV1 0 15	1.1	0.643	0.643	3.572	1.864
348	LSV0 1 16	0.7	0.436	0.436	1.864	1.864
349	LSV2 0 17	1	0.578	0.578	5.125	3.572
350	LSV1 1 18	0.7	0.392	0.392	3.572	3.572
351	LSV3 0 19	0.9	0.52	0.52	6.523	5.125
352	LSV2 1 20	0.6	0.352	0.352	5.125	5.125
353	LSV4 0 21	0.8	0.467	0.467	6.523	6.523
354	LSV3 1 22	0.5	0.317	0.317	6.523	6.523
355	RIV1 0 24	2.1	0.777	0.777	−1.26	−0.672
356	RIV0 1 25	1.4	0.527	0.527	−1.064	−0.672
357	RIV2 0 26	1.9	0.698	0.698	−1.792	−1.26
358	RIV1 1 27	1.3	0.473	0.473	−1.624	−1.26
359	RIV3 0 28	1.7	0.627	0.627	−2.268	−1.792
360	RIV2 1 29	1.2	0.426	0.426	−1.792	−1.792
361	RIV4 0 30	1.5	0.564	0.564	−2.688	−2.268
362	RIV3 1 31	1	0.382	0.382	−2.268	−2.268
363	RIV5 0 32	1.4	0.507	0.507	−3.08	−2.688
364	RIV4 1 33	0.9	0.344	0.344	−2.688	−2.688
365	RIV6 0 34	1.2	0.456	0.456	−3.08	−3.08
366	RIV5 1 35	0.8	0.309	0.309	−3.08	−3.08
367	RIV2 1 36	1.2	0.426	0.426	−1.624	−1.624
368	RIV1 2 37	0.8	0.289	0.289	−1.624	−1.624
369	RIV1 1 38	1.3	0.473	0.473	−1.428	−1.064
370	RIV0 2 39	0.9	0.321	0.321	−1.064	−1.064
371	RIV2 1 40	1.2	0.426	0.426	−1.428	−1.428
372	RIV1 2 41	0.8	0.289	0.289	−1.428	−1.428
373	RSV1 0 43	1.7	0.74	0.74	2.556	1.349
374	RSV0 1 44	1.2	0.502	0.502	1.349	1.349
375	RSV2 0 45	1.6	0.665	0.665	3.692	2.556
376	RSV1 1 46	1.1	0.451	0.451	2.556	2.556
377	RSV3 0 47	1.4	0.598	0.598	4.686	3.692
378	RSV2 1 48	0.9	0.406	0.406	3.692	3.692
379	RSV4 0 49	1.3	0.537	0.537	5.609	4.686
380	RSV3 1 50	0.9	0.364	0.364	4.686	4.686
381	RSV5 0 51	1.1	0.483	0.483	6.39	5.609
382	RSV4 1 52	0.8	0.328	0.328	5.609	5.609

(Continues)

TABLE A1 (Continued)

No.	Vessel name	L (cm)	r_0 (cm)	r_1 (cm)	η_0 (cm)	η_1 (cm)
383	RSV1 1 53	1.1	0.451	0.451	1.349	1.349
384	RSV0 2 54	0.7	0.306	0.306	1.349	1.349